Structure and Dynamics of Lithium in Anatase TiO$_2$

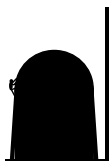Study of interstitial Li-ion intercalation in anatase TiO$_2$ at the atomic level

Structure and Dynamics of Lithium in Anatase TiO$_2$

Study of interstitial Li-ion intercalation in anatase TiO$_2$
at the atomic level

PROEFSCHRIFT

ter verkrijging van de graad van doctor
aan de Technische Universiteit Delft,
op gezag van de Rector Magnificus prof. dr. ir. J.T. Fokkema,
voorzitter van het College voor Promoties
in het openbaar te verdedigen op maandag 17 februari 2003 om 16.00 uur

door

Marnix WAGEMAKER

natuurkundig ingenieur
geboren te Leiden

Dit proefschrift is goedgekeurd door de promotor:
Prof. dr. G.J. Kearley

Toegevoegd promotor:
Dr. ir. A.A. van Well

Samenstelling promotiecommissie:
Rector Magnificus   voorzitter
Prof. dr. G.J. Kearley   Technische Universiteit Delft, promotor
Dr. ir. A.A. van Well   Technische Universiteit Delft, toegevoegd promotor
Prof. dr. R. Frahm   Universiteit Wüppertal
Prof. dr. A.P.M. Kentgens   Katholieke Universiteit Nijmegen
Prof. dr. J. Schoonman   Technische Universiteit Delft
Prof. dr. I.M. de Schepper   Technische Universiteit Delft
Dr. F.M. Mulder   Technische Universiteit Delft

Printed in The Netherlands

Contents

Chapter 1

Introduction

Titanium dioxide TiO_2 occurs naturally in three crystalline forms: rutile, anatase and brookite. In rutile, the most common form, titanium is octahedrally coordinated by oxygen, whereas in anatase and brookite the oxygen octahedron is distorted. Because it is more common, it is often assumed that rutile is the most stable form, however, anatase is the thermodynamically stable form.

The first practical use of TiO_2 was as white pigment in paint replacing the toxic lead oxides. The whiteness is due to the relatively high refractive index which in combination with small particle sizes results in strong light scattering in a broad range of wavelengths. Rutile has a slightly higher refractive index compared to anatase and is extensively used as pigment. The optical properties and chemical stability have extended its use to countless commercial products like toothpaste and sun lotion.

The more recent interest in the anatase TiO_2 variant is based on a number of more sophisticated and technically applicable properties. The high (photo)catalytic activity can be used in waste-water purification reactors. Another recent application is the use as electron collector in Grätzel type solar cells [1] which is mainly due to the high electron mobility in anatase TiO_2. Furthermore the open crystallographic structure of anatase facilitates the accommodation of substantial amounts of Li-ions (or other small ions) within the lattice. Consequently it is applied as electrode material in Li-ion battery systems [2]. Lithium insertion changes the optical properties of TiO_2: it turns the white powder dark blue whilst in thin film form it changes from being transparent to partially reflecting. This is generally referred to as electrochromism and finds application in displays and sun-blinds (switchable mirrors) [3]. In this thesis we focus on the fundamental properties of lithium inserted TiO_2 that might be related to the use in electrochromic applications and in particular in battery devices.

In the last decades there has been growing attention to environmentally friendly methods for the production and storage of energy. Therefore, alternatives are sought to replace the existing rechargeable systems like the lead battery and nickel cadmium batteries which contain heavy metals and have a relative low energy density expressed in mAh/g. The Li-ion batteries came into the picture as a result of its high energy capacity, re-chargeability and its environmental friendly properties.

Anatase TiO_2 may act as an anode in such a battery, a schematic of the battery is shown in figure 1.1. In practice, anatase TiO_2 is not the ideal candidate because of its relatively low potential versus other electrode materials. Here it is considered as a
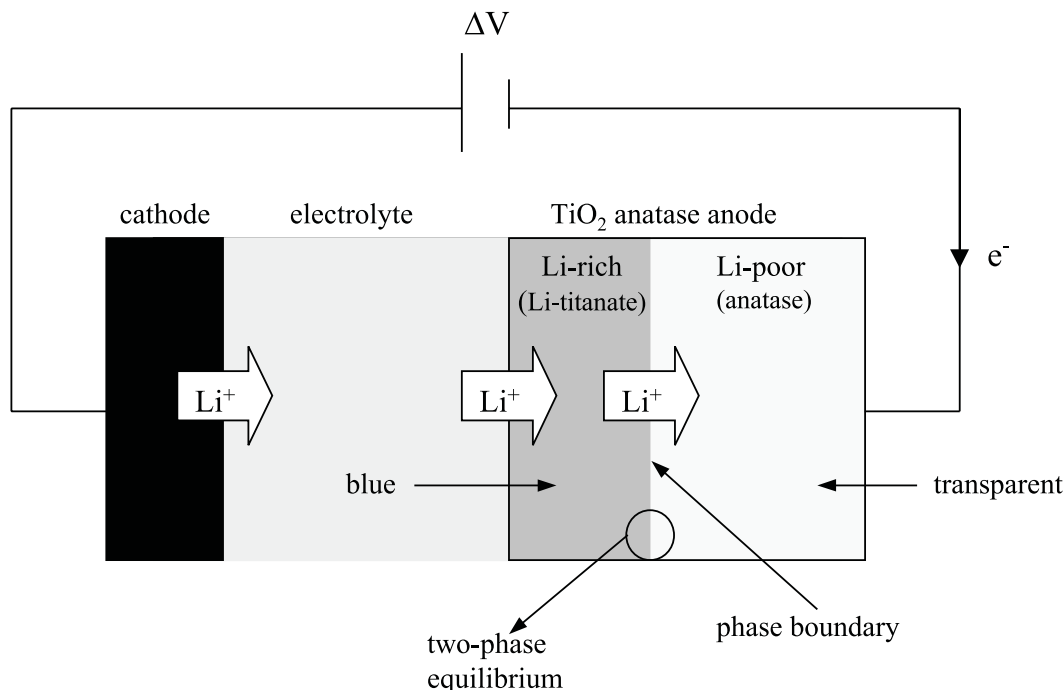
Figure 1.1: *Schematic view of a lithium ion-battery with thin film anatase TiO$_2$ as anode. In this setup the battery is loaded, thus Li-ion are inserted in the anatase TiO$_2$ lattice.*

well defined model material displaying many typical properties of transition metal oxide electrodes. The electrode and electrochromic properties of lithiated anatase TiO$_2$ are already well documented and partly exploited commercially. However, the fundamental understanding of the microscopic processes that result in these properties is still missing. The reason for this is that these processes take place on such short time (ps-ms) and length scales (0.1-100 nm) that they are generally difficult to probe. The aim of this thesis study is to quantify and understand the processes at those small scales. Real understanding can be expected to result in much more efficient exploitation of the properties of materials. Thus we embark on a study that probes the lithiated anatase TiO$_2$ system on an atomic scale.

1.1   Background lithium intercalation in anatase TiO$_2$

Lithiated anatase TiO$_2$ has already been the subject of many experimental and theoretical studies. Here we focus on the most important results that are microscopic in nature and relevant in the context of this thesis.

Anatase TiO$_2$ has a tetragonal structure indexed by the I41/amd space group (number 141) in which titanium is surrounded by a distorted oxygen octahedron. Upon lithiation the anatase lattice undergoes an orthorhombic distortion that results in the Li$_{0.5}$TiO$_2$ phase indexed by the space group Imma (number 74) [4]. The unit cell of both

TiO$_2$ anatase   LiTiO$_2$ Li-titanate
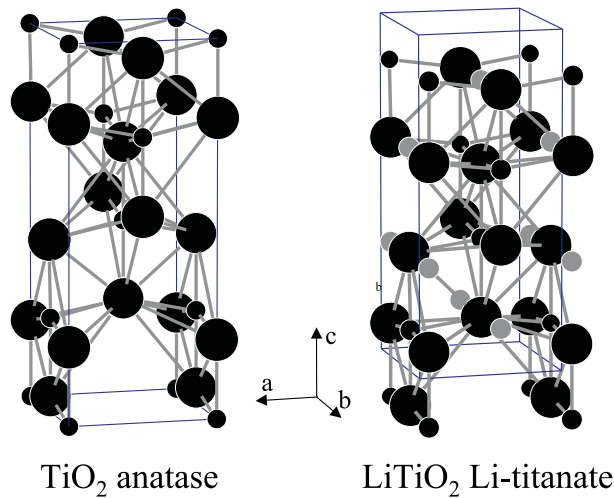
Figure 1.2: *The unit cell of anatase TiO$_2$ (space group I4$_1$/amd) and the same cell of LiTiO$_2$ lithium titanate (space group Imma, the unit cell is different from that of anatase and is indicated by the rectangular box). Ti: small black spheres, O: large black spheres, Li: gray spheres.*

structures is illustrated in figure 1.2. In this thesis the Li$_{0.5}$TiO$_2$ phase is referred to as Li-titanate. The overall distortion of the atomic positions in the change from TiO$_2$ (anatase) to Li-titanate is small and leads to more regular TiO$_6$ octahedra in Li-titanate. The change in symmetry is accompanied by a decrease of the unit cell along the *c*-axis and an increase along the *b*-axis, resulting in an increase of ∼4 % of the unit cell volume. Lithium was found to reside in the interstitial voids within the oxygen octahedra [4]. The structural change can be explained as occupation of Ti-Ti bonding atomic orbitals by the electron that enters the TiO$_2$ lattice with each Li-ion to maintain charge neutrality (see below).

Based on electrochemistry, the (macroscopic) diffusion coefficient at room temperature for chemical vapor deposited (CVD) films was determined in the order of 2 × 10^{-15} cm^{2}s^{-1} for insertion and 6 × 10^{-15}cm^{2}s^{-1} for extraction with activation energies between 0.5 and 0.7 eV [5]. For single crystal anatase significantly larger values have been obtained; 2 × 10^{-13} cm^{2}s^{-1} for insertion and 6 × 10^{-13}cm^{2}s^{-1} for extraction with activation energies of 0.54 eV and 0.78 eV respectively [6]. Van de Krol *et al.* [7] suggested that the difference found between the rate of insertion and the rate of extraction is due to a difference in the mobility of lithium in anatase TiO$_2$ and in Li-titanate.

The microscopic diffusion mechanism has only been studied theoretically based on calculations. Lunell *et al.* [8] predicted that the lithium ion diffusion in the lithiated anatase framework is likely to occur along a diffusion path connecting the vacant octahedral interstitial sites. From each octahedral site four possible directions lead to the next site. The activation energy for such an inter-octahedron jump was calculated to be ≈0.50-0.6 eV. Another study based on calculations predicted that the diffusion in Li-titanate is anisotropic: slow diffusion in the *ab*-planes and faster diffusion in the *c*-direction [9]. The calculations predicted a thermodynamically stable two phase system.

TiO$_2$ is a semi-conductor with a large band gap of 3.26 eV which gives rise to pho-

ton absorption only below wavelengths of 380 nm. As a result it is white in powder form and transparent as thin film and single crystal. Titanium donates much of its four outer electrons (Ti-$3d^2$ and Ti-$4s^2$) to oxygen giving rise to an ionic type of bonding with partial covalent character of the Ti-O bonds [10]. Conservation of overall charge neutrality under insertion of the positively charged Li$^+$ ion forces the uptake of an electron. The electron is believed to be responsible for the electrochromic effect, the dark blue coloration of the otherwise white or transparent TiO_2. However, the orbitals in which the electrons reside and the degree of localization of the electrons is unclear. The electrochromic effect has been proposed to result from photon absorption by (almost) free electrons [11, 12, 13] although an *in-situ* conductivity and optical absorption study suggested a localized electron character [14]. It has also been suggested that the coloration was due to polaron absorption by electrons localized at Ti^{3+} ions [15, 16] and by electrons trapped at surface states [17].

Theoretical studies and calculations indicate that the charge compensating electrons occupy the bottom of the conduction band which is predominantly *3d* in character [18, 19] in agreement with the general picture for Li insertion in transition metal oxides [20]. Based on calculations, Nuspl *et al.* [21] argued that the structural change of anatase TiO_2 upon lithiation into $Li_{0.5}TiO_2$ can be explained by filling of Ti-Ti bonding bands at the bottom of the conduction band. The formation of localized Ti-Ti bonds also suggests the non-metallic resistivity of Li-doped anatase which would not be expected if the electrons are delocalized over the whole Ti-O framework [22].

A model that entails a localized nature of the electrons and also predicts the correct photon absorption energies is presented by Stashans *et al.* [19]. In their calculations a local lithium ion induced one-electron level is predicted well below the conduction band, similar to doping levels in doped semi-conductors (Li_xTiO_2 can be considered to be a doped semi-conductor but with an extremely high doping concentration).

1.2 Outline of this thesis: Scientific questions and the techniques to solve them

The main objective of this thesis is to formulate different aspects of Li-insertion in a microscopic picture which may be related to the physical properties and macroscopic material behavior. In particular, in the order of descending length scales, the spontaneous phase separation and the structure and dynamics in each of the two phases down to the very local level was studied. To do this, microscopic methods are required that probe the local lithium environment and the lithium mobility. These methods were chosen for their sensitivity as local probe on different length and time-scales.

The result is a multi-technique approach. The techniques applied are neutron scattering, more specific neutron diffraction (ND), quasi-elastic neutron scattering (QENS) and neutron reflectometry (NR). Further scattering techniques used are X-ray diffraction (XRD) and X-ray absorption spectroscopy (XAS). Last but not least nuclear magnetic resonance (NMR) is also applied. This study illustrates the applicability and complementary nature of these techniques for microscopic studies of lithium intercalation compounds.

The experimental chapters that form the heart of this thesis are mainly based on

papers either published [23, 24, 25, 26, 27], submitted [28, 29] or prepared for submission [30]. As a result, there is overlap in part of the introduction of each chapter. Another consequence is that in these chapters little attention is devoted to the experimental technique. For this reason chapter 2 is added, in which a short introduction to the techniques is presented.

1.2.1   Atomic structure and morphology

In principle the atomic structure of both anatase TiO_2 and Li-titanate are known, and beforehand there seemed to be no reason to conduct further study. The Li-position in Li-titanate has already been determined, and one might expect it to be the same in the similar anatase structure. But even the Li position in Li-titanate previously determined with neutron diffraction will be shown to be more complicated than was thought. Furthermore, little is known concerning the two-phase morphology in battery operation and its influence on overall diffusion. Often it is not even treated as a two-phase system. This is rather surprising as the coexistence of two or more phases in batteries generally leads to the favorable property of a constant potential during operation.

The obvious method for structure determination is diffraction, using either X-rays or neutrons since the wavelength of X-rays and thermal neutrons are in the order of the atomic distances. The atomic sensitivity of X-rays increases with the atomic number whereas for neutrons it varies more or less randomly through the periodic table. In particular neutrons are relatively sensitive for H and Li, being the reason why neutrons are preferred despite of the fact that the neutron beam intensity is orders of magnitude lower than the X-ray beam intensity. If the periodic structures, crystal grains, that build up the coherent reflections (diffraction lines) are relatively small, roughly smaller that 200 nm, the reflections are less well defined leading to (particle size) line broadening. Although it is hard to separate this effect from strain broadening, the effects appear in many cases connected, and one can extract approximate domain sizes in multi-phase structures. The structure of lithiated anatase, and in particular the high resolution Li-ion position(s) as determined with neutron diffraction, are the topic of chapter 5 whereas X-ray diffraction is part of chapter 3. One might expect the neutron diffraction study as the first of the experimental chapters, but this study was actually performed at a later stage because the questions that initiated it arose during the NMR studies covered by the first two experimental chapters. The results in chapter 5 do not affect the two NMR chapters 4 and 3, therefore they are presented chronologically.

The two-phase morphology in terms of phase boundary movement in a thin film TiO_2 electrode during intercalation is studied by neutron reflectometry (NR) in chapter 7. In NR, the small incoming angles result in a depth-dependent probe at the nanometer length scale (roughly 1-100 nm). In this way, the Li-distribution in the electrode can be probed during the intercalation such to distinguish different intercalation mechanisms in terms of Li density profiles.

1.2.2   Li-ion mobility

One of the main topics of this thesis is the determination of the microscopic diffusion and its relation to the macroscopic diffusion, in particular taking the two-phase mor-

phology into account. Although many macroscopic (electrochemical) studies have been conducted, none exist on a microscopic level. The latter might be especially important considering the unexplained inconsistencies in the macroscopic results. In general, there are few experimental microscopic studies concerning the Li-ion dynamics in transition metal oxide electrode materials, in contrast to, for instance, hydrogen diffusion in metals and lithium diffusion in "fast ion conductors" (faster compared to anatase TiO_2). Both NMR and QENS have proven to be extremely useful in probing the diffusion of hydrogen and lithium on time scales in the range of microseconds to seconds for NMR and pico- to nanoseconds in the case of QENS.

In chapter 5 QENS results are described that illucidate the Li-dynamical behaviour in the picoseconds-nanoseconds range corresponding to small length scales (Å). These motions correspond to Li motions within an oxygen octahedron. This particular time- and length-scale is also covered by molecular dynamics (MD) simulations, which offer the opportunity to gain more detailed understanding. The MD calculations are presented in combination with the QENS data to underpin the interpretation of the QENS data.

The microscopic Li-ion dynamics of Li moving between different octahedra and the chemical environments within the separate phases is probed by NMR (chapter 3). The NMR experiments, described in chapter 4, cover even larger time and length scales, probing the Li-ion mobility between the two coexisting nano-sized phases. This is achieved by 2D-NMR, which measures the exchange between different environments (in this case different phases) at time scales of 1-1000 ms.

1.2.3   Electronic structure

The overview of literature concerning the electronic properties in section 1.1 demonstrates several points of view explaining the observed properties of lithiated anatase. The problem is calculating electronic orbitals and predicting the band character, in particular the degree of localization of the d-orbitals for transition metal oxides. Adding foreign ions (as in the present study of lithiated anatase TiO_2) makes it even more demanding because the otherwise regular structure becomes less regular due to partial occupations of sites.

What is required in such a case is a local probe that does not depend on long range order for it to work. In principle, the structure in the Ti pre-edge region of X-ray absorption spectroscopy (XANES) is a result of allowed transitions of the core electron towards unoccupied orbitals. Hence, besides complications regarding for instance multipole transitions, XANES is related to the local partial density of states. A comparison of the lithiated TiO_2 spectrum with the pure anatase TiO_2 spectrum can lead to additional understanding of the macroscopically observed properties like the optical absorption and the conductivity. This is the subject of chapter 6. The Li-ion electronic environment is probed with [7]Li nuclear magnetic resonance in chapter 3. The sensitivity of the NMR chemical shift allows the detection of very subtle effects in the chemical/electronic environment, like its temperature dependence. This offers complementary information to the XANES results.

Chapter 2

Techniques, theory and methods

2.1 Neutron scattering

2.1.1 Introduction

The importance of neutrons as a microscopic probe in condensed matter physics is based on its physical properties. The wavelength of thermal neutrons is of the order of the interatomic distances in condensed matter. The interference effects of neutron waves scattered by an arrangement of atoms in space carry structural information of the sample material. Unlike X-rays, neutrons interact with atomic nuclei via nuclear forces. The strength of this interaction varies randomly through the periodic system, in contrast to the direct proportionality of the X-ray interaction with the electron density. Therefore, depending on the atoms involved, numerous situations occur in which neutrons are favored over X-rays (or *vice versa*) for structural studies. The neutrality of neutrons allows them to penetrate deeply in the sample and the energy of thermal neutrons is of the same order as many processes in condensed matter. This means that neutron energy-dependent spectra can be related to the physical excitations in the sample. Finally, neutrons have a magnetic moment, and are sensitive to magnetic moments due to unpaired electrons and, consequently, can be used to determine the magnetic structure of solids. In combination with energy dependence the neutron magnetic moment can yield information about magnetic excitations. In general neutrons are difficult to produce, especially when compared to X-rays, this results in a relatively limited neutron flux that is available from neutron sources. As a consequence one often needs grams of sample, and measurements of hours up to days.

2.1.2 Elastic neutron scattering

Definitions

Imagine a beam of neutrons in a given direction, wave vector $\boldsymbol{k_0}$ (the neutron wavelength is $\lambda_0 = 2\pi/|\boldsymbol{k_0}|$) with a specific energy E_0 falling on the sample. At a certain angle we place a detector with an aperture $d\Omega$ relatively far from the sample so that the latter can be regarded as point scatterer. Using polar coordinates, the detector is at θ, ϕ relative to the incoming beam. The number of neutrons that we detect in solid angle $d\Omega$ having an energy between E_1 and $E_1 + dE_1$ and wave vector $\boldsymbol{k_1}$ is defined as the double differential

cross section:

$$\frac{d^2\sigma}{d\Omega dE} = \frac{I}{\Phi dE_1 d\Omega},$$
(2.1)

where Φ is the incoming neutron flux and I the number of neutrons per second that we detect. The momentum transfer of the neutron is defined as:

$$\hbar \boldsymbol{Q} = \hbar(\boldsymbol{k_1} - \boldsymbol{k_0}),$$
(2.2)

and its energy transfer is:

$$\hbar\omega = E_1 - E_0 = \frac{\hbar^2}{2m_n}(k_1^2 - k_0^2),$$
(2.3)

where m_n is the neutron mass and $\hbar$ Planck's constant divided by 2π. If we assume not to distinguish between the different neutron energies, that is we integrate equation 2.1 over the energy we find the definition of the differential cross section:

$$\frac{d\sigma}{d\Omega} = \int_0^\infty (\frac{d^2\sigma}{d\Omega dE_1})dE_1 = \frac{I}{\Phi d\Omega}.$$
(2.4)

We are then naturally lead to the definition of the total cross section, the total fraction of neutrons that is scattered by the sample, irrespective of their angle:

$$\sigma = \int (\frac{d\sigma}{d\Omega})d\Omega.$$
(2.5)

In the next section we look for an expression of the differential cross section.

Coherent and incoherent nuclear scattering

For the transition probability per unit time for transitions from state $|i>$ towards state $<f|$ first-order-perturbation quantum mechanics results in (Fermi's Golden rule):

$$W_{i\rightarrow f} = \frac{2\pi}{\hbar}|<f|V|i>|^2 \rho_{k_f}(E_f),$$
(2.6)

where V is the interaction potential and $\rho_{k_f}(E_f)$ the density of final states. In terms of the scattering of neutrons, $\rho_{k_f}(E_f)$ is the density of states characterized by neutrons that fall into the detector opening $d\Omega$ with an energy between E_f and $E_f + dE_f$. Using equation 2.6, we can rewrite the differential cross section equation 2.4 as:

$$(\frac{d\sigma}{d\Omega})_{i\rightarrow f} = \frac{W_{i\rightarrow f}}{\Phi(E_0)d\Omega}.$$
(2.7)

In case the incoming neutron wavelength is large compared to the nucleus, a good approximation of the interaction potential in equation 2.6 is the Fermi pseudo potential for a collection of nuclei with positions $\boldsymbol{R}_i$:

$$V(r) = \frac{2\pi\hbar^2}{m_n} \sum_i b_i \delta(\boldsymbol{r} - \boldsymbol{R}_i).$$
(2.8)

The (complex) constant b_i is called the scattering length; it is a measure of the interaction strength of neutrons with a specific atom. Working out equation 2.4 using equation 2.6 and 2.8 gives:

$$
\begin{aligned}
\frac{d\sigma}{d\Omega} &= \sum_i [<|b_i|^2> - |<b_i>|^2] + |\sum_i <b_i> e^{i\boldsymbol{Q}\cdot\boldsymbol{R}_i}|^2 \qquad (2.9)\\
&= (\frac{d\sigma}{d\Omega})_{inc} + (\frac{d\sigma}{d\Omega})_{coh}.
\end{aligned}
$$

The physical interpretation of the coherent part is the scattering from a system in which all the atoms have the average scattering length $<b_i>$. It is responsible for interference effects, i.e. the detected intensity will vary as a function of wave-vector transfer $\boldsymbol{Q}$. The incoherent part depends on the random deviations from the average scattering length and is independent of $\boldsymbol{Q}$. It adds up with the coherent part to yield the total scattering of the system.

Coherent elastic nuclear scattering by a crystal

In crystals the nuclear ordering is regular and all the structure information can be reduced to the definition of a unit cell. Introducing the crystal ordering into the coherent part of equation 2.9 result in Bragg's law of diffraction. Before we do so we need to introduce the reciprocal lattice. The definition of the unit cell is the smallest set of atoms that reproduces the crystal by translation of the unit cell by multiples of its dimensions. Given a unit cell with dimensions defined by the three vectors, $\boldsymbol{a_1}$, $\boldsymbol{a_2}$ and $\boldsymbol{a_3}$ the origin of each unit cell can be written as the lattice vector:

$$
\boldsymbol{L_{uvw}} = u\boldsymbol{a_1} + v\boldsymbol{a_2} + w\boldsymbol{a_3} \quad (u, v, w \ are \ integers). \qquad (2.10)
$$

If $\boldsymbol{r}_i$ is the position of atom i with respect to the origin of the unit cell, the position of an atom i in unit cell uvw can be expressed as:

$$
\boldsymbol{R}_i = \boldsymbol{r}_j + \boldsymbol{L_{uvw}}. \qquad (2.11)
$$

The reciprocal lattice is defined as:

$$
\boldsymbol{b_1} = 2\pi\frac{(\boldsymbol{a_2} \times \boldsymbol{a_3})}{v_a}, \quad \boldsymbol{b_2} = 2\pi\frac{(\boldsymbol{a_3} \times \boldsymbol{a_1})}{v_a}, \quad \boldsymbol{b_3} = 2\pi\frac{(\boldsymbol{a_1} \times \boldsymbol{a_2})}{v_a}, \qquad (2.12)
$$

where $v_a = \boldsymbol{a_1} \cdot (\boldsymbol{a_2} \times \boldsymbol{a_3})$ is the volume of the unit cell. From this definition one can derive:

$$
\boldsymbol{a}_\nu \cdot \boldsymbol{b}_\mu = 2\pi\delta_{\nu\mu} \quad (\nu, \mu = 1, 2, 3). \qquad (2.13)
$$

An arbitrary reciprocal lattice vector can be written as:

$$
\boldsymbol{G_{hkl}} = h\boldsymbol{b_1} + k\boldsymbol{b_2} + l\boldsymbol{b_3} \quad (h, k, l \ are \ integers). \qquad (2.14)
$$

Using equations 2.10, 2.13 and 2.14 the coherent part of equation 2.9 can be rewritten as:

$$
(\frac{d\sigma}{d\Omega})_{coh} = N\frac{(2\pi)^3}{v_a}|F(\boldsymbol{Q})|^2 \sum_{\boldsymbol{G_{hkl}}} \delta(\boldsymbol{Q} - \boldsymbol{G}_{hkl}), \qquad (2.15)
$$

where $F(\boldsymbol{Q})$ is the nuclear structure factor of the unit cell defined as:

$$F(\boldsymbol{Q}) = \sum_{j=1}^{n} <b_j> e^{i\boldsymbol{Q}\cdot\boldsymbol{r}_j}, \tag{2.16}$$

with n the number of nuclei per unit cell. The effect of thermal motion can be incorporated by a time-dependent term in the atom positions:

$$\boldsymbol{R}_j = \boldsymbol{r}_j + \boldsymbol{L_{uvw}} + \boldsymbol{u}_j(t). \tag{2.17}$$

This results in an extra factor in the structure factor, which generally is taken as the thermal average of the thermal displacement. Assuming isotropic thermal movement, one finds the Debye-Waller factor:

$$T_j(\boldsymbol{Q}) = \left\langle e^{i\boldsymbol{Q}\cdot\boldsymbol{u}_j} \right\rangle = e^{-\frac{1}{6}\boldsymbol{Q}^2\left\langle\boldsymbol{u}_j^2\right\rangle}. \tag{2.18}$$

We now find for the structure factor:

$$F(\boldsymbol{Q}) = \sum_{j=1}^{n} \langle b_j \rangle \, T_j(\boldsymbol{Q}) e^{i\boldsymbol{Q}\cdot\boldsymbol{r}_j}. \tag{2.19}$$

But what does equation 2.15 mean? Apparently, looking in the direction that is defined by $\boldsymbol{Q} = \boldsymbol{k_1} - \boldsymbol{k_0}$, there can only be neutron intensity if $\boldsymbol{Q}$ matches a reciprocal lattice vector $\boldsymbol{G}_{hkl}$. In other words the reciprocal lattice vectors, $(\boldsymbol{b_1}, \boldsymbol{b_2}, \boldsymbol{b_3})$, that result from the real-space unit cell, determine the possible directions in which the neutrons scatter and "reflections" are found. It is convenient to index each reflection that is allowed by the unit cell, irrespective of its contents, with the to $\boldsymbol{G}_{hkl}$ corresponding hkl values. Whether or not an actual reflection hkl will occur with finite intensity depends on the nuclear structure factor, thus the contents of the unit cell. This becomes more clear if we define the atomic positions in the unit cell as $\boldsymbol{r}_j = x_j\boldsymbol{a_1} + y_j\boldsymbol{a_2} + z_j\boldsymbol{a_3}$ ($0 \leq x_j, y_j, z_j \leq 1$). The structure factor, equation 2.19, can then be rewritten as:

$$F(\boldsymbol{Q} = \boldsymbol{G}_{hkl}) = \sum_{j=1}^{n} <b_j> T_j(\boldsymbol{G_{hkl}}) e^{i2\pi(hx_j+ky_j+lz_j)}. \tag{2.20}$$

Depending on the positions (x_j, y_j, z_j) in the unit cell and the values of hkl the structure factor can becomes zero and no neutrons will scatter, although the condition $\boldsymbol{Q} = \boldsymbol{G}_{hkl}$ is fulfilled. The positions of the atoms in the unit cell determine the allowed reflections with the reflection index, hkl. The relative reflection intensity is directly related to the coherent scattering lengths of the atoms and the Debye-Waller factors.

Until now we assumed scattering from a single crystal. In many cases one will have a powder sample in which the orientation of the crystalline particles is randomly distributed. The reciprocal space then transforms from specific points hkl to concentric spheres with radius $|\boldsymbol{G}_{hkl}|$ with a well defined incoming k_0, k_1 should have the same length and lie on this sphere. In real space this results in a cone of scattered intensity, the Debye-Scherrer cone. This means for a powder diffraction experiment that just one angle scan suffices to detect many reciprocal lattice vectors $\boldsymbol{G}_{hkl}$ provided that

$|\boldsymbol{G}_{hkl}| < \boldsymbol{G}_{max}$. The angle that needs to be scanned is the angle between the incoming $\boldsymbol{k_0}$ and outgoing neutron vector $\boldsymbol{k_1}$ which is defined as 2θ. A more fundamental unit is the d-spacing which refers to the length scale on which a certain reflection scatters, it is defined as $d_{hkl} = 2\pi/|\boldsymbol{G}_{hkl}|$. Geometrical consideration of the scattering condition $\boldsymbol{Q} = \boldsymbol{G}_{hkl}$ leads to:

$$|G_{hkl}| = 2k_0 \sin\theta = \frac{4\pi}{\lambda} \sin\theta. \tag{2.21}$$

This illustrates the two possible methods to probe the reciprocal space. One can determine the angle θ of the scattered neutrons while the neutron wave length λ is kept constant, thus using a monochromatic beam. Alternatively, a white beam can be used if it is pulsed. In that way the neutron energy can be determined by measuring the time of arrival relative to the start of the pulse, the time of flight method (TOF). From the TOF one determines the neutron velocity and via de Broglie's equation λ. A general treatment of neutron scattering can be found in several standard works, for instance in "Thermal Neutron Scattering" [31].

Density difference analysis of powder data

The nuclear structure factors, $F(\boldsymbol{G}_{hkl})$ are directly related to the periodic part of real-space atomic density in a crystal via a Fourier transformation [32]:

$$\rho(\boldsymbol{r}) = \frac{1}{v_a} \sum_{h,k,l} F(\boldsymbol{G}_{hkl}) e^{i\boldsymbol{G}_{hkl}\cdot\boldsymbol{r}_j} = \frac{1}{v_a} \sum_{h,k,l} F(\boldsymbol{G}_{hkl}) e^{i2\pi(hx_j+ky_j+lz_j)} \tag{2.22}$$

If the unit cell dimensions are known, each reflection can be indexed with its hkl value. Collecting the reflections $F(\boldsymbol{G}_{hkl})$ thus gives the possibility to determine the real-space scattering length density in the unit cell. However, what is measured is $|F(\boldsymbol{G}_{hkl})|^2$, hence the phase information is lost. For centro-symmetric structures the phase-angle of the structure factor is limited to 0° or 180°, depending on the hkl values. In practice one often encounters the situation that part of the unit cell contents is known, and one needs to determine the location of the missing atom(s). In that case it is particularly useful to Fourier transform the difference between the observed structure factors, F_O, and the structure factors calculated from the known part of the unit cell, F_C:

$$\Delta\rho(\boldsymbol{r}) = \frac{1}{v_a} \sum_{h,k,l} [F_O(\boldsymbol{G}_{hkl}) - F_C(\boldsymbol{G}_{hkl})] \, e^{i2\pi(hx_j+ky_j+lz_j)} \tag{2.23}$$

This density difference intensity (or density difference map) equals the scattering length density of the atoms that were not used in the calculated model. Again, we assumed single crystal data. The same method can be applied with powder data, as long as we have a list of hkl reflections. However, to go from the one dimensional diffraction data to the three dimensional $\Delta\rho(\boldsymbol{r})$ one needs symmetry relations of the unit cell contents, the space group. Care should be taken with this method because the symmetry operations of the space group may project density where in reality there is none. Also care should be taken of the real-space resolution of density difference maps, the range of the reciprocal space that is measured determines the positional accuracy of the scattering density, it is approximately equal to $\Delta\boldsymbol{r} = 0.715 \times 2\pi/|\boldsymbol{G}_{max}|$ [32].

2.1.3   Quasi-elastic incoherent neutron scattering

In section 2.1.2 it was assumed that there was no energy transfer during the scattering process. The double differential cross section does allow for energy transfer, equation 2.1, and it can be derived using equation 2.6 and introducing the conservation law for energy as a δ function; $\delta(\hbar\omega - E_0 + E_1)$ where $\hbar\omega$ is the energy transfer, E_0 the incoming and E_1 the outgoing neutron energy: This leads to the general double differential cross-section for neutron-nucleus scattering:

$$\frac{d^2\sigma}{d\Omega dE_1} = \frac{k_1}{k_0}\frac{N}{\hbar}\left(\frac{\sigma_{coh}}{4\pi}S_{coh}(\boldsymbol{Q},\omega) + \frac{\sigma_{inc}}{4\pi}S_{inc}(\boldsymbol{Q},\omega)\right), \qquad (2.24)$$

where N is the total number of particles and $S_{coh,inc}(\boldsymbol{Q},\omega)$ are the so called dynamical scattering functions which can be expressed by the space and time Fourier transformation of correlation functions $G(\boldsymbol{r},t)$:

$$S_{coh}(\boldsymbol{Q},\omega) = \frac{1}{2\pi}\int G(\boldsymbol{r},t)e^{i(\boldsymbol{Q}\cdot\boldsymbol{r}-\omega t)}d\boldsymbol{r}dt, \qquad (2.25)$$

$$S_{inc}(\boldsymbol{Q},\omega) = \frac{1}{2\pi}\int G_s(\boldsymbol{r},t)e^{i(\boldsymbol{Q}\cdot\boldsymbol{r}-\omega t)}d\boldsymbol{r}dt. \qquad (2.26)$$

The pair correlation function $G(\boldsymbol{r},t)$ is the conditional probability to find two particles at a distance $\boldsymbol{r}$ and at different times t. The self correlation function $G_s(\boldsymbol{r},t)$ represents the conditional probability for finding the same particle at position $\boldsymbol{r} = 0$ at $t = 0$ and at a later time t at distance $\boldsymbol{r}$. The coherent scattering from a perfect harmonic solid results in scattering from collective phenomena like the elastic Bragg intensities (section 2.1.2) and inelastic scattering from phonons at well defined energy transfers. Here we are interested in the incoherent scattering function for random diffusive motions. The incoherent part is related to uncorrelated diffusive motion, hence it is related to the diffusion of single particles.

We will discuss two types of diffusion, i.e. random continuous diffusion and hopping diffusion. The former one is governed by Fick's law and results in the quasi-elastic incoherent dynamic scattering function:

$$S_{inc}(Q,\omega) = \frac{1}{\pi}\frac{DQ^2}{(DQ^2)^2 + \omega^2}, \qquad (2.27)$$

with D the diffusion coefficient. $S_{inc}(Q,\omega)$ has a Lorentzian shape with a full width at half maximum (FWHM) $2DQ^2$.

Hopping diffusion of atoms from one site to another leads to a sum of an elastic and a, Lorentzian shaped, quasi-elastic part:

$$S_{inc}(Q,\omega) = A(Q)\delta(\omega) + \frac{A(Q) - 1}{\pi}\frac{1/\tau}{(1/\tau)^2 + \omega^2}, \qquad (2.28)$$

with τ the mean residence time at one site. The elastic incoherent structure factor (EISF) $A(Q)$ is determined by the geometry of the hopping diffusion. The EISF can be interpreted as the probability that the diffusing particle remains within a box defined by the Q scale. Note that the time window accessible by the experiment is determined

by both by the energy resolution ($\Delta\omega$) and the maximum ω value of the spectrometer used. Processes that occur at timescales relatively fast compared to the energy transfer, $\hbar\omega$, will fall outside the time window, whereas the intensity of relatively slow processes compared to the resolution will end up in the elastic peak.

To give an example of an explicit form of the EISF: If we consider a system were n sites, a distance a apart, are available for hopping diffusion within the time window accessible, the EISF is given by:

$$A(Q) = \frac{1}{n} + \frac{n-1}{n}\frac{\sin Qa}{Qa}. \tag{2.29}$$

This expression is valid for n identical sites. For a system with different occupancies for different sites, $A(Q)$ has to be adjusted. E.g., if n=2 and the occupancies are defined by $1 - \epsilon$ and $1 + \epsilon$, respectively, the EISF is:

$$A(Q) = \frac{1+\epsilon^2}{2} + \frac{1-\epsilon^2}{2}\frac{\sin Qa}{Qa}. \tag{2.30}$$

A complete work on quasi-elastic neutron scattering is written by M. Bee [33].

2.1.4 Neutron reflectometry

The neutron wave character allows the description of neutron reflectometry completely analogous to the reflection and refraction of light. The starting point is the one-dimensional stationary Schrödinger equation for the neutron wave amplitude:

$$-\frac{\hbar^2}{2m_n}\frac{d^2\Psi}{dz^2} + V(z)\Psi = \frac{\hbar^2}{2m}q_0^2\Psi, \tag{2.31}$$

where $V(z)$ is the interaction potential of the neutrons with the reflecting material, m_n is the neutron mass and q_0 is the z-component of the incoming neutron wave vector k_0, see figure 2.1, defined as:

$$q_0 = \frac{2\pi sin\theta}{\lambda}. \tag{2.32}$$

We assume $V(z)$ does not depend on both x and y, in other words we are reflecting on the $x-y$ plane of a material that only changes composition in the z direction.

The position dependent interaction with the medium can be described with the optical potential $V(z)$ defined by the refractive index:

$$n(E) = 1 - \delta(E) - \imath\beta(E). \tag{2.33}$$

In this we assume no energy transfer between the neutrons and matter in which case:

$$\delta = \frac{\lambda^2}{2\pi}\sum_j N_j(z)b_{c,j}, \tag{2.34}$$

and:

$$\beta = \frac{\lambda^2}{2\pi}\sum_j N_j(z)b_{a,j}, \tag{2.35}$$
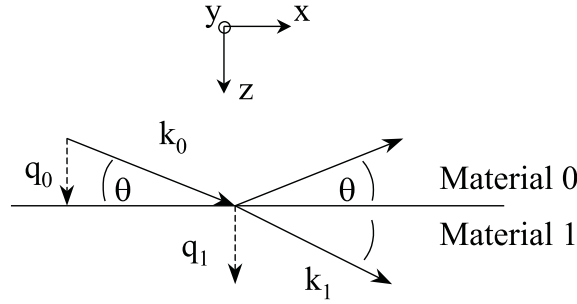
Figure 2.1: *Definition of the wave vector perpendicular to the reflecting interface.*

where $N_j(z)$ is the atom number density, b_c is the coherent scattering length, and b_a is the imaginary part of the potential that incorporates absorption. The potential can than be defined as:

$$V(z) = 2\pi \frac{\hbar^2}{m_n} \sum_j N_j(z)(b_c + ib_a)_j. \tag{2.36}$$

In neutron reflectometry a practical definition for the potential is the scattering length density:

$$\Gamma(z) = \frac{2m_n}{\hbar^2} V(z) = 4\pi \sum_j N_j(z)(b_c + ib_a)_j. \tag{2.37}$$

The z-component of the wave vector inside the material can then be expressed as:

$$q(z) = \sqrt{q_0^2 - \Gamma(z)}. \tag{2.38}$$

In general, equation 2.31 cannot be solved analytically for a specific $\Gamma(z)$. However, discrete homogeneous layers offer the possibility to solve the Schrödinger equation for a constant potential in each layer. The solutions are coupled through the continuity and differentiability boundary conditions at each interface:

$$\Psi(z)_i|_{z=z_i} = \Psi(z)_{i+1}|_{z=z_i} \quad and \quad \frac{d\Psi(z)_i}{dz}|_{z=z_i} = \frac{d\Psi(z)_{i+1}}{dz}|_{z=z_i}, \tag{2.39}$$

where z_i is the interface between layer i and $i+1$. The general solution of equation 2.31 for a constant potential Γ_i in layer i is:

$$\Psi(z) = A_i e^{\imath q_i z} + B_i e^{-\imath q_i z}, \tag{2.40}$$

where $q_i = \sqrt{q_0^2 - \Gamma_i}$. Above the interface, $z < 0$ in figure 2.1, the first term represents the incoming beam and the second the reflected beam. In an actual measurement the amplitude of the reflected wave is measured, this is called the reflectivity $R = |B_0|^2$, assuming $A_0 = 1$. The most simple reflection case is that from a perfect interface between two media, incoming medium: i=0 and reflecting medium : i=1, which results in Fresnel's law:

$$R = \left| \frac{q_1 - q_0}{q_1 + q_0} \right|^2. \tag{2.41}$$
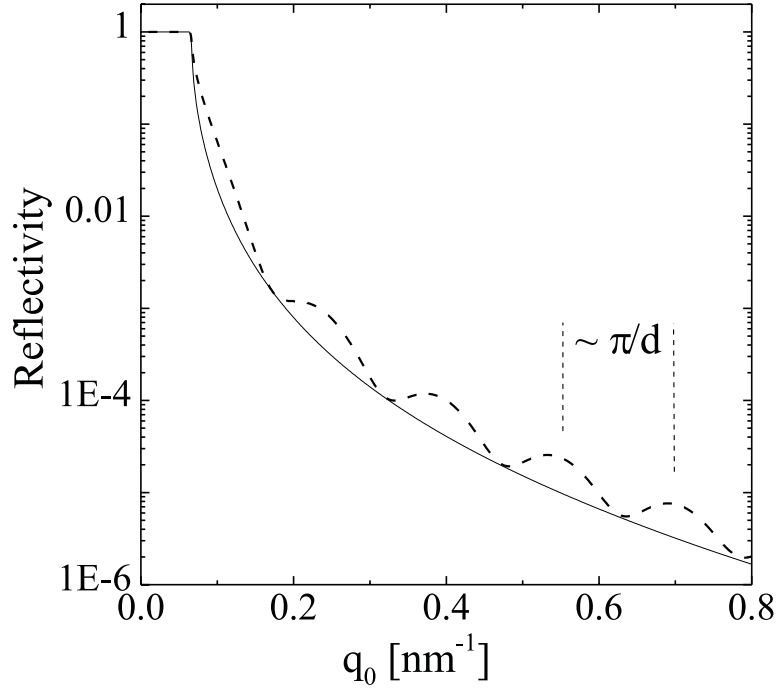
Figure 2.2: *Calculated neutron reflection, solid line: quartz substrate, dashed line: 20 nm gold layer on top of a quartz substrate. For large q_0, the period of the fringes is inversely proportional to the thickness of the layer.*

By varying the z-component of the neutrons, wave vector q_0, the reflectivity decreases with increasing q_0, for instance in figure 2.2 Fresnel's law is calculated for quartz. Either the angle, θ, or the wavelength can be varied to measure R as a function of q_0, c.f. equation 2.32. The critical angle is determined by the substrate, Γ_{sub}. Below the critical angle, $\theta_c = \sqrt{\Gamma_{sub} - \Gamma_0}$, total reflection occurs. In case $\Gamma_{sub} < \Gamma_0$ no total reflection occurs.

Introducing one layer between the incoming medium and the substrate results in a reflectivity:

$$R = \left| \frac{R_0 + R_1 e^{2iq_{lay}d_{lay}}}{1 + R_0 R_1 e^{2iq_{lay}d_{lay}}} \right|^2, \tag{2.42}$$

where R_0 and R_1 represent the Fresnel reflectivity between the incoming medium and the layer, and between the layer and the substrate, respectively, q_{lay} is the z-component of the neutron wave vector inside the layer and d_{lay} the layer thickness. If the layer thickness is much larger than the coherence length along z of the reflecting neutrons and $\Gamma_{lay} > \Gamma_{sub}$, the layer will determine the critical angle. For thermal neutrons the coherence length is in the order of micrometers and the coherence length along z is thus of the order $\mu\text{m}\cdot sin\theta \approx\approx 10\text{nm}-100\text{nm}$. The layer introduces interference effects between the reflecting and the transmitted amplitudes which results in the fringes in the reflectivity as a function of q_0. As an example the calculated reflectivity of a 20 nm gold layer on top of a quartz substrate is shown in figure 2.2. In general the spatial resolution of the reflectivity depends on the maximal q at which the reflectivity is measured, roughly

the minimal length scale probed is $2\pi/q_{max}$. The reflectivity strongly depends on the layer thickness and all the potentials involved. Therefore, neutron reflectivity contains information of the nm-scaled scattering length density profile in the reflecting sample. For extensive information concerning reflectometry a number of standard works exist, for instance by J. Lekner [34].

2.2   Solid-state nuclear magnetic resonance

2.2.1   Introduction

An atomic nucleus possesses an overall spin if it exists of an odd number of neutrons plus protons (half integer spin), or if both number of protons and neutrons are odd (integer spin). When a steady magnetic field B_0 is applied to a nucleus with spin quantum number I, quantum mechanics states that the nuclear spin energy level splits into $2I+1$ equidistant energy levels as a result of the interaction between the spin and the field (Zeeman interaction), for instance figure 2.3 (a) for $I = 1/2$. The energy required for a transition between two of these energy levels corresponds to radio frequency (r.f.) waves with a frequency depending on the magnetic field applied in practice. For instance the transition or "resonance" for hydrogen (^{1}H) in a field of 14.1 Tesla occurs at a frequency of 600 MHz of the r.f. field.

In a free nucleus one would indeed measure the Zeeman energy, however, in molecules and in solids many interactions play a part in shifting, splitting and broadening of the energy levels. Clearly, this will change the absorption spectrum measured. The influence of the environment of the nucleus on its spin transitions offers the opportunity to study its surroundings. Thereby NMR allows in principle to study the electronic and magnetic environment as well as the local atomic configuration. In addition, dynamic processes may be studied if these processes influence the relaxation of the nuclear spins.

In this chapter, the basic principle and the physical aspects that are encountered in solid state NMR are sketched. First, the basic NMR experiment will be described, paragraph 2.2.2. Next is a short review on a microscopic level of the main interactions in solids that influence the observed NMR signal, paragraph 2.2.3. In practice we always deal with a macroscopic sum of nuclei rather than a single nucleus. A short introduction to the classical treatment of a macroscopic nuclear spin system is given in paragraph 2.2.4. After external disturbance fluctuating processes causing spontaneous transitions eventually cause the system to return to equilibrium. How these systems relax to thermal equilibrium and the influence of diffusing nuclei is illustrated in paragraph 2.2.5. At the end of the chapter a few for this thesis relevant experimental NMR techniques are shown in section 2.2.6.

2.2.2   Description of the NMR experiment

It is useful to start with introducing the method with which NMR spectra are recorded as to create a context for the rest of the chapter. This will be done in a qualitative way, a more precise picture will be given in section 2.2.4. A nucleus with $I = 1/2$ in a static magnetic field B_0 will result in two energy levels associated with the quantum numbers $m = -1/2$ and $1/2$. Absorption will occur if the energy of the r.f. radiation matches

the energy for a nuclear spin transition between the two levels, hence $E_{r.f} = \hbar\omega_L = \Delta E = \gamma\hbar B_0$. In that case a nuclear spin will flip its direction from the energetically more favorable orientation parallel to the field to anti-parallel orientation, see figure 2.3 (a). The most obvious method to measure the absorption spectrum is to sweep the r.f. frequency such that it includes the resonance condition. A more technically sophisticated method is pulse or Fourier NMR which will be described next. A short pulse with r.f. frequency corresponding to the central value of the range of expected absorption frequencies has a band width inversely proportional to the pulse length. Hence, a large spectral width can be probed by a single pulse if it is short enough. Such a pulse will cause the macroscopic nuclear magnetization, initially aligned with the static field, to rotate towards the plane perpendicular to the applied field, see figure 2.3 (b). The combination of the the pulse length and the power of the r.f. pulse determines the amount of spin transitions. A pulse with duration such that it rotates the macroscopic magnetization exactly in the plane perpendicular to the applied field is referred to as a $\pi/2$ pulse. Due to the applied field the macroscopic magnetization will precess in the plane with the Larmor frequency determined by the absorption condition, $\hbar\omega_L = \gamma\hbar B_0$. A coil placed in the precession plane, figure 2.3 (b), will pick up an induced current as a result of the precessing macroscopic magnetization. The result will be a damped oscillating signal as shown in figure 2.3 (c), which is called the free induction decay (FID). Fourier transform of the signal will result in the absorption spectrum, figure 2.3 (d). In general the frequency axis is expressed in parts per million (ppm) of the observed frequency scaled by the Larmor precession frequency of the same nucleus in a reference compound. Many interactions with the environment will cause a distribution in the individual nuclear precession frequencies. As a result the macroscopic magnetization de-phases in the rotating plane which leads to the damped FID signal. In some cases the damping can be described by just one time constant, T_2 the transverse or spin-spin relaxation time. In addition the magnetization relaxes back to align with the applied field due to the interactions of the individual spins with the environment. This time constant, T_1 is called the longitudinal or spin-lattice relaxation. Relaxation is further discussed in paragraph 2.2.5.

2.2.3   Interactions in solids

Zeeman interaction

The possession of both spin angular momentum $\boldsymbol{J}$ and charge of a nucleus is expressed in terms of the magnetic moment, $\boldsymbol{\mu} = \gamma\boldsymbol{J}$, where γ is the isotope dependent magnetogyric ratio. $\boldsymbol{J}$ is given in units of $\hbar$ and the maximal observable component is $I\hbar$, where I is the nuclear spin quantum number of a specific isotope. If a constant magnetic field is applied the interaction between the nuclear spin and the applied field is expressed by the Hamiltonian [35]:

$$\widehat{H}_0 = -\boldsymbol{\mu} \cdot \boldsymbol{B_0} = -\gamma\boldsymbol{J} \cdot \boldsymbol{B_0} = -\gamma\hbar\boldsymbol{I} \cdot \boldsymbol{B_0}. \tag{2.43}$$

The interaction results in $2I + 1$ energy levels $E_m = -\gamma\hbar B_0 m$ where m is the quantum number associated the nuclear spin components parallel to the applied field. The quantum number m can have the values $-I, -I+1, ..., I-1, I$. A nuclear spin parallel to the
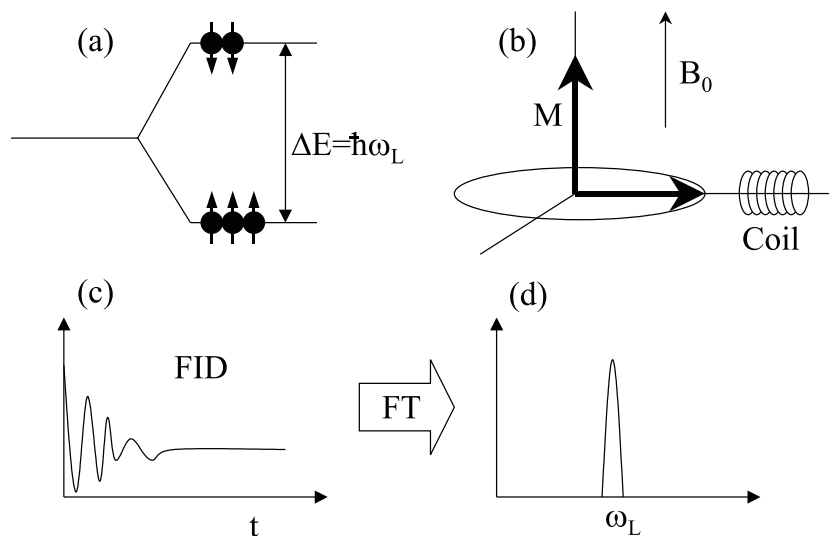
Figure 2.3: *(a) Nuclear spin energy for an atom with $I = 1/2$ in a static magnetic field B_0. (b) Macroscopic magnetization aligned with the field B_0 and rotated in the plane perpendicular to the field, and a conducting coil placed in the plane to pick up the induced current resulting from the rotating macroscopic magnetization. (c) FID recorded by the coil. (d) Fourier transform of the FID.*

applied field leads to lower energy states and in a macroscopic system the occupation of spin levels follows the Boltzmann law. The energy difference between these levels, $\Delta E = \gamma \hbar B_0$, determines the resonance condition for applied r.f. fields as described in the previous section. In the high field approximation the Zeeman interaction dominates the position of the energy levels and other interactions can be treated as perturbation. Therefore, in first order, the Zeeman interaction determines the position in frequency of the resonance line.

Chemical shift

In general, the observed NMR (Larmor) frequency differs slightly from the theoretical value γB_0 for the free nucleus in a magnetic field B_0. This is the result of an additional field $-\sigma B_0$, originating from the electrons surrounding the nucleus, that shields the nucleus from the applied field. It is essential to notice that the additional field is proportional to the applied field such that the local field becomes $B_{local} = (1 - \sigma)B_0$. This causes a shift from γB_0, the chemical shift, in the observed resonance frequency. In molecules and solids the chemical shift is in general anisotropic and can be expressed as a tensor $\widetilde{\widetilde{\sigma}}$. The Hamiltonian in equation 2.43 corrected for the chemical shift (or shielding) then yields [35]:

$$\widehat{H}_0 = -\gamma \hbar \boldsymbol{I} \cdot (1 - \widetilde{\widetilde{\boldsymbol{\sigma}}}) \cdot \boldsymbol{B_0}. \tag{2.44}$$

The additional field can be either diamagnetic or paramagnetic. The diamagnetic component of the chemical shift depends on the ability of the applied field to induce an electronic current in the atom or molecule that reduces the local field. Roughly speaking

the diamagnetic contribution is proportional to the electron density at the resonance nucleus. The paramagnetic contribution to the additional field arises from the possibility that the applied field excites electrons to unoccupied orbitals, hence creating an effective magnetic moment aligned with the applied field. When the local symmetry is less than cubic the anisotropy of the chemical shift causes different orientations to have different resonance frequencies. In poly-crystalline materials this leads to anisotropic chemical shift broadening of resonance lines.

Paramagnetic and Knight shift

In the previous section the influence of electrons in closed shells was considered, which lead to an applied-field-dependent shift. Both paramagnetic unpaired electrons in localized orbitals and unpaired conduction electrons can strongly influence the local field experienced by the nuclei. This direct magnetic coupling of the unpaired electron spin and the nuclear spin (hyperfine interaction, Fermi interaction or contact interaction) causes large shifts in the observed resonance frequency. For localized unpaired electrons this results in a Curie-Weiss temperature dependent chemical shift [36]:

$$\frac{\Delta\omega}{\omega_0} = \frac{g\mu_B}{3}\frac{J(J-1)}{k_B T}\left\langle |u(0)|^2 \right\rangle, \tag{2.45}$$

where ω_0 is the unshifted resonance frequency, $\left\langle |u(0)|^2 \right\rangle$ is the magnitude of the squared unpaired electron wave function at the nucleus, g the free electron g factor, μ_B the Bohr magneton, J the total electronic angular momentum, k_B Boltzmann's constant and T the temperature. The polarization of the unpaired electron density of conduction electrons is the result of an imbalance in the electronic spin populations due to the applied field. This results in Pauli paramagnetism. The paramagnetic induced shift due to unpaired conduction electrons is called Knight shift and equals [36]:

$$K = \frac{\Delta\omega}{\omega} = \frac{8\pi}{3}\chi_e \left\langle |u(0)|^2 \right\rangle_{\varepsilon_F}, \tag{2.46}$$

where χ_e is the Pauli susceptibility of the conduction electrons, and $\left\langle |u(0)|^2 \right\rangle_{\varepsilon_F}$ represents the electron density with energy close to the Fermi level ε_F. In contrast to the susceptibility of localized paramagnetic electrons given by Curie's law, equation 2.45, the Pauli paramagnetic shift due to electrons is essentially independent of temperature. However, in semi-conductors the density of the conduction band electrons displays an intrinsic temperature dependence that is related to the value of the band gap. As a consequence the Knight shift will display the same temperature dependence. The unpaired electron density can only affect the field at the nucleus if it has a non-vanishing electron density at the nucleus. Therefore, in principle only unpaired s-orbitals can contribute to this shift. However, indirect coupling of other orbitals with s-orbitals through core polarization can also result in Knight shifts [36].

Magic angle spinning

Before proceeding with two important interactions that broaden nuclear magnetic resonance lines in solids, dipolar and quadrupolar interactions, magic angle spinning (MAS)

is introduced. This technique is of considerable importance in solid state NMR as it can reduce the generally large line-width in solids. This often enables the assignment of resonances that otherwise would overlap and could not be distinguished. In liquids and gases, fast random diffusion effectively averages anisotropic interactions that can be described by rank-2 tensors. Such interactions are: dipole interaction, first order quadrupolar interaction and chemical shift anisotropy. Working out a rank-2 tensor results in a frequency shift from ω_0 that is proportional to $(3cos^2\theta - 1)$ where θ is the angle between the nuclear moment and the applied field. Magic angle spinning refers to rotating the sample under $\theta_{MAS} = 54.74°$ with a frequency ω_{spin}. On a time scale $t >> 1/\omega_{spin}$ the nuclear spins experience an averaged environment that is oriented under an angle θ_{MAS} with respect to the applied field. As a result the angle dependent term $(3cos^2(\theta_{MAS}) - 1)$ vanishes, and all nuclei resonate near $\omega_0 \pm n\omega_{spin}$. The width of a single resonance line, expressed in Hz, can only be effectively averaged if the MAS frequency is larger. If the MAS frequency is smaller than the static line width or spectral distribution spinning side bands occur at multiples of the spinning frequency, an example is shown in figure 2.4. MAS is particular useful in solids, where in many cases chemical shift anisotropy, dipole interactions and quadrupole interactions are dominant.

Dipole-dipole interaction

The main interaction between the spins of two nuclei, $\boldsymbol{I}$ and $\boldsymbol{S}$, is the dipole-dipole coupling between their magnetic moments. The magnitude of the interaction depends on the relative orientations of the spins with respect to each other and is expressed in terms of the dipole Hamiltonian:

$$\widehat{H}_D = \frac{\mu_0}{4\pi}\hbar^2\gamma_I\gamma_S\boldsymbol{I} \cdot \widetilde{\widetilde{\boldsymbol{D}}} \cdot \boldsymbol{S}, \qquad (2.47)$$

where μ_0 is the magnetic permeability in vacuum, $\widetilde{\widetilde{D}}$ the dipolar coupling tensor and γ_i the magnetogyric ratio for nucleus i. Rapid tumbling of molecules in gases and liquids averages out the distribution and results in a narrow resonance. The complications of solving the time independent Schrödinger equation for the Hamiltonian in equation 2.47 can be avoided by the method of moments by Van Vleck. By assuming a resonance frequency distribution, the second moment of the frequency distribution is related to the line width, Van Vleck's result for identical nuclei is [37]:

$$M_2 = \left\langle \Delta f^2 \right\rangle_{II} = \frac{3}{4} \left(\frac{\mu_0}{4\pi}\right)^2 \gamma_I^4\hbar^2 I(I + 1) \sum_k \frac{(1 - 3\cos^2\theta_{jk})^2}{r_{jk}^6}, \qquad (2.48)$$

where γ_I is the magnetogyric ratio of the nucleus, r_{jk} the distance between two atoms, j and k, and θ_{jk} is the angle between the vector connecting the two atoms and the direction of the applied static field. As an example we calculate the line width assuming a Gaussian resonance line shape for ^{7}Li atoms in a cubic lattice, lattice parameter $d = 2.5$ Å for a poly-crystalline sample. For a poly-crystalline sample the $(1 - 3\cos^2(\theta_{jk}))^2$ term averages to 4/5 and assuming a cubic lattice with lattice constant d, $\sum_k(1/r_k^6) = 8.5/d^6$. This leads to $< \Delta f^2 >^{1/2} = 808.8$ Hz, where we used $\gamma_{Li} = 1.655 \cdot 10^7$ Hz·T^{-1} and $I_{Li} = 3/2$. The Gaussian line shape relates the line width, δ (FWHM), to the second moment as

$\delta = 2\ln(2)M_2^{1/2}$. This results in $\delta = 1.12$ kHz. For comparison, it is interesting to note that two interacting ^{7}Li nuclei lead to $\delta = 0.416$ kHz, much less than a whole lattice with ^{7}Li. For a system with unlike spins, where nucleus I is in resonance, the contribution of the spins with quantum number S to the second moment is:

$$M_2 = \left\langle \Delta f^2 \right\rangle_{IS} = \frac{1}{4}\left(\frac{\mu_0}{4\pi}\right)^2 \gamma_I^2 \gamma_S^2 \hbar^2 S(S+1) \sum_k \frac{(1 - 3\cos^2\theta_{jk})^2}{r_{jk}^6}, \qquad (2.49)$$

where γ_I and γ_S are the magnetogyric ratios of the two types of nuclei. The total second moment of the resonance line of nuclear spin quantum number I in case both like and unlike spins are present is given by the sum of the second moment contributions.

Quadrupole interaction

Some nuclei with $I > 1/2$ possess an electric quadrupole moment which expresses the fact that the charge density, $\rho(r)$, inside the nucleus is non-spherical. The quadrupole moment is defined as:

$$eQ = \int \rho(\boldsymbol{r})(3z^2 - \boldsymbol{r}^2)d\boldsymbol{r}, \qquad (2.50)$$

where z is parallel to the nuclear spin direction $\boldsymbol{I}$. In a crystal with less than cubic symmetry the interaction of the nuclear quadrupole moment with the nonuniform electric field gradient produced by the crystal results in $2I + 1$ quantized energy levels even in absence of an external magnetic field. The quadrupole interaction of the nucleus and the electric field gradient is expressed in the quadrupole Hamiltonian [37]:

$$\widehat{H}_Q = \frac{eqQ}{4I(2I+1)\hbar}\boldsymbol{I} \cdot \widetilde{\widetilde{\boldsymbol{V}}} \cdot \boldsymbol{I}, \qquad (2.51)$$

where $\widetilde{\widetilde{\boldsymbol{V}}}$ is the electric field gradient tensor and $eq = V_{zz}$ and $\eta = \frac{V_{xx} - V_{yy}}{V_{zz}}$ is the asymmetry parameter, with $V_{\alpha\beta} = \frac{d^2E}{d\alpha d\beta}$ where E is the electric field. In a relatively large applied field the quadrupole interaction is an order of magnitude smaller than the Zeeman interaction in which case the distortion of the energy levels can be calculated with first order perturbation theory.

For a $I = 3/2$ nucleus, e.g. ^{7}Li, the Zeeman interaction results in four equidistant energy levels associated with quantum numbers $m = [-3/2, -1/2, 1/2, 3/2]$, see figure 2.4 (a). Because only transitions between neighboring energy levels can be induced by a r.f. pulse the three transitions will all occur at the same frequency. First order quadrupole interaction shifts all pairs $\pm m$ by the same amount. As a result the central $1/2 \leftrightarrow -1/2$ transition is not affected, in contrast to the $-3/2 \leftrightarrow -1/2$ and $1/2 \leftrightarrow -3/2$ transitions, see figure 2.4 (a). The frequency shifts are related to the nuclear electric quadrupole interaction as follows [37]:

$$\omega_{-\frac{1}{2},-\frac{3}{2}} = \omega_0 + \frac{1}{4}\left(\frac{e^2qQ}{\hbar}\right)\left[(3cos^2\theta - 1) + \eta sin^2\theta cos2\phi\right], \qquad (2.52)$$

$$\omega_{\frac{1}{2},-\frac{1}{2}} = \omega_0, \qquad (2.53)$$

$$\omega_{\frac{1}{2},\frac{3}{2}} = \omega_0 - \frac{1}{4}\left(\frac{e^2qQ}{\hbar}\right)\left[(3cos^2\theta - 1) + \eta sin^2\theta cos2\phi\right], \qquad (2.54)$$
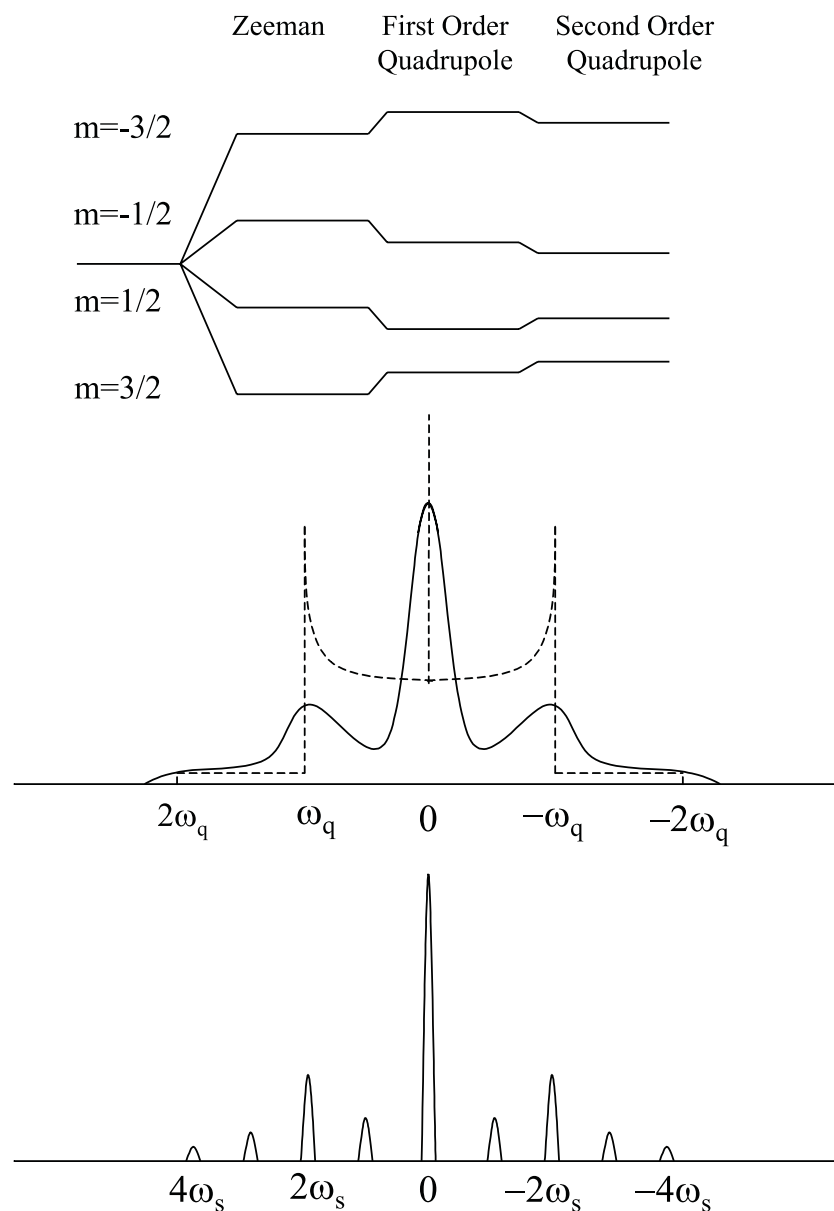
Figure 2.4: *Top: Nuclear spin energy level splitting of an I = 3/2 nucleus in a magnetic field, and first and second order perturbation of the levels if an electric field gradient is present at the nucleus. Middle: Dashed line: theoretical first order quadrupole perturbed powder spectrum, $\omega_q = \frac{1}{4}\left(\frac{e^2 qQ}{\hbar}\right)[(3cos^2\theta - 1) + \eta sin^2\theta cos2\phi]$. Solid line: Sketch of the powder spectrum that might be encountered in practice. Bottom: Magic angle spinning side band spectrum of the sketched powder spectrum, where ω_s is the spinning frequency.*

where the units of ω are radians per second, θ and ϕ are the polar and azimuthal angles of the orientation of the principle axis system (of the quadrupole moment) in the laboratory coordinate system (z-axis parallel to B_0). The two satellite transitions, $\omega_{\mp\frac{1}{2}\mp\frac{3}{2}}$, are thus shifted from the Larmor frequency $\omega_0 = \gamma B_0$ with an amount proportional to the quadrupole coupling constant $e^2qQ/\hbar$. The satellite transitions are a sensitive probe for changes in the environment of the quadrupole nucleus. Whereas the central transition remains a narrow transition, the angular dependence of the satellite transitions cause a frequency distribution for a poly-crystalline sample, example figure 2.4 (b). The first order quadrupole interaction involves a rank two tensor which enables MAS to average the interaction, resulting in the spectrum shown in figure 2.4 (c). However, even for relatively small quadrupole interactions the MAS spinning frequency can not exceed the width of the static powder pattern. As a result spinning side bands occur separated by the spinning frequency.

If large quadrupolar interactions are present first order perturbation is not sufficient and the second order effects play a role. Depending on the maximum spectral width that can be probed, and the strength of the quadrupole interaction, the satellite transitions might not be observable. The central transition of a powder spectrum broadens due to second order quadrupole interactions with [37]:

$$\Delta\omega = \frac{1}{192\omega_0}\left(\frac{e^2qQ}{\hbar}\right)^2\left((3+\eta)^2 + 16(1+\eta)\right). \qquad (2.55)$$

The center of gravity of the powder resonance $m-1 \leftrightarrow m$ is shifted with respect to the isotropic ("true") chemical shift by an amount [37]:

$$\Delta\delta_{m-1,m} = \delta_{CS} - \delta_{iso} = -\left(\frac{3[I(I+1) - 9m(m-1) - 3]}{40[I(2I-1)]^2}\right)$$
$$\left(\frac{e^2qQ}{\omega_0}\right)^2\left(1 + \frac{\eta^2}{3}\right). \qquad (2.56)$$

The shape of the powder line depends on η. It is important to realize that for instance dipolar interactions and first order quadrupolar interactions do not depend on the Larmor frequency (field independent), ω_0, and the second order effects do (inversely proportional to the field). Field dependent measurements (Larmor frequency dependent) can therefore often reveal the origin of interactions. The effect of MAS on the central transition powder line shape is complicated if the quadrupole interactions are so strong that in that case they need to be treated in second order. In most cases the residual MAS line width is larger than the distance between the spinning side bands, hence they overlap. Moreover, the shape of the the central transition depends on the MAS speed [38].

Homogeneous and inhomogeneous resonance lines

There are two principle types of resonance lines in solids: homogeneously broadened and inhomogeneously broadened resonance lines. Homogeneous broadening is the result from transitions between two spin levels which are intrinsically broadened. Examples of interactions leading to homogeneous broadening are; dipolar interactions, fluctuating quadrupolar and chemical shift interactions. For homogeneously broadened lines the line

width is inversely related to the transversal or spin-spin relaxation time, T$_2$. In contrast to that, inhomogeneously broadened lines consist of a distribution of narrow homogeneously broadened resonance lines. Both field inhomogeneities and crystal imperfections lead to a inhomogeneous distribution of resonance frequencies. Experimentally, inhomogeneous broadening mechanisms can be removed by a spin echo pulse sequence (see section 2.2.6), and as a result the "true" line width can be obtained.

2.2.4 Classical description of the dynamics of a macroscopic spin system in a magnetic field

In the previous section the interactions were discussed in terms of individual spins. In section 2.2.2 it was clear that in an actual experiment the macroscopic magnetization needs to be considered. The r.f.-field-induced transitions cause the individual spins to reorient, and as a result the macroscopic magnetization will rotate. The Bloch equations offer a very useful tool in describing the dynamics of the macroscopic magnetization, including the transverse and longitudinal relaxation times, T_2 and T_1. Although the Bloch equations give useful insight into the macroscopic spin dynamics and the relaxation mechanism, it is unable to predict line-shapes resulting from the various interactions. For that, more sophisticated methods are needed such as the linear response theory developed by Kubo and Tomita [39].

The phenomenological equations of Bloch describe the time dependence of the macroscopic magnetization along the static field, the longitudinal component in the z-direction, and the transverse components in the x- and y-direction. The longitudinal and transverse relaxation are each assumed to be described by a single time constant, T_1 and T_2 respectively:

$$\frac{dM_z}{dt} = -(M_z - M_0)/T_1, \tag{2.57}$$

$$\frac{dM_x}{dt} = -iM_x/T_2, \tag{2.58}$$

$$\frac{dM_y}{dt} = -iM_y/T_2, \tag{2.59}$$

with M_0 the equilibrium magnetization along the z-axis at $t = 0$. In absence of relaxation, the motion of the nuclear magnetization for an ensemble of spins in a homogeneous field B_0 along the z-direction is governed by:

$$\frac{d\boldsymbol{M}}{dt} = \gamma \boldsymbol{B}_0 \times \boldsymbol{M}. \tag{2.60}$$

If the effect of relaxation can be superimposed on this motion we have:

$$\frac{d\boldsymbol{M}}{dt} = \gamma \boldsymbol{M} \times B_0\boldsymbol{k} - \frac{M_z - M_0}{T_1}\boldsymbol{k} - \frac{M_x\boldsymbol{i} + M_y\boldsymbol{j}}{T_2}, \tag{2.61}$$

where $\boldsymbol{i}, \boldsymbol{j}$ and $\boldsymbol{k}$ are the unit vectors in in x,y and z-direction (laboratory frame), respectively. Equation 2.61 can be solved by the following solution:

$$M_x = (M_{xy})_{t=0}e^{-\frac{t}{T_2}}cos(\omega_0 t + \phi_{t=0}), \tag{2.62}$$

$$M_y = (M_{xy})_{t=0}e^{-\frac{t}{T_2}}sin(\omega_0 t + \phi_{t=0}), \tag{2.63}$$

$$M_z = M_0 + (M_{z,t=0} - M_0)e^{-\frac{t}{T_1}}, \tag{2.64}$$

with $M_{xy} = \sqrt{M_x^2 + M_y^2}$ and ϕ is the phase of M_{xy} with respect to the y-axis at t=0. The Bloch equations provide us with a very clear classical picture of the macroscopic magnetization precessing around the static field $\boldsymbol{B}_0$. Measuring the transversal magnetization, for instance M_y, results in an exponentially decaying oscillating signal. In Fourier NMR this free induction decay (FID) is Fourier transformed to yield the absorption spectrum (see figure 2.3). For the exponentially decaying oscillating transverse magnetization this leads to a Lorentzian line-shape function for the absorption:

$$f(\omega) = \pi T_2 \left[\frac{1}{1 + (2\pi(\omega - \omega_0)T_2)^2} \right], \tag{2.65}$$

where ω_0 is the center of the resonance line and $1/\pi T_2$ the line width at half maximum.

In an actual NMR experiment the nuclear system is first perturbed before the relaxation is measured. In general, this is done using a pulse of a linearly polarized r.f. field along a direction perpendicular to the static field: $\boldsymbol{B}_1 = 2B_1 cos(\omega t)\boldsymbol{i}$. The effect of this perturbation can be illustrated by incorporating it in the Bloch equation. Assuming the pulse is much shorter than both T_1 and T_2 relaxation terms, we can neglect the last two terms in equation 2.61. Next we represent the Bloch equation in the coordinates of the rotating frame around B_0 with frequency ω. In the new system the magnetization and the r.f. field yield $\boldsymbol{M}' = \boldsymbol{i}'M_x' + \boldsymbol{j}'M_y' + \boldsymbol{k}M_z$ ($\boldsymbol{k}'$ coincides with $\boldsymbol{k}$) and $\boldsymbol{B}_1' = \boldsymbol{i}'2B_1$. This leads to the Bloch equation in the rotating frame:

$$\frac{\delta \boldsymbol{M}'}{\delta t} = \frac{d\boldsymbol{M}}{dt} - \omega \times \boldsymbol{M}' = \gamma \boldsymbol{M}' \times \left(B_0 + \frac{\omega}{\gamma} \right) \boldsymbol{k} + \gamma \boldsymbol{M}' \times \boldsymbol{B}_1'. \tag{2.66}$$

If we assume the linearly polarized r.f. field to be in exact resonance with precession of the nuclear magnetic moment in the laboratory frame, thus $\gamma B_0 = \omega$, the solution of equation 2.66 is simply:

$$M_x' = 0, \tag{2.67}$$
$$M_y' = M_0' sin(\gamma B_1 t), \tag{2.68}$$
$$M_z = M_0' cos(\gamma B_1 t). \tag{2.69}$$

To an observer in the rotating frame the nuclear magnetic moments rotate with a frequency $\omega_1 = \gamma B_1$ in the z-y' plane, starting at t=0 along the z-axis. The r.f. pulse length/amplitude can be chosen such that the macroscopic magnetic moment can have any direction in the z-y' plane. A $\pi/2$ pulse rotates the magnetization, in the rotating frame, along the x'-axis exactly in the plane perpendicular to the static field. This defines the initial condition for relaxation towards equilibrium described by the Bloch equations 2.62. The result is an exponentially damped oscillating x- and y- magnetization in the x- and y- direction, while the magnetization in z- direction recovers exponentially along the B_0 field. For any solution of the Bloch equations in the rotating frame, the solution in the laboratory frame (x,y,z frame) for the transversal magnetization, for instance the x-component, can expressed as:

$$M_x = M_x' cos(\omega t) + M_y' sin(\omega t). \tag{2.70}$$

To describe these phase relations under the influence of a perturbing r.f. pulse, Bloch introduced the complex susceptibility $\chi(\omega) = \chi'(\omega) + i\chi''(\omega)$. This susceptibility thus

governs the response in terms of the transversal magnetization due to the r.f. pulse with field strength B_1. Equation 2.70 in terms of the complex susceptibility results in:

$$M_x(t) = 2B_1\chi'(\omega)cos(\omega t) + i2B_1\chi''(\omega)sin(\omega t). \qquad (2.71)$$

This relation is in fact only valid for small r.f. excitations. The condition that B_1 is small is needed to prevent saturation, consequently χ' and χ'' are independent of B_1. Equation 2.71 can be interpreted as the linear response of the spin system to an r.f. excitation, where χ' represents the dispersion of and χ'' the absorption by the spin system of the r.f. field. Measurement of the response of the transversal magnetization is thus related to the complex susceptibility, the Fourier transform of which leads to the absorbed spectrum. The Bloch equations describe a simplified classical system only taking into account the Zeeman interaction. However, quantum mechanical treatment of an r.f. pulse as perturbation of a system including the various interactions has the same result for a pulse, which results in a rotation, θ, of the macroscopic magnetization [40]:

$$\chi'(\omega) = \frac{\gamma}{\sin(\theta)} \int_0^\infty \langle M_x(t) \rangle \cos(\omega t) dt. \qquad (2.72)$$

$$\chi''(\omega) = \frac{\gamma}{\sin(\theta)} \int_0^\infty \langle M_x(t) \rangle \sin(\omega t) dt. \qquad (2.73)$$

These equations are valid for relatively short pulses (relative to the line width) and a small perturbing r.f. field compared to the static field. From equations 2.72 and 2.73 it is clear that any pulse length, resulting in θ rotation of the macroscopic magnetization, results in the same response, although different in amplitude.

2.2.5   Relaxation due to diffusion

Fluctuations with frequencies in the order of the Larmor frequency can induce transitions between the nuclear spin states. This type of relaxation is referred to as spin-lattice or longitudinal relaxation and quantified in the T_1 time constant. In this context the lattice represents all aspects of the nuclear spin environment. As a result of the spin-lattice relaxation the spin system in a large static field perturbed by a $\pi/2$ pulse will reach equilibrium, the spins will re-align with the static field according to the equilibrium Boltzmann distribution over the spin levels. Fields that fluctuate with a frequency much smaller than the Larmor frequency do not cause transitions between the spin states as effectively, but broaden the instantaneous spread in energy levels, thereby broadening the NMR lines. This second relaxation mechanism is quantified in the spin-spin or transverse relaxation time, T_2. In solids, where the fluctuations are mostly in a smaller frequency range as compared to liquids, T_1 relaxation is often less efficient compared to T_2 relaxation ($T_1 >> T_2$). In that case the transversal magnetization reaches thermal equilibrium mainly by spin-spin interactions (mostly dipolar in character), before the complete spin system reaches thermal equilibrium with the lattice. A variety of interactions can cause relaxation in solids, the most important are the following. (1) The hyperfine coupling between the nuclear and electronic spins of conduction electrons has in addition to the Knight shift in the Larmor frequency also a dynamic character which can result in a simultaneous flip of both nuclear and electron spin in opposite direction.

(2) Paramagnetic moments, the large magnetic moments of unpaired electrons, usually cause fast relaxation leading to very small T_1 values. (3) Thermal vibrations cause time-dependent magnetic fields and electric field gradients that can induce transitions between the spin levels. (4) The diffusive motion of nuclei causes fluctuating magnetic fields.

In this paragraph more attention will be directed towards the relaxation due to diffusing nuclei, relating the relaxation rates to the timescale of the diffusion process.

Dipolar interactions between nuclear spins, often dominant in solids, result in a specific rigid lattice line width which, under certain assumptions, can be estimated by the method of moments, equations 2.48 and 2.49. However, in liquids, gasses and also in solids, diffusion of nuclear spins can lead to a line width much smaller than the rigid line width (the width if no diffusion takes place). A qualitative explanation for this is that, if the nuclear spin is allowed to randomly hop around with a specific time constant τ_c (the correlation time), it experiences an average of the dipolar interaction frequencies if τ_c is sufficiently short. Such an average value has a narrow frequency distribution compared to the distribution of instantaneous values, therefore, smaller line widths can be expected in case of diffusion of the nucleus or its environment, often referred to as motional narrowing. The time dependent Hamiltonian that describes the nuclear spin interactions with its environment can be expressed in different components:

$$\hat{H}(t) = \hat{H}_0 + \hat{H}_{Diff} + \hat{H}_1(t), \tag{2.74}$$

where $\hat{H}_1(t)$ is the perturbed Hamiltonian which can be, for instance, the dipolar or first order quadrupolar interaction responsible for broadening or splitting of the otherwise infinitely sharp resonance lines. $\hat{H}_{Diff}$ represents the kinetic energy of the diffusing nuclei that does not disturb the unperturbed Zeeman Hamiltonian $\hat{H}_0$. This means that just considering $\hat{H}_0$ and $\hat{H}_{Diff}$ will lead to infinitely sharp resonance lines. However, $\hat{H}_{Diff}$ does influence the way in which $\hat{H}_1(t)$ widens the resonance lines. We suppose that $\hat{H}_1(t)$ takes the form $\hat{H}_1 \cdot f(t)$ where $\hat{H}_1$ is independent of time and $f(t)$ is a fluctuating term measuring the strength of $\hat{H}_1$ at different times. Time dependent perturbation theory tells us that the transition probability between two energy levels a and b is given by:

$$W_{a \to b}(\omega) = \frac{1}{\hbar^2} \left| \left\langle b | \hat{H}_1 | a \right\rangle \right|^2 \int_{-\infty}^{+\infty} \langle f(0)f^*(0+t) \rangle \, e^{i\omega t} dt. \tag{2.75}$$

The quantity $G(t) = \langle f(0)f^*(0+t) \rangle$ is the autocorrelation function of $f(t)$. The autocorrelation function is the inverse Fourier transform of the power spectrum $J(\omega)$ which describes the random fluctuations that cause the transitions:

$$J(\omega) = \int_{-\infty}^{+\infty} G(t)e^{i\omega t} dt. \tag{2.76}$$

Generally $G(t)$ decreases rapidly with t, and it is particular simplifying to assume a correlation function that decays exponentially:

$$G(t) = \langle f(0)f^*(0) \rangle \, e^{-|t|/\tau_c}, \tag{2.77}$$

where τ_c is a characteristic time of the random motion. In that case the power spectrum can be expressed as:

$$J(\omega) = \frac{2\tau_c}{1 + \omega^2 \tau_c^2} \langle f(0)f^*(0) \rangle, \tag{2.78}$$

where $\langle f(0)f^*(0)\rangle$ is the mean square average of the fluctuation, a measure of the fluctuation strength.

To proceed, we need to know the interaction Hamiltonian, $\hat{H}_1$ in equation 2.75. For both dipolar and quadrupolar interactions the spin interactions can either be expressed in cartesian tensors, 3×3 matrices in equations 2.47 and 2.51, or alternatively in spherical tensors in terms of Euler angles. For the dipole interaction between two spins I and S the latter leads to the dipolar alphabet [36]:

$$\widehat{H}_D = \frac{\mu_0}{4\pi}\hbar^2\gamma_I\gamma_S[A + B + C + D + E + F], \tag{2.79}$$

where:

$$
\begin{aligned}
A &= (1 - 3\cos^2\theta(t))r^{-3}(t)I_zS_z, \\
B &= -\tfrac{1}{4}(1 - 3\cos^2\theta(t))r^{-3}(t)(I_+S_- + I_-S_+), \\
C &= -\tfrac{3}{2}\sin\theta(t)\cos\theta(t)\exp^{-i\varphi(t)}r^{-3}(t)(I_zS_+ + I_+S_z), \\
D &= -\tfrac{3}{2}\sin\theta(t)\cos\theta(t)\exp^{i\varphi(t)}r^{-3}(t)(I_zS_- + I_-S_z), \\
E &= -\tfrac{3}{4}\sin^2\theta(t)\exp^{-2i\varphi(t)}r^{-3}(t)I_+S_+, \\
F &= -\tfrac{3}{4}\sin^2\theta(t)\exp^{-2i\varphi(t)}r^{-3}(t)I_-S_-,
\end{aligned}
\tag{2.80}
$$

where θ and ϕ are the polar and azimuthal angles and r the distance between the two spins, which, all three, are allowed to fluctuate with time due to the diffusional process. The quadrupolar Hamiltonian can be considered a degenerate case of the dipole Hamiltonian with $S = I$, hence leading to basically the same terms. A and B leave the sum of the two quantum numbers $m = (m_I + m_S)$ unchanged: $\Delta m = 0$, whereas C, D induce transitions with $\Delta m = \pm 1$ and C, D induce transitions with $\Delta m = \pm 2$. The term A represents the change of the z component of the magnetic field by the z component of neighboring magnetic moments. As a consequence, the local field varies from nucleus to nucleus giving rise to a distribution in Larmor frequencies which contributes to the static line width (in absence of fluctuations). The shape of the distribution can be calculated given the exact configuration of the spins. If one is not interested in the exact shape but rather in certain characteristics, such as the line width of the distribution, the method of moments of Van Vleck offers an alternative (equations 2.48 and 2.49). B alters both nuclear spins but does not change the sum of the two quantum numbers $m = (m_I + m_S)$ which corresponds to simultaneous flopping of two antiparallel spins in the case of $I = 1/2$. The precession of one spin causes a fluctuating field at the resonance frequency at the location of the other, which results in simultaneous transitions. These transitions limit the lifetime of the spins in a given state and hence broaden the spectral line. This is taken into account by a numerical factor which is also included in Van Vleck's second moment (equations 2.48 and 2.49). The terms C to F are relatively small contributions, therefore only A and B need be considered for the rigid lattice line width. In an actual pulse NMR experiment were the magnetization is rotated into the plane perpendicular to the static magnetic field it is the static distribution in Larmor frequencies that limits the phase memory of the precessing nuclear spins. This is quantified in the transversal or spin-spin relaxation time, T_2, which for homogeneously broadened lines is directly related to the line width depending on the line shape (expressed in Hz: $1/\pi T_2$ FWHM for a Lorentzian and the width between points of maximum slope for a Gaussian).

Interaction terms A and B do not account for the relaxation of the spin system as a whole towards thermal equilibrium with the environment. The thermal contact of the spin system is provided by the terms C to F that allow effective transitions of the nuclear spins, hence energy transfer to and from the environment. In this case we consider the energy exchange with random diffusion of atoms, and hence we allow the position coordinates in equation 2.79 to vary randomly with time. If the terms C to F are different from zero, they cause transitions, $\Delta m = \pm 1, \pm 2$, where the random motion provides or absorbs the corresponding energy. This provides the relaxation mechanism of a perturbed system of spins to thermal equilibrium which under certain circumstances can be quantified by one relaxation time, T_1, which is related to the transition probabilities. The equilibrium populations of two spin levels, N_a and N_b and the transition probabilities, $W_{a \to b}$ and $W_{b \to a}$, are related by Boltzmann's law and by detailed balance:

$$\frac{W_{a \to b}}{W_{b \to a}} = \frac{N_b}{N_a} = e^{(E_a - E_b)/kT}, \tag{2.81}$$

where $(E_a - E_b)$ is the difference in energy of levels a and b and T the temperature of the lattice. If, even when the spins are not equilibrium with the lattice (the environment), the probabilities $W_{a \to b}$ and $W_{b \to a}$ are related by a Boltzmann factor, as in equation 2.81, the equilibrium is reached by a simple exponential law with characteristic time [41]:

$$T_1 = \frac{1}{2W}. \tag{2.82}$$

In the case of $I = 1/2$, there will always be a temperature T_s, the spin temperature, defined by $e^{\gamma \hbar B_0 / kT_s} = N_- / N_+$, where N_- and N_+ are the instantaneous occupancies when the spin system is not in equilibrium with its environment. In this case one might say that the spin system itself is in equilibrium, specified by T_s, and it approaches equilibrium with the lattice as a whole, and the foregoing definition of T_1 is valid. However, if $I > 1/2$ a spin temperature can not be defined unless the populations of successive levels are related by the same factor. The most prominent interaction that is capable to restore the internal equilibrium between the spins, such that a spin temperature can be defined, is the spin-spin interaction associated with term B in equation 2.80. The simultaneous flopping of two spins such that their total quantum number does not change tends to bring the spin system to an internal equilibrium. Therefore, if this process is fast compared to the spin-lattice relaxation, $T_1 >> T_2$, equation 2.82 also applies for $I > 1/2$ and the relaxation is relatively simple.

For liquid-like random diffusional motion of nuclei with $I = 1/2$ and $I > 1/2$ (given the above restriction), Bloembergen Purcell and Pound [41] derived:

$$\frac{1}{T_1} = \frac{2}{5} \gamma^4 \hbar^2 N I(I+1) \int_a^{+\infty} \frac{1}{r^6} \left[\frac{\tau_c}{1 + \omega_0^2 \tau_c^2} + \frac{2\tau_c}{1 + 4\omega_0^2 \tau_c^2} \right] 4\pi r^2 dr, \tag{2.83}$$

$$\frac{1}{T_2'} = \frac{3}{2} \gamma^2 \hbar \left\{ \frac{4 N I(I+1)}{15} \int_{-2/T_2'}^{2/T_2'} \int_a^{+\infty} \frac{1}{r^6} \left[\frac{\tau_c}{1 + \omega^2 \tau_c^2} \right] 4\pi r^2 dr d\omega \right\}^{\frac{1}{2}}, \tag{2.84}$$

where N is the number of nuclei per unit volume and the r-integration assumes a homogeneous distribution of nuclear dipoles starting from the minimum nuclear distance
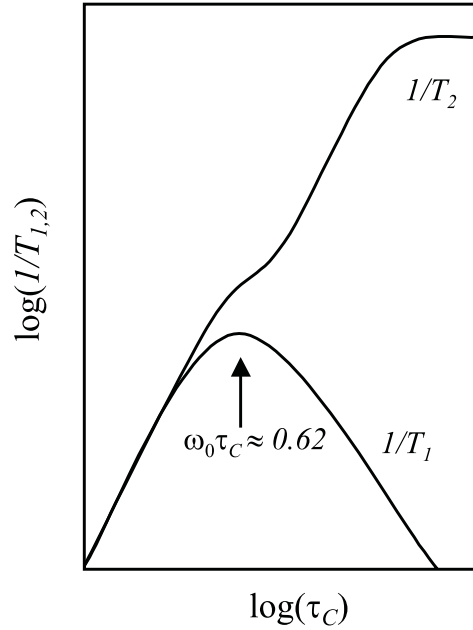
Figure 2.5: *The BPP model for the relaxation rates $1/T_1$ and $1/T_2$, taking only nearest neighbors into account, as a function of the correlation time, τ_c, which is associated with randomly diffusing atoms. For random diffusion in liquids and hopping diffusion in a crystal lattice τ_c is inversely proportional to the diffusion coefficient.*

a. The limited frequency range in the expression for $1/T_2'$ restricts the frequencies to that corresponding to the actual splitting of the energy level. Since these results were first derived by Bloembergen, Purcell and Pound [41] it is often referred to as the BPP model. The line width is not only determined by T_2' because the spin lattice relaxation limits the the lifetime of the nuclear states. This effect can be included such that the true spin-spin relaxation time yields [41]:

$$\frac{1}{T_2} = \frac{1}{T_2'} + \frac{1}{2T_1}. \tag{2.85}$$

If only the effect of the first neighbors (at distance a) is incorporated in equation 2.83, the result is:

$$\frac{1}{T_1} = \frac{2\gamma^4 \hbar^2 I(I+1)}{5a^6} \left[\frac{\tau_c}{1 + \omega_0^2 \tau_c^2} + \frac{2\tau_c}{1 + 4\omega_0^2 \tau_c^2} \right], \tag{2.86}$$

$$\left(\frac{1}{T_2'} \right)^2 = \frac{6\gamma^4 \hbar^2 I(I+1)}{5a^6} \arctan\left(\frac{2\tau_c}{T_2'} \right). \tag{2.87}$$

The behavior of the BPP model, only including the first neighbor interactions, for the relaxation rates as a function of the correlation time is schematically shown in figure 2.5.

The longitudinal relaxation rate $1/T_1$ reaches a maximum near $\omega_0^2 \tau_c^2 \approx 1$. The reason for this maximum is that the energy exchange of the spin system with the diffusing atoms is most efficient if the characteristic time of the diffusion, τ_c, corresponds to the Larmor precession time $1/\omega_0$.

Although the equations in 2.83 were derived for the liquid like diffusion, it has shown to also work quite well for atomic diffusion in solids [42]. Given the relation between the correlation time and the diffusion coefficient, the relaxation rates can directly be related to microscopic self diffusion coefficients. The fluctuations associated with the diffusion process are characterized by auto-correlation functions (see equation 2.75), hence the diffusion process probed is self-diffusion. Assuming random translational jump diffusion of atoms in a lattice or in a liquid, the correlation time can be expressed in terms of a microscopic diffusion coefficient D:

$$\tau_c = a^2/KD, \tag{2.88}$$

where a is the hopping distance (and nearest neighbor distance) and K the number of possible jump directions (=12 for a liquid). In many cases this type of diffusion is thermally activated, obeying:

$$D = D_0 e^{-E_A/kT}, \tag{2.89}$$

where E_A is the activation energy for diffusion. Combining equation 2.86 or equation 2.87 with equation 2.88 leads to a direct relation of the relaxation rates with the diffusion coefficient.

The relations become very simple in the limit of large and small values of the correlation time relative to the Larmor frequency. At high temperatures, such that $\omega_0^2 \tau_c^2 << 1$, T_1 in equation 2.86 leads to:

$$\frac{1}{T_1} = \frac{6\gamma^4\hbar^2 I(I+1)}{5KDa^4}. \tag{2.90}$$

In this domain T_1 is inversely proportional to the diffusion coefficient, and temperature dependent T_1 data can be used to determine the activation energy for diffusion, E_A. For lower temperatures, such that $\omega_0^2 \tau_c^2 >> 1$, one finds:

$$\frac{1}{T_1} = \frac{3\gamma^4\hbar^2 I(I+1)KD}{5\omega_0^2 a^8}. \tag{2.91}$$

In contrast to the result in equation 2.90, here T_1 is proportional to D.

For high temperatures, such that $2\tau_c/T_2' << 1$ the spin-spin relaxation rate in equation 2.87 becomes:

$$\frac{1}{T_2'} = \frac{12\gamma^4\hbar^2 I(I+1)}{5KDa^6}. \tag{2.92}$$

Like the behavior of $1/T_1$ at higher temperatures ($\omega_0^2 \tau_c^2 << 1$), $1/T_2'$ in equation 2.92 is inversely proportional to the diffusion coefficient. Hence, given the influence for $\omega_0^2 \tau_c^2 << 1$ of T_1 on the observed T_2 via equation 2.85 (see also figure 2.5), T_2 only differs a numerical factor compared to T_2' in equation 2.92. For $\omega_0^2 \tau_c^2 >> 1$ the influence of T_1 is negligible and equation 2.92 can be used. The expression for $1/T_2'$ holds only for $< \Delta\omega^2 >^{1/2} \tau_c << 1$, where $< \Delta\omega^2 >$ is the second moment of the static resonance line shape. In this regime smaller correlation times (higher temperatures) lead to a more narrowly defined distribution of the average interactions of the nuclear spin with its environment which increases the transversal relaxation time. For homogenous lines this effect can be observed as line narrowing with decreasing correlation time (or increasing temperature) because $1/T_2$ is directly proportional to the line width for homogeneously

broadened lines. For $< \Delta\omega^2 >^{1/2} \tau_c >> 1/T_2'$ the fluctuation frequency is to small too influence the line shape, hence $1/T_2'$ is proportional to the static line width. The transition between both regimes is approximately located at $\tau_c = T"_2/\sqrt{2}$, with $T"_2$ the spin spin relaxation time associated with the static line width. This can be used to determine the diffusion coefficient from T_2' via equation 2.88.

Torrey [43] has extended the BPP theory for T_1 in order to predict the relaxation more precise for specific cases of random translational lattice diffusion. Particularly in the vicinity of the maximum in $1/T_1$, their model predict the behavior better. For the higher temperatures, $\omega_0^2\tau_c^2 << 1$, Torrey's model for T_1 becomes equivalent with the BPP model. For T_2 the improvement of Torrey's model is limited to the region $\omega_0^2\tau_c^2 \approx 1$, because for $\omega_0^2\tau_c^2 << 1$ the T_1 effects on T_2 are small and although large for $\omega_0^2\tau_c^2 >> 1$ this is just the region where the two models become equivalent.

The relaxation rates for quadrupolar interaction can be derived very similarly to that for dipolar interactions. The geometrical terms in equation 2.80 are the same and, under the assumption of the existence of a well defined spin temperature, the same relations can be used to determine the relaxation rates. The obvious differences are the constants that specify the interaction strength which, in the case of quadrupole interaction, will be related to the quadrupolar coupling constant. One needs to replace the $\gamma^4\hbar^2/r^6$ dipolar term by $e^4q^2Q^2/(4\hbar^2)$ in equations 2.83.

2.2.6 Experimental methods in NMR

In sections 2.2.2 and 2.2.4 Fourier NMR was introduced which uses the fact that in one short pulse a large frequency window can be probed to excite the spin system. Fourier NMR gives the opportunity to manipulate the spin system by sequences of pulses in order to reach certain preferred conditions. In this paragraph a few basic examples are shown that are relevant for the NMR experiments in this thesis.

Spin echo

Suppose we apply a $\pi/2$ pulse to an ensemble of spins in a solid. Subsequently, all spins start to rotate in the x-y plane (B_0 along the z-axis) with the same phase. From the Bloch equations 2.61 we learn that free induction decay decreases exponentially, with T_2 expressing the de-phasing of the nuclear spin precessions with respect to each other. If a second pulse, a π pulse (see figure 2.6 (a)), is applied after a certain time τ the spins that were a certain phase angle ahead of the average, are now faced with the same phase angle difference only now behind the average. Precisely τ later their phase is back to the average again, just like after the first pulse. In other words, the spins have refocussed. An advantage of detecting the free induction decay with a spin-echo compared to a simple $\pi/2$ pulse is that clean data can be acquired at $t_2 = 0$ whereas directly after a pulse there will always be signal left in the coil for some time (usually in the order of microseconds) which restricts the resonance width that can be measured. By measuring the resonance intensity for various τ_{echo} the "true" transversal relaxation time T_2 can be determined irrespective of inhomogeneous line broadening due to for instance applied field inhomogeneities and crystal imperfections.
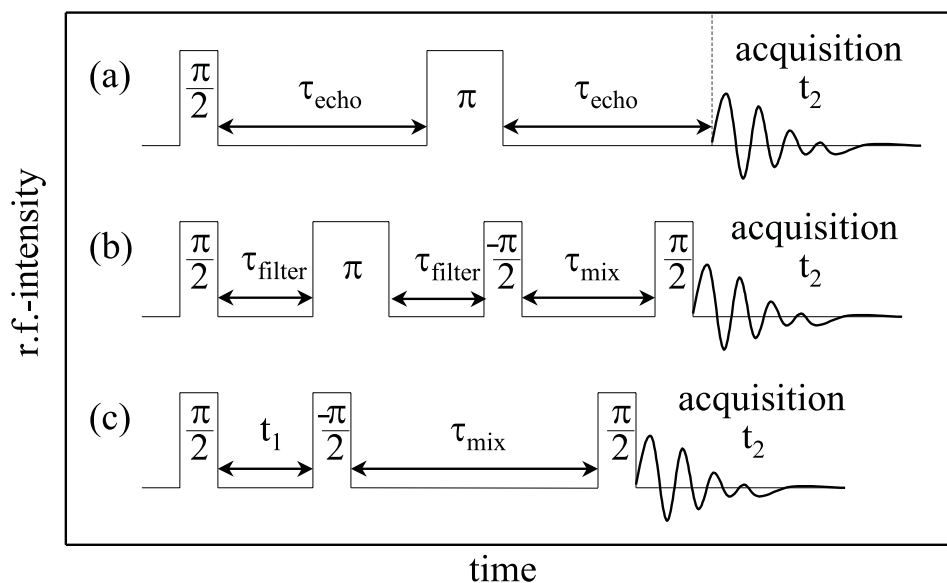
Figure 2.6: *NMR Pulse sequence's. (a) Echo pulse sequence. (b) T_2 filter plus diffusion time pulse sequence. (c) 2D-NMR pulse sequence.*

T_2 filter and spin diffusion

If two resonances are present with different T_2, for instance due to different environments of the NMR nucleus, say species A and B, the one with the longer T_2, say T_2^A can be isolated. This can be done by applying an echo sequence (see figure 2.6 (b)) with time τ_{filter} long enough to loose the coherence of species B, $\tau_{filter} > T_2^B$. The refocussed intensity at time τ_{filter} is solely due to species A which is aligned along the -z-axis by a $-\frac{\pi}{2}$ pulse. This selected magnetization is kept along the z-axis during the time τ_{mix} before it is placed back in the xy-plane by a $\frac{\pi}{2}$ pulse. Then the signal is detected by the coil. As a function of τ_{filter} magnetization along the z-axis of the nuclei in A can be lost by T_1 relaxation but also by nuclei changing from one environment to another i.e. nuclei moving from A to B. In this way the mobility of nuclear motions can be quantified, however only if the T_2 times of the different species allow the T_2 filtering and mixing times are shorter than the longitudinal relaxation.

Two dimensional NMR

The first $\frac{\pi}{2}$ pulse places the magnetization in the xy-plane where it will precess around the static field with the Larmor frequency. After a time t_1 a $-\frac{\pi}{2}$ pulse is applied. Because the pulse is applied such that the magnetization rotates in the yz-plane only the component projected on that plane is recovered along the z-axis. As a function of t_1 the z-component of the magnetization sinusoidally varies with the Larmor frequency. After a mixing time τ_{mix} the third pulse rotates this z-component back in the xy-plane. Directly after this pulse the FID is recorded. A two dimensional data set is formed if FID's are recorded for different times t_1. Because both the spin precession during t_1 and t_2 proceeds with the Larmor frequency, two dimensional Fourier transform will lead to a 2D spectrum with

the resonances on the diagonal ($\omega_1 = \omega_2$). However if for instance two resonances are present, A and B, and during the mixing time τ_{mix} nuclei will change their environment from A to B the resonance will occur in the ω_1 dimension at the A frequency, but in the ω_1 dimension at the B frequency leading to off-diagonal intensity in the $\omega_1\omega_2$ plot. Thus 2D-NMR enables to detect changes in the environment of the resonance nucleus between the spectrum before the mixing time (t_1-dimension) and after the mixing time (t_2-dimension). In this way nuclear mobility can results in off-diagonal intensity. 2D-NMR is a powerful tool in observing atomic and molecular dynamics on time scales typically ranging from T_2 to T_1.

2.3   X-ray absorption spectroscopy

2.3.1   Introduction

When X-rays pass through a material their absorption depends on their energy. The Lambert-Beer law relates the incoming intensity I_0 with the outgoing I_1 via the linear absorption coefficient $\mu(E)$:

$$I_1 = I_0 e^{-\mu(E)d}, \tag{2.93}$$

where d is the thickness of the absorbing material. In order to measure the linear absorption coefficient $\mu(E)$, the incoming and transmitted intensities need to be measured as a function of energy. The schematic experimental setup for a X-ray absorption spectroscopy (XAS) experiment is shown in figure 2.7. Generally, the X-ray photon source
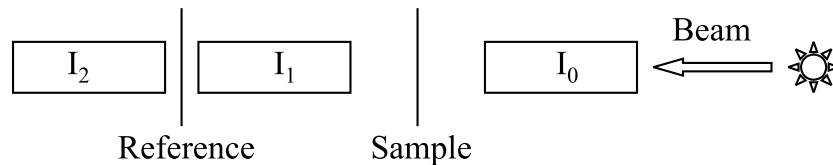
Figure 2.7: *Schematic setup for an X-ray absorption experiment. The boxes represent ionization chambers. In principle $\mu(E)$ can be determined by measuring the intensity in chamber zero and one, equation 2.93. Between the second and the third ionization chamber a reference foil is placed in order to calibrate the exact edge position of the sample.*

is a bending magnet at a synchrotron storage ring, which can provide a range of X-rays typically 6 to 20 keV wide, depending on the specific beam line. The silicon double crystal monochromator selects a narrow band of 1 to a few eV from the "white" beam. The intensities in front and behind the sample are measured with ionization chambers, and the third ionization chamber behind a reference foil provides each measurement with a reference energy scale. Generally, XAS deals with photo absorption by core electrons. Photo absorption is a one photon process where an electron is excited to an unoccupied state. By increasing the photon energy new core levels can be excited, thereby increasing the absorption coefficient recognized as the edges, see figure 2.8.

Figure 2.8: *Ti K,L,M edges of a Ti metal foil. (a) The fine structure of the Ti K edge and (b) the extracted oscillatory part of the Ti K edge which contains structural information.*
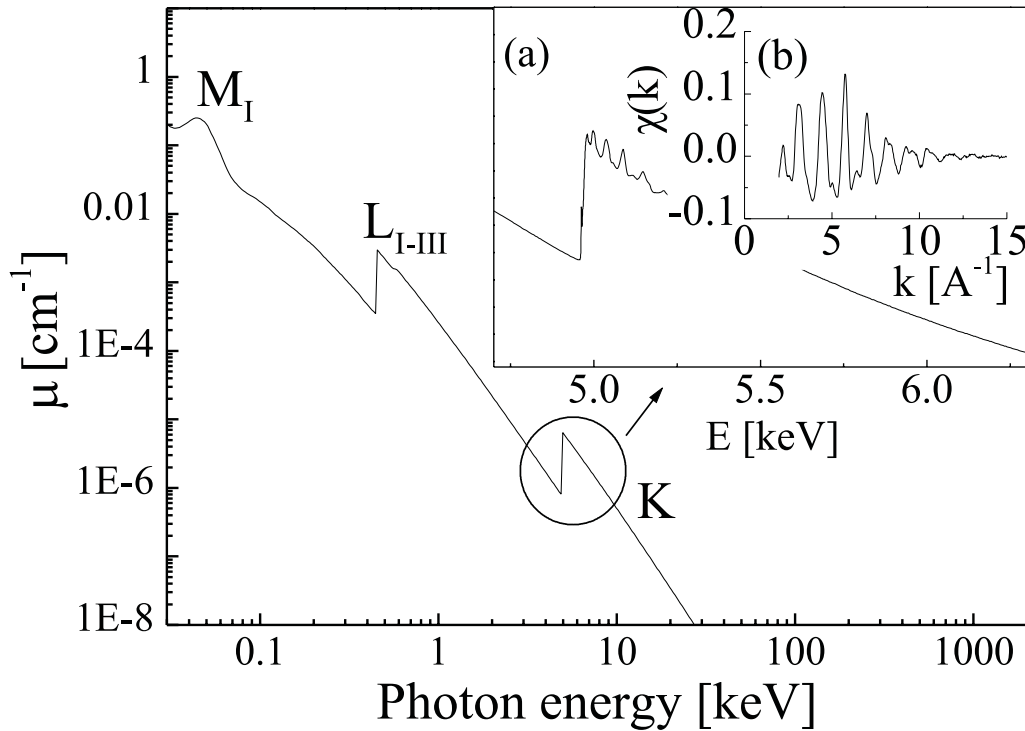
At the K-edge *1s*-electrons are excited and at L_1-, L_2- and L_3-edges *2s*, *$2p_{1/2}$* and *$2p_{3/2}$* electrons are excited. For an isolated atom the absorption edges would be sharp and smooth. However, for condensed matter an additional fine structure appears around and above the edges that is the result of the photo electron which is excited to unoccupied states, either localized or delocalized. Two regions in the X-ray absorption spectrum can be distinguished. First, the X-ray absorption near edge structure (XANES) near the edge up to roughly 40 eV above the edge, and secondly the extended X-ray absorption fine structure (EXAFS) further above the edge. The difference between these regions stems from the strength of the photo-electron scattering. The XANES region is dominated by strong multiple scattering because the mean free path is large. Analysis of these XANES oscillations in the spectrum of a particular sample can provide information about vacant orbitals, electronic configuration and the site symmetry of the absorbing atom. In addition, the absolute position of the edge is related to the oxidation state of the absorbing atom, because the shielding of the core electrons will depend on the occupation of the other electronic levels. At higher energies the modulations become weaker and single scattering effects dominate. The expelled photo electron wave interferes constructively and destructively with its back scattered intensity from surrounding atoms. Hence, the observed fringes contain structural information, like inter-atom distances and coordination numbers. In addition, the XANES probes the electronic structure, and hence, X-ray absorption spectroscopy is capable to probe both structural order and electronic properties. Comprehensive texts concerning XANES and EXAFS can be found in [44].

2.3.2   XANES

The interaction of X-rays and matter can be described by Fermi's golden rule which gives the transition probability between the initial state $|\psi_i\rangle$ and final state $\langle\psi_f|$ in the dipole approximation :

$$W_{i \to f} = |\langle\psi_f|\widehat{H}_{Int}|\psi_i\rangle|^2 \delta(E_f - E_i + \hbar\omega)\rho_f(E_f). \tag{2.94}$$

The delta function takes care of the energy conservation and the squared matrix element gives the transition rate. $\widehat{H}_{Int}$ represents the interaction of the photon with the electron treated as perturbation of the total Hamiltonian. $\rho_f(E_f)$ represents the density of the available final states. For one-photon transitions the dipole approximation (first order terms of $\widehat{H}_{Int}$) suffices and only contains the electric field acting on the electron angular moments. In the XANES region electron transitions occur towards unoccupied states inside the excited atom while in the EXAFS region the energy of the electron is high enough to ionize the atom. Therefore, the XANES region can be related to the partial density of states of the absorbing atom, partial since the absorption process needs to obey the transition rules. For instance in case of K-edge absorption the *1s* electron can only be excited to a state with *p*-character since $\Delta I = 1$ for photon absorption when only the dipole approximation is considered. Multipole excitations disturb this simple picture, however, they are often very weak in intensity. In addition hybridized atomic bands might also facilitate initially forbidden transitions. Although these aspects can involve complicated transitions in the electronic structure, most difficulties in XANES arise due to the multiple scattering events on the structure. Due to the complications brought by multiple scattering effects, the XANES theory is complex, and not yet fully understood. Analysis is therefore often done in comparison with similar materials for which ideas have been developed concerning the XANES features. Nevertheless, theoretical models have been developed in the last decade that are now able to simulate XANES spectra *ab-initio* including self-consistent real-space multiple scattering theory (for instance the FEFFv8.10 code [45]). In many cases this allows a quantitative interpretation of XANES data on the basis of an *ab-initio* calculation of the absorption spectrum.

2.3.3   EXAFS

For the EXAFS region theoretical models exist that enable the interpretation of experimental results. In the EXAFS region the density of the final state is that of a free electron and a scattered contribution. The fine structure of the edge can be normalized to the edge shape by defining $\chi(E)$ as:

$$\chi(E) = \frac{\mu(E) - \mu_0(E)}{\mu_0(E)}, \tag{2.95}$$

were $\mu_0(E)$ is the actual edge shape (the atomic background absorption) without the fine structure. The result for χ based on Fermi's Golden rule equation 2.94 can be derived to be [44]:

$$\chi(\boldsymbol{k}) = \sum_i A_i(\boldsymbol{k})sin(2\boldsymbol{k}r_i + \theta_i(\boldsymbol{k})), \tag{2.96}$$

where the amplitude, $A_i(\boldsymbol{k})$, of the oscillations is given by:

$$A_i(\boldsymbol{k}) = \frac{N_i F_i(\boldsymbol{k}) D_i(\boldsymbol{k}) e^{-2\sigma_i^2 \boldsymbol{k}^2}}{\boldsymbol{k} r_i^2}, \tag{2.97}$$

and $\mathbf{k}$ the photoelectron wave vector:

$$|\boldsymbol{k}| = \sqrt{2m/\hbar(E - E_0)}, \tag{2.98}$$

where E_0 is absorption edge position and m the electron mass. The structural information provided by EXAFS around the central atom can be deduced from equation 2.96 because the summation runs over the different coordination shells surrounding the atom. The amplitude is proportional to the coordination number N_i at distance r_i with scattering amplitude $F_i(\boldsymbol{k})$. Because $F_i(\boldsymbol{k})$ is an element specific property, different backscattering atoms can be separated. The interference effect is recognized in the sine term from which in principle the atom distances can be determined. The photo-electron wave suffers additional phase shifts $\theta_i(\boldsymbol{k})$ when travelling through the potentials of the absorber and the scattering atoms. A Gaussian distribution of the atoms in coordination shell i with standard deviation, σ_i, around the average distance, r_i, will lead to a damping of the EXAFS amplitude. This results in the Debye-Waller factor for the instantaneous position distributions due to thermal motions. The additional damping factor, $D_i(\boldsymbol{k})$, incorporates the effect of inelastic scattering which results in a reduction of the photo-electron coherence length. Assuming that $F_i(\boldsymbol{k})$ and $\theta_i(\boldsymbol{k})$ and $D_i(\boldsymbol{k})$ are known, EXAFS provides us with r_j, N_j and σ_i. The relations $F_i(\boldsymbol{k})$, $\theta_i(\boldsymbol{k})$ and $D_i(\boldsymbol{k})$ can be determined by calculations based on the composition and structure. Often these values are also determined from well known related compounds and the values can be used in the interpretation of the material of interest. Compared to the XANES region, the EXAFS region is much easier to calculate due to the absence of strong multiple scattering. In many cases models can be tested by fitting them to the data, a suitable package is WinXas [46]. EXAFS probes the local atomic order around the specific absorbing atom. The limited value of the mean free path of the photoelectron implicates that the EXAFS signal contains information only on the closest neighbors. For this reason EXAFS is particular useful in the structural determination of non-crystalline materials.

Chapter 3

Two-phase morphology and lithium interstitial diffusion in TiO$_2$ (anatase); a ^{7}Li MAS NMR study

Abstract

^{7}Li magic angle spinning solid state nuclear magnetic resonance is applied to investigate the lithium local environment and lithium ion mobility in tetragonal anatase TiO$_2$ and orthorhombic lithium titanate Li$_{0.6}$TiO$_2$. Upon lithium insertion an increasing fraction of the material changes its crystallographic structure from anatase TiO$_2$ to lithium titanate Li$_{0.6}$TiO$_2$. Phase separation occurs and as a result the Li-rich lithium titanate phase coexists with the Li-poor TiO$_2$ phase containing only small Li amounts ≈ 0.01. In both the anatase and the lithium titanate lattice Li is found to be hopping over the available sites with activation energies of 0.2 eV and 0.09 eV respectively. This leads to rapid microscopic diffusion rates at room temperature ($D_{micr} = 4.7 \times 10^{-12}$ cm^{2}s^{-1} in anatase and $D_{micr} = 1.3 \times 10^{-11}$ cm^{2}s^{-1} in lithium titanate). However, macroscopic intercalation data show activation energies of ~ 0.5 eV and smaller diffusion coefficients. We suggest that the diffusion through the phase boundary is determining the activation energy of the overall diffusion and the overall diffusion rate itself. The chemical shift of lithium in anatase is independent of temperature up to $\sim$250 K, but decreases at higher temperatures, reflecting a change in the *3d* conduction electron densities. The Li mobility becomes prominent from this same temperature showing that such electronic effects possibly facilitate the mobility.

3.1 Introduction

TiO$_2$ (anatase) has been subject of a large number of studies during the last decade. This interest arises from the possible application of TiO$_2$ in solar cells [15, 47, 1] ,electrochromic devices [48, 49, 50, 51] and rechargeable lithium ion batteries [52, 2, 53, 54].

The use of TiO$_2$ (anatase) as an electrode material in lithium ion batteries and electrochromic devices is based on its ability to accommodate charge in the form of small foreign ions, such as Li$^+$ and H$^+$ in an intercalation process.

Schematically, the electrochemical reaction can be written as: TiO$_2$ + xLi$^+$ + xe$^-$ → Li$_x$TiO$_2$, where x is the mole fraction Li in TiO$_2$. The maximum Li insertion in TiO$_2$ (anatase) varies through the literature from x= 0.5 up to 1 depending on the temperature and experimental technique [52, 53, 54, 4, 6, 55, 56, 57]. For chemical intercalation with n-butyllithium [56], which has a potential of 1 V vs. Li, x= 0.7 seems to be the most reliable value, while for electrochemical experiments x = 0.5 is most consistently reported for the maximum insertion ratio. The (elastic) interaction force between intercalated Li-ions is attractive [57] and weak Ti-Ti interactions are formed [21], which results in phase separation. The repulsive Coulomb interaction between the lithium ions is expected to be responsible for the limitation of the lithium content to x = 0.7 [4, 57]. TiO$_2$ (anatase) has a tetragonal phase (space group I41/amd, number 141). Cava *et al.*[4] determined the structure of the intercalation compound Li$_{0.5}$TiO$_2$ (lithium titanate) with neutron diffraction (space group Imma, number 74). The overall orthorhombic distortion of the atomic positions in the change from anatase to lithium titanate is small and leads to more regularly shaped TiO$_6$ octahedra in lithium titanate than in anatase. The change in symmetry is accompanied by a decrease of the unit cell along the c-axis and an increase along the b-axis, resulting in an increase of ∼4 % of the unit cell volume. In the lithium titanate phase the Li ions are randomly located in half of the available interstitial octahedral 4e sites, which was also found in theoretical calculations [18, 19]. Van de Krol *et al.* [58] have studied the structural changes during intercalation with *in-situ* X-ray diffraction (XRD). They reported that the phase transition accompanying the intercalation process is reversible, and starts at insertion ratios larger than x = 0.05 for nano-structured TiO$_2$ (anatase) electrodes [5]. Electrochemically, the two phase system produced by the phase separation and transition results in a constant potential during insertion and extraction of Li for 0.05 < x < 0.5. The lithium ion diffusion in lithium titanate and in anatase is likely to occur along a diffusion path connecting the vacant octahedral (interstitial) sites [19]. The macroscopic diffusion coefficient obtained with chronoamperometry on CVD films was found to be 2 × 10^{-15} cm^{2}s^{-1} for insertion and 6 × 10^{-15}cm^{2}s^{-1} for extraction [5]. This is significantly smaller than those obtained for single crystalline anatase; 2 × 10^{-13} cm^{2}s^{-1} for insertion and 6 × 10^{-13}cm^{2}s^{-1} for extraction [6]. Activation energies for insertion and extraction were found to be 0.54 eV and 0.78 eV respectively [5], and 0.6 eV for diffusion [18]. These values are in good agreement with the calculated 0.5 eV activation energy for Li hopping from one interstitial site to another [19, 9]. Van de Krol *et al.* [7] suggested that the difference found between the rate of insertion and the rate of extraction may be due to a large difference between the Li$^+$ mobility in the coexisting phases TiO$_2$ (anatase) and Li$_{0.5}$TiO$_2$ (lithium titanate). Little is known concerning the microscopic lithium ion mobility in both phases. Therefore, the present investigation was initiated to study the lithium environment and mobility in Li-doped TiO$_2$ with an overall composition given by Li$_x$TiO$_2$, where x varies between 0.03 and 0.7. ^{7}Li solid-state MAS NMR is applied since it can locally probe the chemical environment of Li via the chemical shift (resonance line positions) and quadrupolar interaction. The Li dynamics can be probed when Li hops from one site to another on a frequency comparable to, or shorter than, the relevant

NMR spectral parameters expressed in frequency units [37]. Two main questions will be addressed: i) in which crystallographic phase and with what concentration is the Li intercalated, and ii) on what time scale and with what activation energy does the Li motion occur in each phase. Furthermore, the chemical shift may give information concerning the electronic local environment of Li. We mainly concentrate on the small insertion ratios where the ^{7}Li NMR signal is visible for both the coexisting phases, anatase and lithium titanate. In contrast, at higher insertion ratios, $x > 0.2$, only the signal of lithium in lithium titanate is resolvable [55]. X-ray diffraction was employed to determine the relative amounts of anatase and lithium titanate, as well as to determine the domain size of each phase.

3.2   Materials and methods

3.2.1   Sample preparation

Microcrystalline TiO_2(anatase) (99%) was obtained from Janssen Chemica. X-ray diffraction showed the characteristic anatase structure. Li_xTiO_2 samples were prepared by chemical intercalation of the TiO_2 powder with n-butyllithium [56] (1.6 M Aldrich). The TiO_2 powder was mixed with hexane (95+%, Aldrich), and the n-butyllithium was added while stirring the mixture. Six samples were prepared with different amounts of n-butyllithium to form Li_xTiO_2 with the overall compositions of $x = 0.03$, 0.07, 0.12, 0.25, 0.5, 0.7. All the lithium is intercalated within the TiO_2 powder since n-butyllithium (with a potential of 1 V against lithium) reacts vigorously with anatase TiO_2, as is illustrated by the direct change of color of the TiO_2 powder (white to blue) and the heat that develops during reaction. After 3 days with occasional stirring, the samples were filtered, washed with hexane and dried. All sample preparations were carried out in an argon atmosphere glove box to prevent reactions of Li with air. The darkness of the blue colored powder is visually proportional with the composition (deeper blue for large x). After preparation the samples were subjected to wet-chemical inductively coupled plasma spectroscopy (ICP) analysis to check the overall composition (ratio Li/Ti). These results confirmed that during preparation all the lithium reacts with the TiO_2 (anatase), thus yielding the overall compositions as mentioned. The sample preparation procedure was repeated several times with complete reproducibility.

3.2.2   X-ray powder diffraction

Structural characterization was performed using a Bruker D3 Advance X-ray diffractometer with Cu-Kα radiation. A sample container with airtight Kapton foil windows filled with argon was used to prevent the samples from reacting with moisture or oxygen from air. To make sure the sample did not degrade during an experiment, the most intense lithium titanate peak was monitored before and after the measurement. By visual inspection the sample remained blue for at least several months. The relative amounts of the two phases present in the samples, and the line widths were determined by full Rietveld refinements.

3.2.3   Solid-state NMR spectroscopy.

^{7}Li MAS NMR ($I = 3/2$, 92.6% abundance) spectra were recorded on a Chemagnetics 400 Infinity ($B_0 = 9.4$ T) and a Chemagnetics 600 Infinity ($B_0 = 14.1$ T) operating at 155.4 and 233.2 MHz, respectively. The MAS probe head with 3.2 mm airtight zirconia rotors achieved spinning speeds up to 19.2 kHz in a dry nitrogen atmosphere. Chemical shifts were referenced to a 0.1 M LiCl aqueous solution. The spectra were recorded after a 30° (at $2\omega_{rf}$) radio frequency pulse applied with a recycle delay of 20 s. The 90° pulse length was 1.4 μs. The T_1 relaxation time was determined to be well below 5 s for all temperatures using a saturation recovery experiment. Therefore, a pulse delay of 20 s was sufficient for quantitative measurements. Comparison of the integrated lithium signal intensity detected in Li-Acetate and the Li_xTiO_2 samples indicated that all the lithium present in the samples was detected. In order to observe the effect of degradation of the samples on the NMR spectra, samples were exposed to air intentionally. The spectra changed considerably for samples that were exposed to air for 1 hour, while for 5 hours of exposure the spectrum turned out to be completely degraded yielding a spectrum similar to that of LiOH. Clearly the samples are unstable in air and LiOH is the most likely reaction product formed at the surface of the TiO_2. By visual inspection of the blue coloration it appears that for low values of x the degradation proceeds more rapid than for high values of x. During the work presented here the stability of the samples was monitored directly via the NMR spectra. Two types of NMR experiments were performed yielding different types of information. 1) Structural information is obtained through the chemical shift using single pulse excitation MAS experiments for the different sample compositions. The influence of the temperature on the electronic local environment of Li is observed in terms of its influence on the chemical shift. 2) To explore the Li mobility T_2 relaxation was measured under static, i.e. non-spinning, conditions using a Hahn-echo sequence ($\pi/2 - \tau - \pi - \tau - \mathrm{acq}$) for a range of temperatures (148 – 473 K). Thermally activated Li ion diffusion can increase the spin-spin relaxation time, T_2, with increasing temperature[36], due to the averaging of interactions. The value of T_2, at the temperature just below the temperature at which T_2 starts to increase, is related to the lower limit of the average time a Li ion resides at one site before it hops to another site (correlation time)[36] at that temperature. For the present investigation the T_2 relaxation under static conditions appeared to be more sensitive to Li diffusion than the T_2 relaxation under MAS conditions. The reason for this is that when the spinning speed is significantly larger than the dipolar interactions (both expressed in Hz) the spinning already averages dipolar interactions leaving only relatively smaller effects of Li diffusion on the T_2 relaxation.

3.3   The lithium distributions in Li_xTiO_2

3.3.1   XRD results.

The X-ray diffraction (XRD) patterns for the various amounts of lithium inserted in TiO_2 (anatase) are shown in figure 3.1. The powder pattern of the untreated sample is recognized as that of pure, anatase (space group I4$_1$amd, a=3.784 Å, c=9.510 Å).

The intercalation of lithium causes new reflections to occur in the XRD pattern,
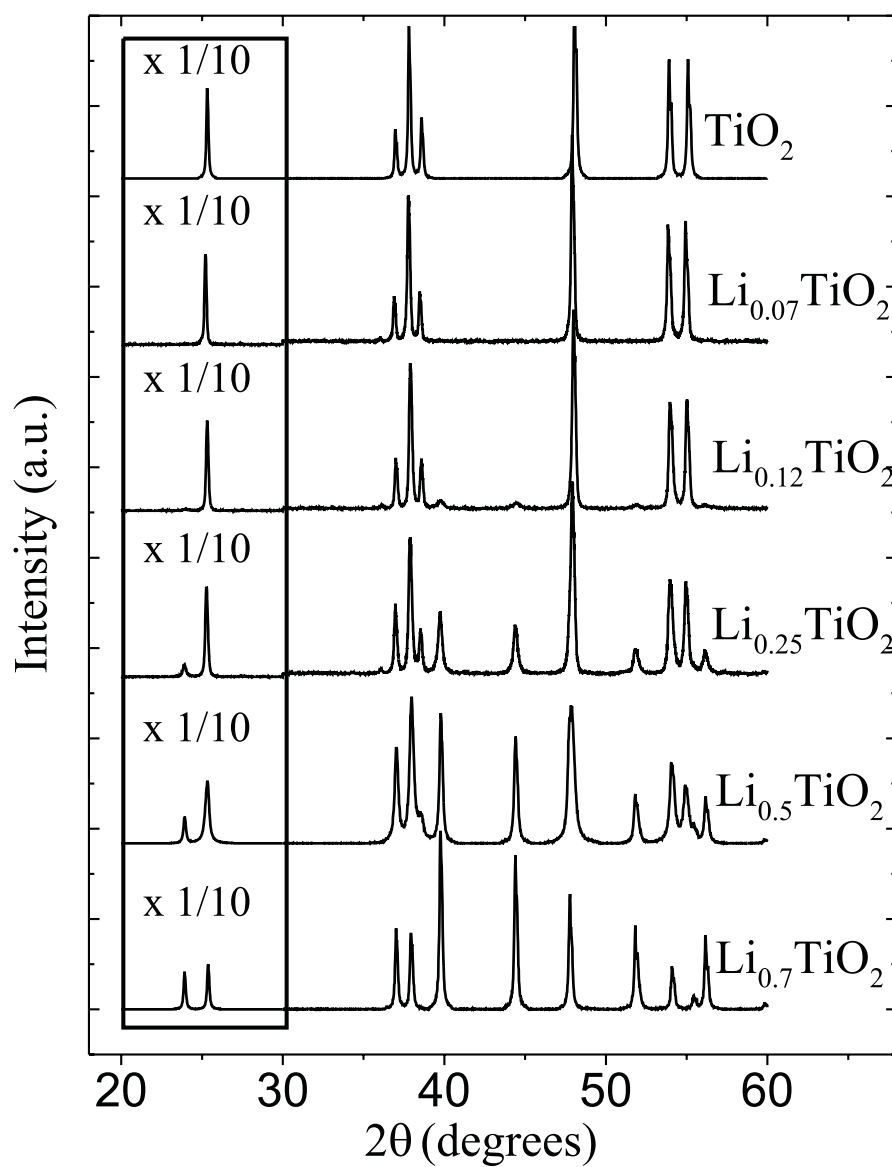
Figure 3.1: *X-ray diffraction spectra of lithium intercalated TiO_2 (anatase) for the different overall compositions. The first part of the spectra is scaled down to get a better view of the second part.*
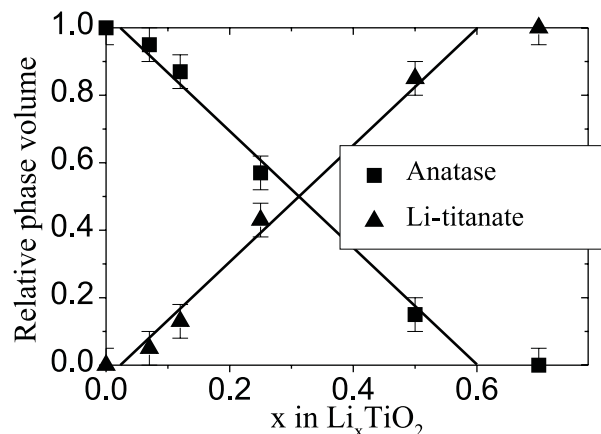
Figure 3.2: *Phase fractions of anatase TiO$_2$ and lithium titanate versus inserted amount
of Li, x=Li/Ti.*

matching those reported in the literature for lithium titanate (Li$_{0.5}$TiO$_2$) [55, 5, 22,
59]. They are in agreement with the orthorhombic unit cell as determined by neutron
diffraction (space group Imma, a=3.806 Å, b=4.077 Å, c=9.067 Å). For the compositions
$x < 0.6$ both phases, anatase and lithium titanate, are present. At $x = 0.7$ all anatase
has been totally phase transformed to the lithium titanate structure, illustrated by the
absence of anatase reflections, see figure 3.1. The presence of two phases may indicate
that lithium is not homogeneously distributed over these two phases. The results are
plotted versus the overall lithium content, x, in figure 3.2. The relative amount of each
crystallographic phase is linearly proportional to the amount of inserted lithium, x. The
Rietveld refinements showed line broadening of mainly the lithium titanate phase that
may be attributed to a typical domain size of about 60 - 80 nm and limited internal
strains. The unit cell of the anatase phase increases by only $\sim$ 0.3 % upon lithium
insertion, while lithium titanate has a 3.3 % larger unit cell, more or less independent of
the overall lithium content x.

3.3.2 ^{7}Li MAS NMR results

The center-bands of the ^{7}Li MAS NMR spectra for the various amounts of lithium
inserted in anatase are displayed in figure 3.4. The full spectra are very similar for
different x, therefore only one is plotted in figure 3.3. Since fast MAS averages the
dipolar interactions, the broad interaction probed by the side bands originates either
from quadrupole interactions or from chemical-shift anisotropy. The field independence
of the static and MAS patterns expressed in Hz (not shown) indicates that it is due to
first order quadrupolar interactions. Spectral decomposition of the center band reveals
several contributions to the spectra that are listed in table 3.1 (at high temperature the
different components are best visible, see also figure 3.8 below). Accurate intensities of
the contributions were obtained from fitting the RT line shapes of the resonance lines
with a mix of a Gaussian and Lorentzian line-shape, and keeping the shape constant for
each of the samples, while fitting the relative intensities.
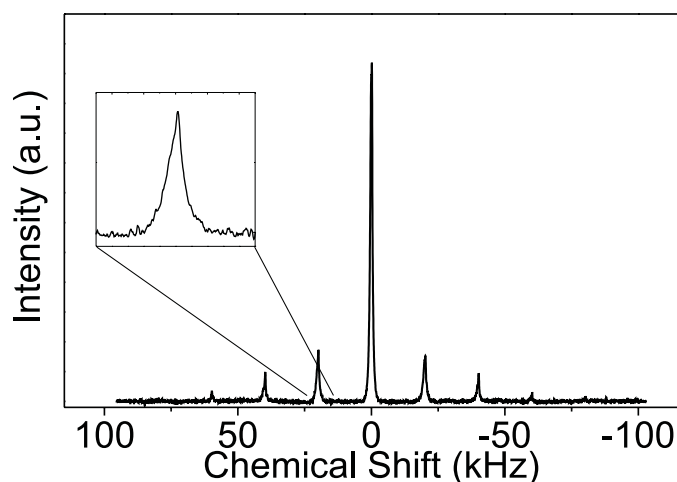
Figure 3.3: *Full ^7Li MAS NMR (Chemagnetics 400) spectrum for overall composition Li$_{0.12}$TiO$_2$, the inset of the first side-band illustrates both species are present not only in the center-band (figure 3.4).*
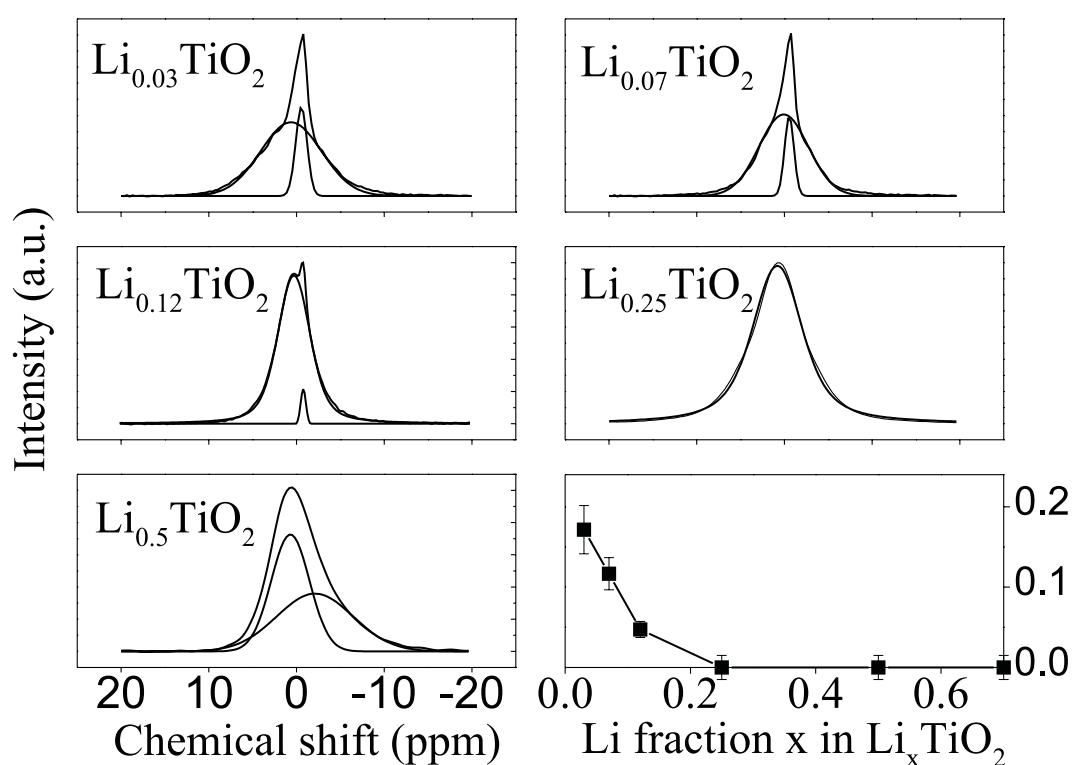
Figure 3.4: *^7Li MAS NMR (Chemagnetics 400) center-band spectra at T = 298 K for different amounts of lithium intercalated, x=Li/Ti, in TiO$_2$ (anatase). The best fits are included, the spectral parameters of which are listed in table 3.1. The bottom right-hand figure represents the relative ^7Li NMR peak area of Li in anatase (species C) versus x.*

Table 3.1: ^7Li MAS NMR (Chemagnetics 400) parameters at T = 298 K for lithium
intercalated in the overall composition $Li_x TiO_2$. Species A refers to Li in lithium titanate
and species C to Li in anatase.

| Sample	Species	δ(ppm)	FWHM (kHz)
x = 0.03	A	0.70 ± 0.1	0.85 ± 0.01
	C	-0.75 ± 0.05	0.15 ± 0.01
x = 0.07	A	0.60 ± 0.1	0.88 ± 0.01
	C	-0.86 ± 0.05	0.16 ± 0.01
x = 0.12	A	0.65 ± 0.1	0.99 ± 0.02
	C	-0.85 ± 0.07	0.14 ± 0.01
x = 0.25	A	0.69 ± 0.1	1.10 ± 0.02
x = 0.50	A	0.65 ± 0.1	1.00 ± 0.01
	B	-2.8 ± 0.3	1.61 ± 0.03

The samples with small Li/Ti ratios have a broad central resonance (species A) as
well as a narrow resonance at about –0.8 ppm (species C). The contribution of the nar-
row resonance to the total spectra decreases with increasing Li/Ti ratio as illustrated
in figure 3.4. Because the NMR measurements are performed quantitatively, the ratio
between the integrated signal observed for both species equals the ratio of the amount
of lithium in both environments. For these quantitative results the whole spectra have
been de-convoluted including the side bands. At the overall composition $x \geq 0.25$ species
C is not visible anymore, and only species A remains. For $x = 0.5$ (and x=0.7) a new
resonance appears at –2.8 ppm (species B). The line shape of the spinning side bands is
much like the center band although the narrow resonance, species C, is relatively weaker.
The resonances referred to as "species A" and "species B" match the resonance observed
by Luca et $al.$ [55]. They assigned species A as Li in the octahedral voids of the lithium
titanate phase and species B was suggested to be the result of a lithium species weakly
coupled to conduction band electrons. The narrow resonance, species C, has not been
observed before. This is not in contradiction with the results of Luca et $al.$ [55] (who
studied compositions $x \geq 0.3$), since species C only appears with measurable intensity
at insertion ratios less than $x = 0.25$. Species A is the result of Li in lithium titanate,

therefore species C must be Li residing in another environment that gradually vanishes with increasing Li insertion as is illustrated by figure 3.4. Therefore the species C has to be assigned to Li in anatase, the initial anatase TiO_2 phase that gradually disappears upon increased lithium insertion. We therefore confirm the thermodynamically stable two-phase system that was previously reported and also predicted by recently performed calculations [9]. Combination of the X-ray and NMR data for the different overall compositions $Li_x TiO_2$ leads to a determination of the lithium fraction in the anatase and in the lithium titanate phase. figure 3.2 gives the amount of both crystallographic phases from XRD while in figure 3.4 the fraction of lithium in the anatase phase is given. Combining these results the composition of the anatase phase is $Li_x(TiO_2)$ with $x \approx 0.01$ and the composition of the lithium titanate phase is $Li_x TiO_2$ with $0.6 < x < 0.7$ for all the samples with overall Li composition $0.03 < x < 0.7$. The latter finding is in agreement with Murphy [59] and Wittingham [56]. Extrapolating the linear behavior in figure 3.2 leads to $x \approx 0.6$ instead of $x = 0.5$ for the lithium rich phase (for the overall composition $Li_{0.5}TiO_2$ the original anatase phase is still present, figure 3.1). Clearly for increasing lithium concentration there is a strong preference for the lithium titanate structure (composition $Li_{0.6-0.7}TiO_2$). The result indicates that the phase separation in anatase and lithium titanate takes place at even lower lithium concentrations than the suggested $x = 0.05$ by van de Krol *et al.* [58]. Having assigned species C to lithium in anatase TiO_2 the chemical shift might lead to an indication of the oxygen coordination and thus to the position of lithium in the anatase lattice. Based on the resemblance of the anatase and lithium titanate structure one might expect Li in anatase to reside in the octahedral voids. Lithium in lithium titanate is effectively five-fold coordinated to oxygen (in the *a-b* plane two oxygens at 1.97 Å and two at 2.04 Å, and in the *c*-direction one at 2.17 Å and one at 2.8 Å), while Li in the middle of the octahedral site in anatase is effectively four-fold coordinated (four oxygens in the *a-b* plane at 1.93 Å and two in the *c*-direction at 2.78 Å). In absence of other mechanisms influencing the chemical shift, five-fold oxygen coordination would lead to a more positive chemical shift [60] for lithium in lithium titanate. This is indeed the case as can be confirmed inspecting figure 3.4, indicating that the Li may be in the octahedral voids. Another feature of interest in the MAS spectra of figure 3.3 is the presence of spinning side bands. This broad spinning side band manifold is a result of the interaction of the ^{7}Li quadrupole moment (-3 × 10^{-30} m^2) with the electric field gradient. The quadrupole interaction (C_Q) is, next to the chemical shift, a second sensitive probe of the chemical environment of Li. The side bands belong to both lithium in lithium titanate and in anatase. However, since the Li in anatase resonance is relatively weak, the width of its quadrupolar interaction is difficult to determine. Based on the positions of the ions surrounding Li and assuming point charges (*i.e.* an ionic charge model), an estimate for the quadrupole interaction constant, C_Q, and the asymmetry parameter, η, can be computed [61]. Using the position of Li in the lithium titanate [4] structure leads to $C_Q = 159$ kHz and $\eta = 0$ if the six nearest neighboring atoms are considered (all oxygen). This is in agreement with the width of the observed side band manifold, which equals 160 kHz at T = 298 K figure 3.3. For Li in the center of the anatase octahedral voids one obtains $C_Q = 299$ kHz. Based on these values for C_Q the second order quadrupole broadening and the quadrupole induced shift can be calculated to be negligible in the presented measurements. The chemical shifts of both resonances can therefore be considered isotropic. The intensity of Li in anatase

in the side bands is unfortunately too weak to decide on the correctness of this value and therefore on the position of Li in the anatase lattice. The small concentration of Li in anatase complicates the experimental determination of the Li position in anatase by means of neutron diffraction, and to the best of our knowledge it is not reported in literature. However, the distorted octahedral voids are the most likely Li positions since it is not in contradiction with the data and also in view of the position Li has in the very similar lithium titanate structure. When examining the data, it appeared that there is a slight temperature dependence of the relative amounts of Li in the anatase TiO_2 and lithium titanate phase. When fitted using a Boltzmann distribution the Li in anatase could be viewed as being in an energy level ~ 31 K above that of Li in lithium titanate. The small change in the relative amounts of Li in both phases shows that there is exchange of Li on prolonged time scales between the two phases. This is a matter of further investigation and falls outside the scope of this paper.

3.3.3   Origin of the ^7Li MAS NMR line-width

The two Li-ion environments associated with Li in the anatase lattice and Li in the lithium titanate lattice have a striking difference in resonance width as can be seen figure 3.4 and in table 3.2. Especially considering the similarity of the anatase structure and the lithium titanate structure one might wonder what the origin of the difference is. Under MAS conditions the dipolar interactions and chemical shift anisotropy can be considered to have negligible contribution to the line width. Therefore we need to consider the quadrupolar interactions and coupling mechanisms with electrons. In table 3.2 the width of the two resonances is given for two field strengths. From the field dependence it is clear that the width scales linearly with the field. This directly rules out quadrupolar interactions, as first order effects are field independent and second order line-broadening is reversibly proportional to the field. Hence, a coupling with electronic orbitals should be considered. With respect to that it is interesting to mention that Luca *et al.* attributed the existence of the ^7Li resonance labelled B, which appears at Li/Ti$\approx$0.5 (see table 3.2), to a weak coupling with conduction electrons. This resonance appears to be broader than resonance A. A clear tendency is observed, increasing the lithium insertion ratio, leading to a higher charge compensating electron density, results in larger line-widths for the NMR ^7Li resonance. For lithium intercalation it is expected that the charge compensating electrons occupy the bottom of the conduction band which mainly exists of Ti-*3d* orbitals [20]. Hence the suggested coupling of Li with the charge compensating electrons might be explained in terms of a coupling with the Ti-*3d* electron density, apparently proportional to the electron density.

3.4   Lithium mobility

3.4.1   Static and MAS^7Li NMR results

In the remainder we concentrate on the sample with overall composition $Li_{0.12}TiO_2$ where species A and C are both measurable, i.e. $x < 0.25$. The static ^7Li spectra for overall composition $Li_{0.12}TiO_2$ at different temperatures are displayed in figure 3.5. The broad,

Table 3.2: ^7Li MAS NMR parameters at $T = 298$ K for lithium intercalated TiO_2 at two different field strengths; 9.4 and 14.1 T (Chemagnetics 400 and 600). Species A refers to Li in lithium titanate, species B to the second Li-environment in Li-titanate for $Li/Ti \geq 0.5$ and species C to Li in anatase.

Species	Field [T]	FWHM [kHz]	FWHM [ppm]
A	9.4	0.99	6.43
B	9.4	1.61	10.36
C	9.4	0.14	0.90
A	14.1	1.51	6.50
B	14.1	2.43	10.42
C	14.1	0.23	0.97

~ 160 kHz, wings in the spectra stem from the powder pattern of the $\pm\frac{1}{2} \leftrightarrow \pm\frac{3}{2}$ satellite (nuclear spin) transitions which are separated from the central transition due to the quadrupole interactions described above. The central peaks in figure 3.5 can be decomposed into two more narrow components resulting from the $-\frac{1}{2} \leftrightarrow +\frac{1}{2}$ central transition of, respectively, Li in lithium titanate (~ 12 kHz below 198 K) and Li in anatase (~ 1.3 kHz below 198 K). These two central transitions of Li in both phases display strong line narrowing with increasing temperature above 198 K. This is attributed to motional narrowing as a result of increased lithium mobility in the lattice. Motional narrowing occurs when the lithium hopping frequency between sites exceeds a relevant nuclear hyperfine interaction (expressed in Hz), ultimately leading to effective averaging of the interaction. The possible relevant interactions of ^7Li with its environment are 1) the magnetic dipolar coupling and 2) the quadrupolar interaction. Both are discussed in more detail with respect to mobility in the following.

1) Given the largest nuclear spins of Ti (^{49}Ti: -1.1039 μ_N, 5.5 % natural abundance (n.a.); ^{47}Ti: -0.7883 μ_N, 7.5% n.a.), O (0.0 μ_N) and Li (^7Li: 3.256 μ_N, 92.5% n.a.; ^6Li: 0.822 μ_N, 7.5% n.a.) the nuclear dipolar interaction in poly-crystalline anatase and lithium titanate can be estimated [37]. The dipolar coupling in lithium titanate will be dominated by the Li-Li interactions on the shortest possible Li-Li distances (2.54 Å) [4] while for the low density of Li in anatase the dipolar interaction will be dominated by the shortest Ti-Li distances (2.676 Å). The lattice sum of all the dipolar interactions leads for lithium titanate to a static (or rigid lattice) powder line width of ~ 8 kHz, and leads for anatase to ~ 1.0 kHz assuming that for both phases Li resides in the center of the oxygen octahedra. For both species the calculated value is smaller, but in fair agreement with the line width observed in the decomposition of the central peak in the low-temperature spectra (table 3.3). It is worth mentioning that the difference in NMR line-width between species A and C can now be explained from the difference in Li density
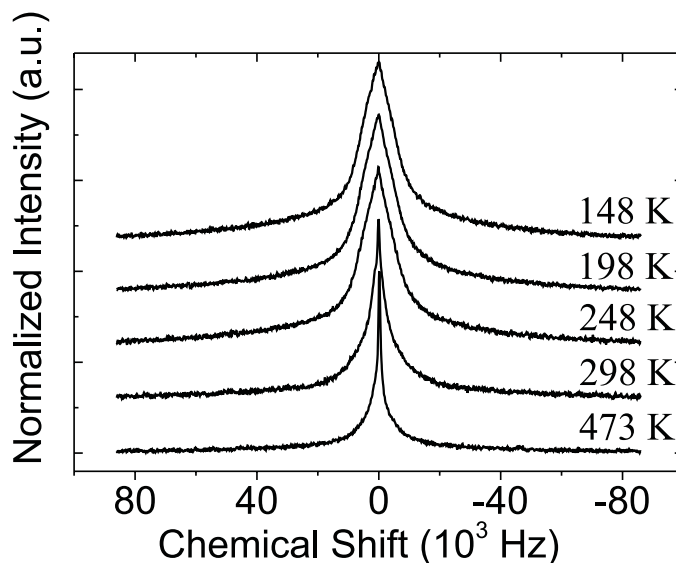
Figure 3.5: *^7Li static NMR (Chemagnetics 600) spectra for overall composition $Li_{0.12}TiO_2$ obtained with a Hahn-echo-pulse sequence for a number of temperatures illustrating the effect of Li diffusion on the line-width (motional narrowing).*

between Li in anatase (species C) and Li in lithium titanate (species A). Li diffusion can average the dipolar interaction to zero, provided that Li hopping rates are fast compared to the dipolar interactions [36] in lithium titanate and anatase, respectively.

2) The symmetry of the octahedral voids in both lithium titanate and anatase is such that the different sites have opposite orientation of the quadrupole tensor with respect to the applied field but no difference in absolute value. As a result, the quadrupolar interaction may be averaged within one powder particle assuming it is a single crystal, leading to a collapse of the spectrum towards the central line. The quadrupolar interactions of more than 100 kHz are larger than the dipolar interactions. This implies that the dipolar interactions should start to be averaged by motions at lower temperatures than the quadrupolar interactions. The present results do not show significant change in the width of the quadrupole spectrum with temperature. Therefore, the Li mobility was not high enough to cause a significant collapse in the MAS spectra, and the spinning side bands to disappear. It may also be noted that for the relatively small quadrupolar interaction the second order quadrupolar interaction is negligible compared to the line widths observed. In view of the above considerations, figure 3.5 indicates the averaging of the nuclear dipolar interactions of Li in both the anatase and lithium titanate environment, clearly evidencing temperature dependent Li mobility in both phases. It should be noted here that the dipolar interactions can only be averaged significantly when the positions of Li nuclei relative to all other nuclei sample many different positions with sufficiently fast rates. More local Li motion, e.g. inside the octahedral sites, is not enough to yield the strong motional narrowing effects as observed, since the average position relative to the other nuclei does not change significantly, and with it, the dipolar relaxation does not change much. In fact, local motions -if present- may be expected on more rapid time scales than probed with T_2, i.e. they may be visible in a temperature dependence of T_1.

Table 3.3: *Spectral decomposition of the ^7Li Static NMR (Chemagnetics 400) central transition for a range of temperatures (overall sample composition $Li_{0.12}TiO_2$). Species A refers to Li in lithium titanate and species C to Li in anatase.*

Temperature (K)	Species	δ(ppm)	FWHM (kHz)
148	A	0.59 ±0.15	11.8 ± 0.2
	C	-0.73 ± 0.10	1.35 ± 0.07
198	A	0.6 ± 0.16	11.8 ± 0.2
	C	-0.70 ± 0.09	1.35 ± 0.11
248	A	0.65 ± 0.15	11.7 ± 0.2
	C	-0.67 ± 0.08	1.12 ± 0.19
298	A	0.61 ± 0.13	11.2 ± 0.2
	C	-0.80 ± 0.07	0.89 ± 0.04
398	A	0.55 ± 0.11	6.94 ± 0.15
	C	-1.4 ± 0.07	0.63 ± 0.05

Because the latter is almost absent in both phases, this indicates that there is no relevant Li (local) motion on time scales close to the Larmor frequency ($\sim 10^7$-10^9 Hz). We also have to conclude that the change observed in T_2 is due to Li hopping between different interstitial sites. An often-applied model for the spin-spin relaxation due to fluctuations in the dipolar interactions caused by diffusion is the Bloembergen, Purcell and Pound (BPP) model [41]. An example for the determination of diffusion coefficients using the BPP model for T_2 relaxation, and comparing them with macroscopic data, is Holcomb *et al.* [42] for alkali metals Na and Li. In the following, the BPP model will be applied.

3.4.2   Mobility from T_2 spin-spin relaxation.

Now that we know the origin of the line narrowing, a quantitative analysis of the motion can be performed by analyzing the spin-spin relaxation times as a function of temperature. The static T_2 spin-spin relaxation time for each of the phases is shown in figure 3.6, at temperatures ranging from 148 K to 473 K. For both species, T_2 does not vary until a certain temperature, while for higher temperatures a significant increase is observed. In case of identical nuclei, the BPP model for T_2 relaxation only taking into account the

first neighbors yields [41]:

$$\left(\frac{1}{T_2}\right)^2 = C_{dipole} \arctan \frac{2\tau_c}{T_2}, \qquad (3.1)$$

where C_{dipole} is proportional to the rigid lattice second moment $< \Delta\omega^2 >$, τ_c is the correlation time defining the time between Li hops, and ω_0 the Larmor frequency. In this case we neglect the effect of T_1 on the actual line width because $T_1 >> T_2$, so that T_2 in equation 3.1 is proportional to the line width. The expression for $1/T_2$ holds only for rapid motion i.e. $< \Delta\omega^2 >^{\frac{1}{2}} \tau_c << 1$, for slow motion i.e. $< \Delta\omega^2 >^{\frac{1}{2}} \tau_c >> 1$, $1/T_2$ equals the static line width $< \Delta\omega^2 >^{\frac{1}{2}}$. Between the two regimes a breakpoint occurs where $\tau_c = \frac{T"_2}{\sqrt{2}}$, where $T"_2$ is the relaxation time associated with the static line width. If we assume the mobility of the ions to be thermally activated, the correlation time will obey an Arrhenius law, $\tau_c = \tau_\infty e^{\frac{E_A}{k_B T}}$, where E_A is the activation energy of the jump process and $\frac{1}{\tau_\infty}$ the attempt frequency. For high temperatures such that $2\tau_c/T_2 << 1$, the BBP model in equation 3.1 can be approximated by $\frac{1}{T_2} \approx C_{dipole}\tau_c \propto \tau_\infty e^{\frac{E_A}{k_B T}}$. Therefore an Arrhenius plot of $\ln(\frac{1}{T_2})$ versus $\frac{1}{T}$ in this range leads to a determination of the activation energy. Figure 3.6 gives the Arrhenius plot for both phases. The linear fit results in activation energies of $E_A = 0.20 \pm 0.01$ eV (2400 K) and $E_A = 0.09 \pm 0.01$ eV (1000 K) for Li in anatase and lithium titanate, respectively. The breakpoint between the low and high mobility regime indicated by the crossing lines in figure 3.6 leads via $\tau_c = \frac{T"_2}{\sqrt{2}}$ to approximate values for the correlation time, 0.17 ms at $\sim$250 K for anatase and 0.019 ms at $\sim$290 K for lithium titanate. With these values τ_∞ is computed to be 16 ns for Li in anatase and 620 ns for Li in lithium titanate. At room temperature this leads to $\tau_c = 47\mu s$ for anatase and $17\mu s$ for lithium titanate.

An estimate of the microscopic diffusion coefficient D at room temperature can be determined with $D = \frac{l^2}{n\tau_c}$, where l is the length of an elementary jump between sites and n the number of possible jumps to different nearest neighbor sites. In both phases lithium can be expected to hop from the octahedral interstitial sites to four other equivalent sites ($n = 4$) at a distance 2.96 Å for anatase and 3.03 Å[19] for lithium titanate, resulting at room temperature in $D_{micr} = 4.7 \times 10^{-12} cm^2 s^{-1}$ and $D_{micr} = 1.3 \times 10^{-11} cm^2 s^{-1}$, respectively. The dependence on overall Li content was checked by performing similar experiments as described for Li$_{0.12}$TiO$_2$ for the overall composition of Li$_{0.07}$TiO$_2$. This resulted in the same results for the Li mobility in both phases.

3.4.3   Discussion.

The estimated values for the microscopic diffusion coefficients in both phases are considerably larger than many reported in literature for electron beam evaporated [7] and CVD [5] films ($\approx 10^{-15} cm^2 s^{-1}$) for the overall diffusion coefficient of Li in TiO$_2$ as determined with electrochemical techniques. Furthermore the activation energy for Li hopping is in both anatase and lithium titanate considerably smaller than values determined electrochemically via the temperature dependence of the diffusion coefficient: $E_A = 0.54$ eV and 0.78 eV [5] (insertion and extraction) and 0.6 eV [18]. The main difference between electrochemical methods and NMR that may explain the differences in diffusion constants is that NMR probes diffusion rates at a scale of nanometers. Therefore, Li
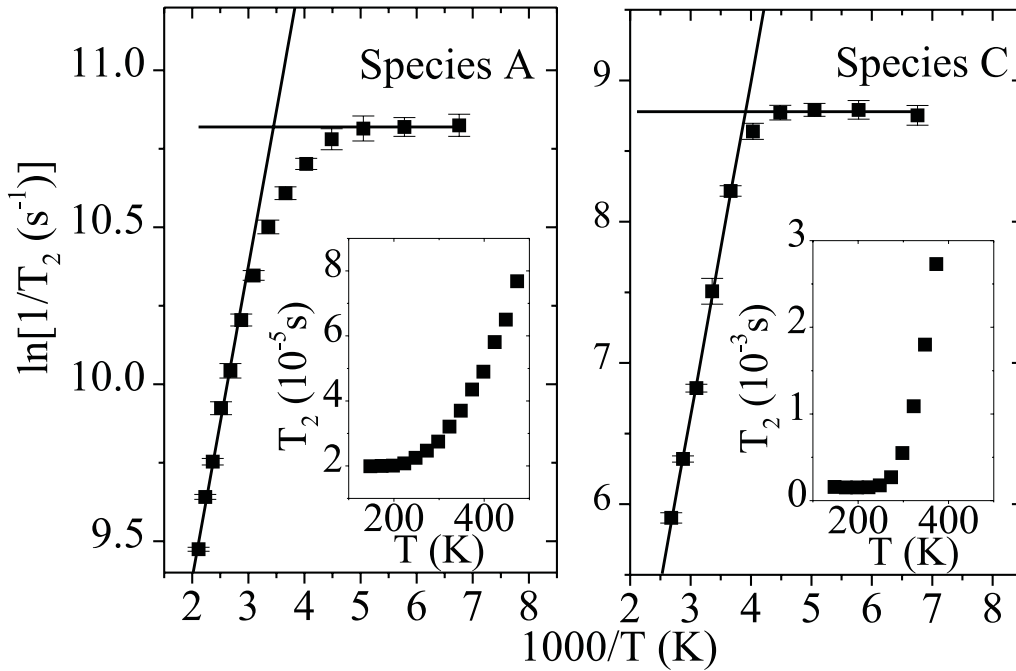
Figure 3.6: *Arrhenius plot of the ^7Li spin-spin relaxation time, T_2, for the coexisting phases with the overall sample composition $Li_{x=0.12}TiO_2$ (species A: Li in lithium titanate, species C: Li in anatase). The data were acquired under non-spinning conditions (Chemagnetics 600). The lines cross at a temperature where the T_2 can directly be related to correlation time of Li motion. The insets give the same results plotted as T_2 versus temperature.*

diffusion observed by NMR is not affected by surface effects, grain boundaries or crystallographic phase boundaries. In principle, these types of diffusion need not have the same activation energy, and they all may be a result of overall diffusion limiting processes in a macroscopic electrochemical diffusion measurement. In fact, one of these processes has to limit the electrochemically determined diffusion coefficient, because the diffusion within each phase is higher and has lower activation energy. For macroscopic Li intercalation in TiO_2, the bulk diffusion is considered to be rate limiting [7] which eliminates surface effects (contact with the electrolyte) to dominate the overall diffusion. The effect of grain boundaries between different crystallites can be illustrated by a study on Li insertion in single crystal TiO_2 (anatase) that reported electrochemically determined diffusion coefficients of respectively 2×10^{-13} and 6×10^{-13} cm^{2}s^{-1} for Li insertion and extraction [6]. Compared to the $D \approx 10^{-15}$ cm^{2}s^{-1} on poly-crystalline materials these values are relatively closer to the present observation ($D_{micr} = 4.7 \times 10^{-12}$ cm^{2}s^{-1} and $D_{micr} = 1.3 \times 10^{-11}$ cm^{2}s^{-1}). Note that one can actually not speak of single crystalline anatase, because Li insertion is accompanied with the phase transition from anatase ($Li_{0.01}TiO_2$) towards lithium titanate ($Li_{0.6}TiO_2$), resulting in the two coexisting phases. The "single crystal" values for the diffusion coefficient (2×10^{-13} and 6×10^{-13} cm^{2}s^{-1}) [6] thus include the phase boundary dynamics and the diffusion of Li through this crys-
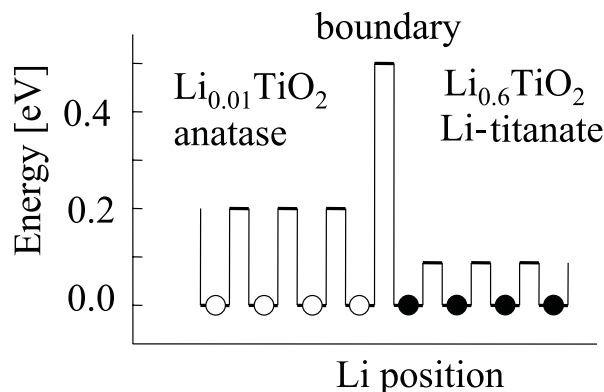
Figure 3.7: *Schematic view of the energy barriers for Li motion in the anatase and lithium titanate two-phase system constructed from the microscopic activation energies in combination with macroscopic Li transport measurements.*

tallographic phase boundary. The "single crystal" result for the diffusion coefficient is still more than one order of magnitude smaller than the present results for within each phase. Assuming the experimental observations at the macroscopic level [18, 5] and at the microscopic level (the present investigation) are correct, the macroscopic activated behavior with $E_A \approx 0.5$ eV can not be due to Li inside each of the two phases, for the simple reason that Li has a lower E_A in both phases (0.2 and 0.09 eV respectively). This leads to the proposition that the microscopic diffusion within the phases is not rate limiting, but the Li diffusion between phases (or the movement of the phase boundary) must be overall diffusion rate limiting.

The energy barriers encountered by a single Li ion in the two-phase system resulting from the discussion above is sketched in figure 3.7. The bottoms of the potential wells in anatase and lithium titanate differ only 31 K ($\sim$3 meV). Li moving through this system will encounter different barriers. Upon Li insertion from the right the Li will have to cross the large 0.5 eV barrier (approximate value found in macroscopic measurements), while for extraction towards the right only smaller 0.09 eV barriers are encountered. The overall diffusion would be limited by the largest barrier, which is formed by the phase boundary. In principle such a model could explain that there is a smaller overall diffusion coefficient for insertion than for extraction of Li.

3.5 Electronic structure

3.5.1 Temperature dependence of the chemical shift

In figure 3.8 and 3.9 the chemical shift (CS) variations of Li in anatase (species C) and of Li in lithium titanate (species A) versus temperature are plotted for overall composition Li$_{0.12}$TiO$_2$. Similar results were obtained for overall composition Li$_{0.07}$TiO$_2$ (not shown). The chemical shift of Li in anatase is constant for T = 173-273 K, while it decreases approximately linearly for T = 298-473 K. The chemical shift of Li in lithium titanate (species A) seems to display the same behavior although less prominently. As a result
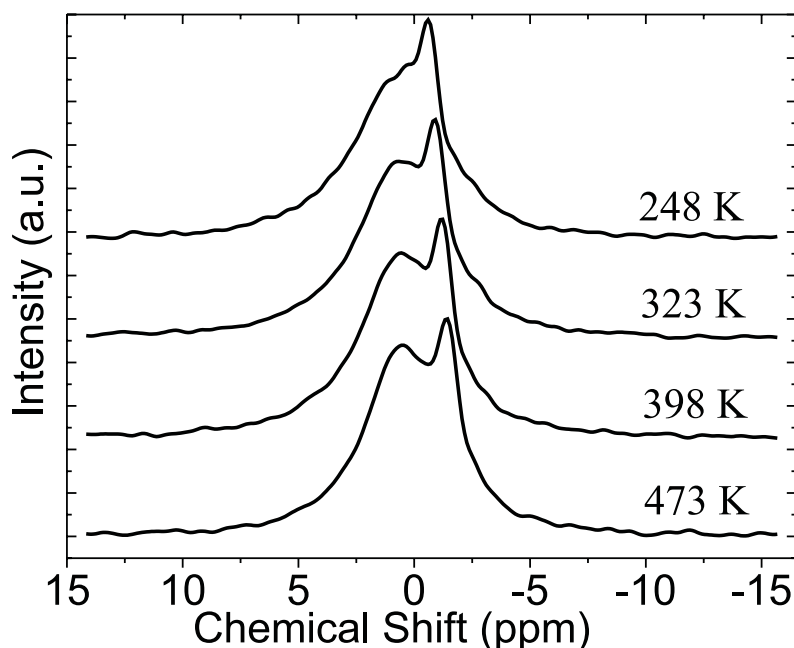
Figure 3.8: ^7Li *MAS center band for overall sample composition* $Li_{0.12}TiO_2$ *for different temperatures illustrating the temperature dependence of the chemical shift.*

of the larger line width of species A, compared to that of species C, its chemical shift values are less accurate.

The decrease of the CS with temperature indicates a reduction in the field measured at the Li nucleus. The structure at these temperatures is not expected to change and thermal expansion has a different temperature dependence than observed for the CS. Thus the observed shift is most likely the result of interactions of the Li nucleus with (conduction) electrons. There are two mechanisms to consider. First, paramagnetic interaction with unpaired localized electrons can influence the CS. Second, the Li nucleus may interact with conduction electrons (Knight shift).

3.5.2 Discussion

In principle, anatase TiO_2 is a large gap semi-conductor with band gap $\sim$3 eV. Upon $Li^+ + e^-$ insertion, the electron may become localized on Ti or it may be inserted in a conduction band. If the electron becomes localized on Ti^{3+} the atom might have a paramagnetic moment (if it is not quenched), while Ti^{4+} is non-magnetic. Paramagnetic ions lead through Fermi-contact interactions and through space dipolar interaction to a paramagnetic induced shift which has a Curie-Weiss $1/T$ temperature dependence. The small variation with temperature of the CS of Li in TiO_2 starting at $\sim$250 K in figure 3.9 can not be described with such temperature dependence. Another argument for the absence of paramagnetic Ti^{3+} is the value of the T_1 relaxation parameter in these materials, which is well above 1 s. In materials with paramagnetic ions, T_1 is lowered significantly, even for very low concentrations, and can become as low as 10^{-4}s. The presence of
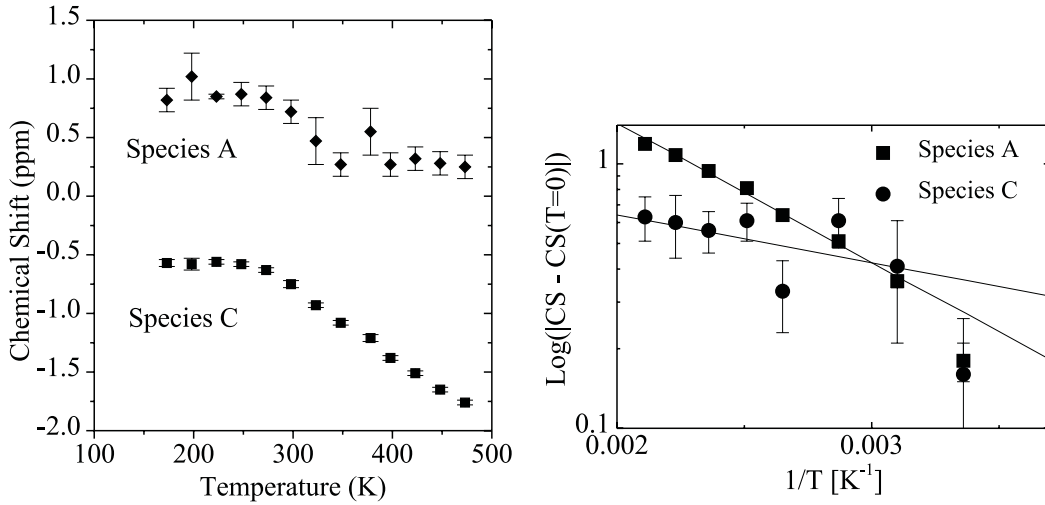
Figure 3.9: *Left:Temperature dependence of the ^7Li MAS chemical shift in anatase (species C) and lithium titanate (species A) for the overall sample composition $Li_{0.12}TiO_2$. Right: Arrhenius plot of the chemical shift (CS) vs. temperature for ^7Li in anatase (species C) and in lithium titanate (species A) for the overall sample composition $Li_{0.12}TiO_2$. The fits result in an activation energy of 100 ± 10 meV in anatase and 40 ± 30 meV in lithium titanate, which is interpreted as the energy below the conduction band of the Li-induced donor level, see text.*

localized electron states leading to paramagnetic Ti^{3+} is thus unlikely. This is also in agreement with magnetic susceptibility and EPR results of Luca *et al.* [55], indicating that the Ti^{3+} density has to be very small. Since there appears no room to interpret the results in terms of localized electron states, one should expect a more delocalized electron density. It is known that for pure anatase TiO_2 above 150 K there is a contribution to the magnetic susceptibility from the conduction band electrons [62]. These conduction electrons have, in principle, a temperature independent Pauli paramagnetism. However, the occupation of the conduction band in a semiconductor like anatase TiO_2 and low Li concentration doped anatase $Li_{0.01}TiO_2$ depends on temperature, which leads to intrinsic temperature dependence. This can be understood in terms of Li-induced localized donor levels below the conduction band as was indicated by a theoretical study [19]. The contribution of the conduction electron density to the chemical shift, referred to as the Knight shift K, is thus in principle dependent on temperature. The basic equation for K is:

$$K = \frac{\Delta\omega}{\omega} = \frac{8\pi}{3}\chi_e \left\langle |u(0)|^2 \right\rangle_{\varepsilon_F}, \qquad (3.2)$$

where χ_e is the Pauli susceptibility of the conduction electrons, and $\left\langle |u(0)|^2 \right\rangle_{\varepsilon_F}$ represents the electron density with energy close to the Fermi level ε_F as measured at the Li nucleus. In Li intercalated TiO_2 (anatase) the conduction band is mainly build out of *3d* orbitals [19, 63], as is also more general the case for transition metal oxides [20]. Since Li has O as nearest neighbors, the effect of *3d* electron densities on the electron densities at ^7Li and the CS must therefore be transferred via O electronic states towards

the Li atom. It is known that there can be a slight admixture of the O-$2p$ states in the conduction band in lithium titanium oxides [63], which would mean that increasing conduction electron densities slightly increase the O-$2p$ occupations. Such an increase in O-$2p$ density appears to reduce the occupation of Li-$2s$ states (by core polarization), resulting in a lowering of K with increasing temperature. The temperature dependence of the [7]Li CS in anatase and in lithium titanate (lower CS with higher T) may therefore indicate an increase of the delocalized Ti-$3d$, O-$2p$ electron density with temperature. The potential of lithium intercalation is sensitive to the admixture of O-$2p$ states in the conduction band [64], indicating that these states are also important for the potential landscape encountered by Li.

The notion that progressive lithium intercalation fills the Ti-$3d$ conduction band with electrons that interact with the Li-nucleus is in agreement with the suggestion made in section 3.3.3 that the line width of the observed resonances A, B and C is proportional to the charge compensating electron density.

If the temperature-dependent chemical shift is interpreted as an increase of the Ti-$3d$ electron density, it can be used to get an estimate of the depth of the suggested donor state.

An Arrhenius plot of the chemical shift of both species is shown in figure 3.9 indicating that it can be interpreted as a thermally activated process. The fits result in an activation energy of 100 $\pm$10 meV in anatase and 40 $\pm$30 meV in lithium titanate, which is interpreted as the energy of the Li-induced donor level below the conduction band. This value is not compatible with the calculated value, 1.2 eV [19], however the qualitative picture in terms of donor states seems to be confirmed by the present NMR results.

Concerning the interaction with conduction electrons, it is also interesting that Luca *et al.* [55] concluded that the negative shift of resonance B (only detected for overall composition $x > 0.3$) was due to a weak coupling of the Li nucleus to conduction band electrons. Luca *et al.* did not detect any temperature dependence for species A and B between 200-300 K. This is not in contradiction with the present results, since the temperature dependence starts above 250 K and the effect is rather small for species A. At the same temperature that the chemical shift starts to be temperature dependent, the lithium appears to be mobile in both anatase and lithium titanate. This may suggest that the activation energy for Li motion is influenced by excitations in the electronic environment. A mechanism for that would include the enhanced electronic screening of the ionic charges surrounding Li by conduction electrons. Based on quantum chemical calculations, Lunell *et al.* [18] suggested a coupling between electron and a diffusing ion in such a way that the charge-compensating electron occupies the $3d$-states of the nearest neighboring Ti atoms, and effectively follows the lithium ion when it diffuses. This is corroborated by the present interpretation of the temperature dependent CS in the following way. With increasing temperature, the Ti-$3d$, O-$2p$ conduction band occupation is increasing, while core polarization of the Li-$2s$ states decreases the electron density measured directly at the Li nucleus. This would explain the observed small decrease of the [7]Li CS. Thus the small variation in the electron density measured at the Li nucleus indicates that the conduction electrons extend over some distance. The time scales of the Li ion hopping (slow) and the electronic mobility (fast) will be very different, which would imply that effectively a delocalized electron cloud is surrounding

the Li ion on its way. Possibly, this influences the potential landscape in such a way that it facilitates Li mobility.

3.6   Conclusions

The NMR results allow the assignment of two coexisting lithium containing crystallographic phases in TiO_2 (anatase): a Li rich (lithium titanate) and a Li poor phase (anatase). The combination of X-ray and NMR data for the different overall compositions of $Li_x TiO_2$ leads to a Li fraction in the Li poor anatase phase of $x \approx 0.01$, and $0.6 < x < 0.7$ in the Li rich lithium titanate phase for all samples investigated. Apparently, TiO_2(anatase) allows only a small Li fraction ($x \approx 0.01$) in the tetragonal structure before the Li imposes the phase transition towards the orthorhombic lithium titanate structure. Motional narrowing and the large variation of the spin-spin T_2 relaxation times prove the lithium in both phases to be mobile at room temperature on a time scale in the order of 47 μs in anatase and 17 μs in the lithium titanate. The Arrhenius behaviour of T_2 *vs* temperature indicates activated Li hopping with activation energy 0.2 eV in the Li poor anatase and 0.09 eV in the Li rich lithium titanate. The room temperature microscopic diffusion coefficients in the anatase and in the lithium titanate phase are 4.7×10^{-12} cm^{2}s^{-1} and 1.3×10^{-11} cm^{2}s^{-1}, respectively. The difference between the results obtained here for the microscopic diffusion and the overall macroscopic diffusion determined by others suggest that the lithium diffusion through, or the dynamics of, the phase boundaries in this two phase system limits the overall diffusion, and also dictates the overall activation energy. The chemical shifts of lithium in anatase and in lithium titanate are independent of temperature up to about 250 K, and decrease at higher temperatures, indicating a change in mainly the 3d-conduction electron density. The change becomes observable at the same temperature that motion of Li appears, suggesting that the electronic structure influences the Li mobility.

Chapter 4

Lithium diffusion between nano-crystalline phases in intercalated anatase TiO$_2$

Abstract

Lithium intercalation in anatase TiO$_2$ micro particles produces a nano-morphology of coexisting lithium-poor Li$_{0.01}$TiO$_2$ and lithium-rich Li$_{0.6}$TiO$_2$ domains. The existence of a two-phase equilibrium system in an electrode material provides the, for batteries desired, constant electrochemical potential as a function of Li content. The equilibrium must be defined and maintained by continuous exchange of charged particles between the phases, but on which time and length scales does this take place? Here we report the direct observation by solid state nuclear magnetic resonance (NMR) of the continuous Li ion exchange between these intermixed crystallographic nano-phases. At room temperature the continuous Li flux through the phase boundaries is $\approx 0.6 \times 10^{20}\ s^{-1}m^{-2}$. The corresponding diffusion coefficient suggests that the phase boundaries are rate limiting in the overall diffusion process. In practice this means that the boundary limits the rate at which lithium can be inserted in TiO$_2$ (anatase) in a battery configuration.

4.1   Introduction

In chapter 3 [23] it was shown that upon lithium intercalation anatase splits up in a lithium-poor phase Li$_{0.01}$TiO$_2$ with the anatase structure (space group I41/amd) and a lithium-rich phase denoted as lithium titanate (space group Imma). For overall compositions Li$_{0.01<x<0.6}$TiO$_2$ the two phases appear to coexist. Upon discharging TiO$_2$ as anode in a battery, Li is extracted from the two-phase system, reducing the Li-rich phase and increasing of the Li-poor phase. As long as both phases are present (and in thermal equilibrium) the electrochemical potential and the electrical potential of the battery are well defined and constant. In order to achieve and maintain thermodynamic equilibrium

there should be lithium transport between the two phases. This is just like the equilibrium between a liquid and its vapor that is maintained by continuous exchange of molecules between liquid and vapor.

In chapter 3 it was suggested that the transport between the two phases is rate limiting for the overall diffusion rate as determined with macroscopic techniques. The microscopic diffusion rate within the two phases was found to be considerably larger compared to macroscopic values, Li in anatase: $D_{micr} = 4.7 \times 10^{-12}$ cm^{2}s^{-1} and Li in lithium titanate: $D_{micr} = 1.3 \times 10^{-11}$ cm^{2}s^{-1} compared to macroscopic values in single crystal TiO_2 (which in fact does not remain a single crystal as Li is intercalated) between 2.0-6.0 $\times 10^{-13}$ cm^{2}s^{-1} [6] and 2.0-6.0 $\times 10^{-15}$ cm^{2}s^{-1} for CVD films [5]. Activation energies of the diffusion in both phases were found to be much lower than found macroscopically, 0.2 eV in anatase and 0.09 eV in lithium titanate [23] compared to $\geq$0.5 eV found macroscopically [5, 18]. In this chapter the rate and activation energy for diffusion between the Li-poor anatase phase and the Li-rich lithium titanate phase is determined. This gives insight into the time- and length-scales on which equilibrium particle transport takes place.

We perform ^{7}Li magic angle spinning (MAS) solid state NMR since this is an excellent microscopic probe giving information on structure and dynamics. The presence of exchange of Li between two phases is established by performing two-dimensional exchange measurements [65]. This technique effectively measures the spectrum of the ^{7}Li atoms at $t = 0$ s, then waits a "mixing time", t_{mix}, and subsequently measures the spectrum of the same ^{7}Li atoms again at $t = t_{mix}$. These relatively time consuming 2D experiments are used to qualitatively describe the exchange of Li from one phase to the other and *vice versa*. Faster 1-D exchange experiments are performed to quantify the diffusion of Li between the two crystallographic phases.

4.2   Materials and methods

Microcrystalline TiO_2(anatase) (99%, particle size $2 - 20$ μm) were treated by chemical intercalation with n-butyllithium [56] to form the overall composition Li$_{0.12}$TiO$_2$ (for more information concerning the sample preparation see chapter 3 section 3.2). The results of chapter 3 have shown that for this composition ≈ 0.83 volume fraction is anatase (Li$_{0.01}$TiO$_2$) and ≈ 0.17 volume fraction exists of lithium titanate (Li$_{0.6}$TiO$_2$). The neutron diffraction line-broadening, chapter 5, gives an estimate of the domain sizes for the sample with overall composition Li$_{0.12}$TiO$_2$: ≈ 160 nm for anatase and ≈ 65 nm for lithium titanate.

^{7}Li MAS NMR spectra were recorded on a Chemagnetics 600 Infinity operating at 233.2 MHz. The MAS probe-head with 3.2 mm airtight zirconia rotors achieved spinning speeds up to 20.2 kHz in a dry nitrogen atmosphere. The 90° pulse length was 1.4 μs and, using a saturation recovery experiment, the T$_1$ relaxation time was determined to be well below 5 s for all temperatures. For the spectra a band width of 200 kHz was chosen. Chemical shifts were referenced to a 0.1 M LiCl aqueous solution.

2D-exchange NMR allows the detection of changes in the nuclear environment on a time scale roughly between the shortest of the spin-spin relaxation times, T_2, involved, and the specific spin-lattice or longitudinal relaxation time, T_1. The Larmor precessions

related to the different nuclear environments are probed before and after a time (mixing time) in which the nuclei can change from one environment to another. In a 2D spectrum, one dimension is related to the frequency spectrum before the mixing time and the other to the spectrum after the mixing time. In case no changes take place during the mixing time the normal one dimensional spectrum is found along the diagonal of the 2D spectrum. In case of diffusion from one environment to another during the mixing time, the diffused intensity will appear off the diagonal at the frequencies related to the environment before and after the mixing time. The principle of the applied r.f. pulse sequence, $\frac{\pi}{2}, t_1, -\frac{\pi}{2}, t_{mix}, \frac{\pi}{2}, acquisition(t_2)$, is further described in section 2.2.6.

1D-exchange NMR experiments were performed, in addition to the 2D-exchange NMR, to further quantify the diffusion. We made use of the significant difference in the line width i.e. the T_2 of the anatase and titanate phase for selecting the anatase phase. The specific pulse sequence applied was $\frac{\pi}{2}, \tau_{filter}, \pi, \tau_{filter}, -\frac{\pi}{2}, t_{mix}, \frac{\pi}{2}, acquisition$ (see section 2.2.6), with the appropriate phase cycles for cancellation of direct magnetization that may occur after T_1 relaxation. Using an appropriate τ_{filter} the intensity of the narrow anatase line was conserved while that of the broad titanate line vanishes due to the short T_2 of ^7Li in Li-titanate (T_2 filtering), i.e before t_{mix} starts the only magnetization present is in the anatase phase. Thus at time $2\tau_{filter}$ the signal with the largest T_2 (Li in anatase) largely refocusses, while τ_{filter} is chosen such that the resonance with the smallest T_2 (Li in lithium titanate) is completely unfocussed and therefore effectively demagnetized in the xy-plane. For the MAS speed used (> 19 kHz) $T_2 \approx 200$ μs (for all temperatures probed) for lithium titanate and 2 ms $< T_2 <$ 10 ms for Li in anatase, therefore τ_{filter} was chosen to be 1 ms. As a result, this experiment measures the diffusion of magnetized lithium in Li-anatase towards Li-titanate. The $\pi/2$ pulse at 2τ before t_{mix} aligns the magnetization of Li in anatase towards the z-axis. In the case that Li diffuses during t_{mix} from anatase towards lithium titanate its magnetization is lost during acquisition from the narrow anatase resonance and is gained by the titanate phase. Qualitatively it is expected that the diffusion of lithium into the titanate phase during t_{mix} causes the intensity of the narrow anatase line to decrease strongly as a function of t_{mix} while the broad titanate line becomes populated again. In this way a non equilibrium condition is created in terms of magnetized (or polarized) Li densities in anatase and titanate, while in terms of Li the system is in diffusive and thermodynamic equilibrium.

4.3   2D NMR exchange spectra

In figure 4.1, the central part of the ^7Li MAS NMR spectrum of the sample with overall composition $Li_{0.12}TiO_2$ is shown. The Li in anatase gives a sharp line in addition to the broad Li in lithium titanate signal. The exchange between the two phases is probed by the two-dimensional NMR experiments. The results of the 2D-NMR measurements are shown in figures 4.2, 4.3 and 4.4. ^7Li that remains in the same crystallographic phase has the same spectrum before and after t_{mix} and as a result the NMR intensity occurs at the diagonal positions. In contrast to that, the spectral intensity produced by ^7Li that is located in anatase at $t = 0$ and in titanate at $t = t_{mix}$ (or *vice versa*) will occur at the corresponding off-diagonal positions. The ridges in figure 4.3 is such off-diagonal
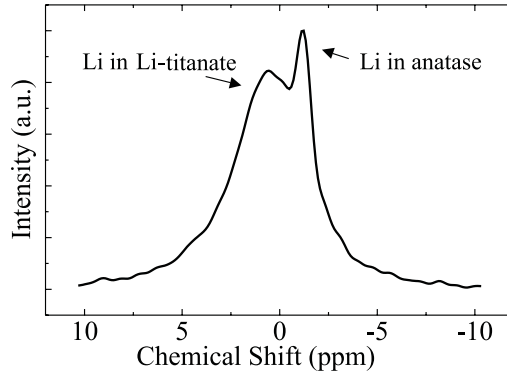
Figure 4.1: *Central part of the ^7Li magic angle spinning NMR spectrum of $Li_{0.12}TiO_2$ at 373K measured on a Chemagnetics 600. A spinning speed of 20 kHz and an r.f. field strength of $192kHz$ was used. Two phases are coexisting in thermal equilibrium: a Li-poor anatase phase with a composition of $Li_{0.01}TiO_2$ (narrow peak) and a Li-rich titanate phase with composition $Li_{0.6}TiO_2$ (broad peak), see chapter 3 [23].*

intensity, thus indicating exchanged of a large amount of Li between the two phases within the diffusion time, $t_{mix} = 50$ ms. The symmetry of the off-diagonal intensity with respect to the diagonal shows that the amount of Li diffusing from one phase to the other is balanced by the diffusion in the other sense as one should expect for a system in diffusive equilibrium. The short mixing time in figure 4.2, $t_{mix} = 50$ μs, does not result in significant diffusion between the phases and as a result no exchange is observed.   Because about 40% of the intensity in the sharp peak in figure 4.2 is exchanged for intensity in the ridges in figure 4.3, about 40% of the initial amount of ^{7}Li in anatase has moved towards the titanate phase after $t_{mix} = 50$ ms. In figure 4.4 a 2D-NMR spectrum taken at 148 K is displayed using a t_{mix} of 50 ms. At this temperature the Li motion between anatase and titanate is effectively frozen. Within the titanate phase there still appears to be diffusion as can be seen by comparing the width in the off-diagonal direction in figure 4.4 with that in figure 4.2. The off-diagonal broadening in figure 4.4 is due to exchange within lithium titanate, Li hopping from one crystallographic site to another (a much smaller length scale compared to inter-phase diffusion). This can be understood using the results from chapter 3 for the jump correlation time in lithium titanate at 148 K which is $\tau_c \approx 650$ μs. Being two orders of magnitude smaller than the mixing time, this means that Li is indeed diffusing within lithium titanate on a 50 ms timescale causing the "intra-titanate" exchange intensity. As fast MAS was applied, our cross-signal intensities in figure 4.3 cannot arise from spin diffusion due to the presence of dipolar couplings. Furthermore, figure 4.4 also proves that the off-diagonal ridges in figure 4.3 between the anatase and titanate phases are not due to spin-diffusion since the ridges are not present. This is because spin-diffusion is temperature independent, and ridges resulting from spin diffusion should then be the same in figure 4.3 and in figure 4.4. Therefore, its is concluded that the cross-signal intensities in figure 4.3 are caused by lithium diffusion between the anatase $Li_{0.01}TiO_2$ and $Li_{0.6}TiO_2$ lithium titanate phase and *vice versa*.

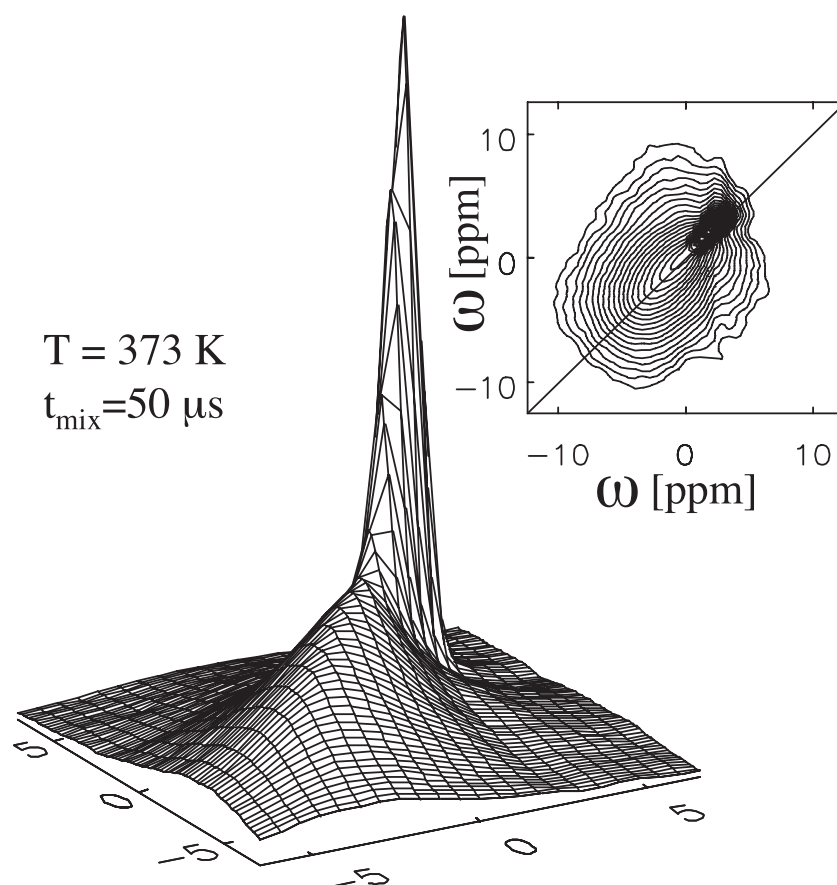Figure 4.2: *Two-dimensional exchange spectrum of $Li_{0.12}TiO_2$ at $T = 373$ K with mixing time $t_{mix} = 50$ μs. The contour plot (inset) is a projection of the three dimensional representation. On the diagonal both resonances can be recognized by comparison with figure 4.1, where Li in anatase is represented by the narrow line and Li in lithium titanate by the broad line. There is no cross-signal intensity visible indicating that the diffusion time of 50 μs is too short for cross-boundary lithium diffusion (diffusion between the two phases).*

4.4   1D NMR exchange spectra

4.4.1   Experiment

Faster one-dimensional experiments were performed to quantify the exchange as a function of t_{mix} and temperature. The experimental results in figure 4.5 display the decrease of magnetization, and thus the decrease of magnetized Li from the anatase phase, as a function of t_{mix}, for several temperatures. One should realize that this is not a net transport of Li but a net transport of magnetization, since the lithium transport from anatase to lithium titanate is compensated by the Li diffusion from lithium titanate, which is initially not magnetized, to anatase. Qualitatively one can understand the results in figure 4.5 as follows. The magnetized Li effectively diffuses from anatase towards titanate decreasing the integrated magnetization in the anatase, a process which becomes more
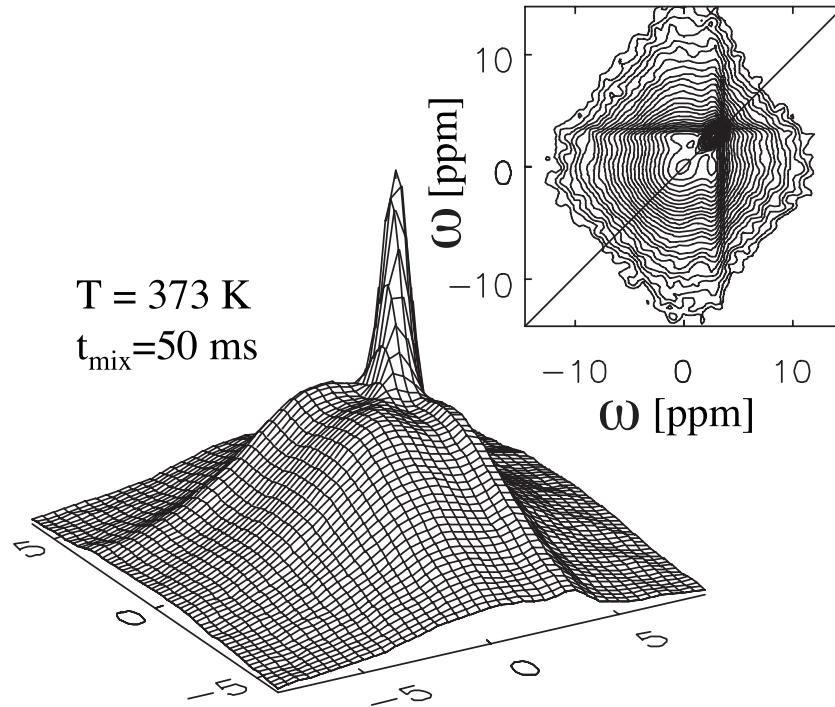
Figure 4.3:   *Two-dimensional exchange spectrum of $Li_{0.12}TiO_2$ at $T = 373$ K and $t_{mix} = 50$ ms. The contour plot (inset) is a projection of the three dimensional representation. Large ridges are visible covering the widths of the Li-in-titanate signal at the position of the Li-in-anatase signal. This cross-signal intensity is a direct measure of cross-boundary Li diffusion, the Li exchange between the two phases.*

pronounced at higher temperatures. In agreement with the absence of cross-intensity in figure 4.4, the Li exchange between the phases is frozen at 148 K. The lines drawn in figure 4.5 are the fits that result from the diffusion model described in the next section.

4.4.2   Fickian diffusion model

To quantify the diffusion between the two phases we construct a model to fit the de-magnetization of the anatase phase in figure 4.5. Although the Li diffusion between the two phases is microscopically balanced, the selective magnetization of Li in anatase by the pulse sequence used (see paragraph 4.2) gives rise to a non-equilibrium situation in terms of the diffusion of magnetization carried by the Li atoms. The Li atoms initially in the anatase phase are labelled. Therefore, we are interested in a non-stationary solution of Fick's law of diffusion:

$$\frac{\partial m(\boldsymbol{r},t)}{\partial t} = \boldsymbol{\nabla} \cdot \{D(\boldsymbol{r})\boldsymbol{\nabla}m(\boldsymbol{r},t)\}, \qquad (4.1)$$

where $m(\overrightarrow{\mathbf{r}},t)$ is the magnetisation of Li at position $\overrightarrow{\mathbf{r}}$ and time t, and D is the effective Li diffusivity. Here we follow the approach described by Spiess *et al.* [66]. First a 1-D solution obeying equation 4.1 is constructed using appropriate boundary conditions for the Li$_x$TiO$_2$ system. From the 1-D solution, a 2 or 3-D solution can be constructed.
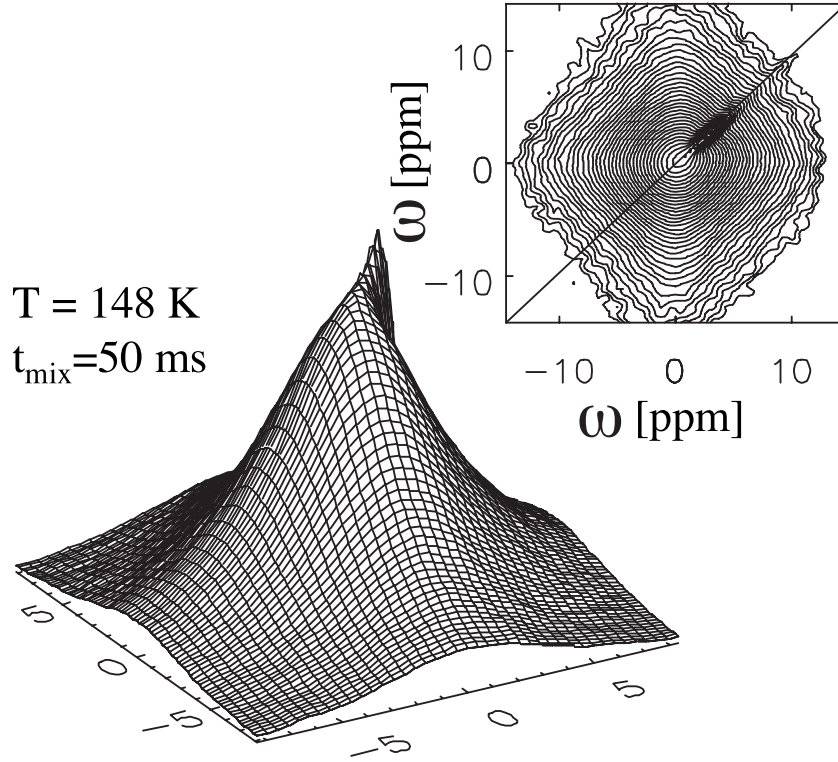
Figure 4.4: *Two-dimensional exchange spectrum of $Li_{0.12}TiO_2$ at $T = 148$ K and $t_{mix} = 50$ ms. The contour plot (inset) is a projection of the three dimensional representation. The cross-boundary lithium diffusion is absent due to freezing of Li motion between the anatase and lithium titanate phase. The rectangular off-diagonal shape of the Li-in-titanate peak shows that there is still diffusion within the titanate phase.*

Integrating this solution over the anatase phase results in the de-magnetization as a function of the mixing time. We first assume that D is isotropic and constant; i.e. $D(\overrightarrow{r}) = D$. This yields a one dimensional equation:

$$\frac{\partial m(y,t)}{\partial t} = D\frac{\partial^2 m(y,t)}{\partial y^2}. \tag{4.2}$$

The boundary conditions for equation 4.2 that are suited for the diffusion problem and yield a solvable equation, are as follows:

$$
\begin{aligned}
at \quad t=0 \quad m(y,t=0) &= m_0 \quad &for \ \ d \leq y \leq -d \\
&= 0 \quad &elsewhere \\
m(y \to \pm\infty, t) &= 0
\end{aligned}
\tag{4.3}
$$

where $2d$, is the length of the region centered around zero, representing the anatase region surrounded by the lithium titanate phase. The first two conditions state that the lithium magnetization in anatase, $-d \leq y \leq d$, equals m_0 at time zero, and that lithium in lithium titanate is initially not magnetized. The third condition prevents the integrated solution from diverging at $t = \infty$. We assume that the lithium titanate
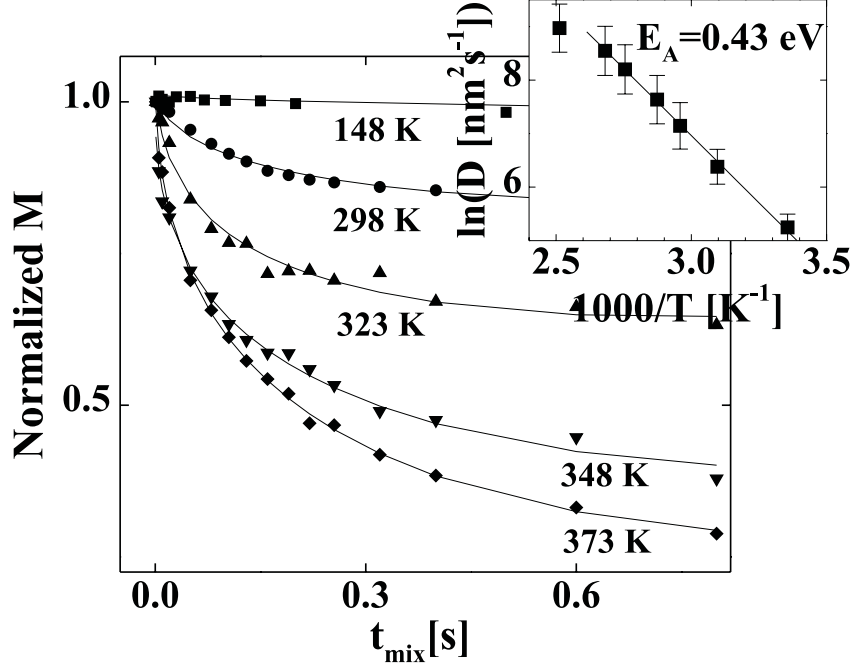
Figure 4.5: *Magnetization of Li in anatase as a function of the mixing time for a range of temperatures. The lines represent fits using the solution, equation 4.5, of the diffusion equation described in the text. Inset: Temperature dependence of the diffusion constant D. Fitting with an Arrhenius behavior the activation energy 0.43 ± 0.06 eV is found for the cross-boundary diffusion process.*

phase extends to infinity. This is not realistic, however, it can be expected to be a good approximation for relatively short times. The solution for equation 4.2 which obeys initial and boundary conditions in equation 4.3 is:

$$m(y, t) = \frac{1}{2}m_0 \left\{ \mathrm{erf}\left(\frac{d-y}{\sqrt{4Dt}}\right) + \mathrm{erf}\left(\frac{d+y}{\sqrt{4Dt}}\right) \right\}. \tag{4.4}$$

In the 1-D demagnetization experiment, the integrated amount of magnetized Li in the anatase phase is detected. Therefore, the solution, 4.4, should be integrated over the anatase region $[-d, d]$ to obtain the magnetization in anatase $M(t_{mix})$ as a function of mixing time. If a square or cube anatase phase domain shape is assumed, the approximate 2-D and 3-D solutions can be obtained simply by taking the Nth power (N=2,3) of the integrated solution. Thus, equation 4.4 integrated over the anatase region $[-d,d]$ yields:

$$M(t_{mix}) = \left\{ \frac{m_0}{2}\sqrt{4Dt_{mix}} \cdot \left[\mathrm{ierfc}\left(\frac{2d}{\sqrt{4Dt_{mix}}}\right) + \right. \right.$$
$$\left. \left. \mathrm{ierfc}\left(\frac{-2d}{\sqrt{4Dt_{mix}}}\right) - \frac{2}{\sqrt{\pi}} \right] \right\}^N, \tag{4.5}$$

where $\mathrm{ierfc}(x) = \frac{1}{\sqrt{\pi}}e^{-x^2} - x(1 - \mathrm{erf}(x))$ ($\mathrm{ierfc}(0) = \frac{1}{\sqrt{\pi}}$, $\mathrm{ierfc}(\infty) = 0$).

The size of the anatase domains was determined by neutron diffraction to be $\approx 160 \pm 20$ nm (chapter 5) for the sample used (in this case $2d = 160$ nm), $Li_{0.12}TiO_2$. For simplicity we assumed that the diffusion coefficient is independent of position, thus equal in both phases. However, previous NMR results, chapter 3 [23], showed that this is not true. The aim here is to determine the total diffusion coefficient for Li diffusing from one phase to the other irrespective what the rate limiting step is, diffusion in anatase, in lithium titanate, or through the phase boundary. Therefore, only one diffusion coefficient is taken account for. The fitted parameters are therefore, m_0 as normalization, the diffusion coefficient and the dimensionality.

Spiess *et al.* [66] add a term to equation 4.5 to correct for the finite dimensions of the domains. At $t = \infty$ the initially magnetized lithium in the anatase phase will be distributed over both phases which results in a finite density of magnetization in both phases. Due to the small lithium concentration in anatase ($Li_{\approx 0.01}TiO_2$) compared to in lithium titanate ($Li_{0.5-0.6}TiO_2$) this additional term can be ignored in the anatase phase. Moreover, in our experiment we only observe the initial part of the total decay.

The fit results are presented together with the data in figure 4.5. All the fits resulted in dimensionality 3 (except at 148 K which is essentially a straight line). The inset in figure 4.5 illustrates that the fitted diffusion coefficient as a function of temperature is thermally activated. The overall diffusion coefficient is $D_{RT} \approx 1.3 \pm 0.2 \times 10^{-12}$ cm^2 s^{-1} at room temperature, or in terms of Li flux through the phase boundaries $\approx 0.6 \times 10^{20}$ s^{-1}m^{-2}. An activation energy of 0.43 ± 0.06 eV can be deduced for the overall cross boundary diffusion.

4.5   Discussion

The 2D-NMR results give direct evidence that Li diffuses from anatase towards lithium titanate and *vice versa* and the 1D-NMR experiments allow quantification of this cross-boundary diffusion. However, can we relate the quantitative results for the diffusion in an equilibrium system to the non-equilibrium situation of (dis-)charging a battery? The diffusion coefficients measured by NMR in chapter 3 and in this chapter are all equilibrium self diffusion coefficients, since no (electro-)chemical potential gradient is applied and no collective behavior is probed. This might be confusing, since Fick's law is used to formulate the model that is fitted to the data. (Although there will be gradients in the, by magnetization, labelled Li, there are no actual applied gradients in the Li (electro-)chemical potential.) Generally, for jump diffusion the relation between chemical and self-diffusion (or tracer-diffusion) coefficient, D_C and D_S respectively, can be expressed as [67]:

$$\frac{D_C}{D_S} = \left(\frac{f_M}{f_t}\right) \left[c\frac{\partial \mu/\partial c}{kT} \right], \tag{4.6}$$

where f_M is the mobility correlation factor, taking into account correlated motion (=1 for uncorrelated motion), f_t is the self- or tracer-correlation factor which reduces the self diffusion at finite concentrations as a result of an enhanced probability for the reverse jump, c is the concentration, μ the chemical potential, k is Boltzmann's constant and T the temperature. The term between square brackets is known as the thermodynamic

factor. In the dilute limit self- and chemical diffusion coefficient are equal:

$$D_S(c \to 0) = D_C(c \to 0) = D_0 = \frac{l^2}{n\tau_0}, \tag{4.7}$$

where τ_0 is the mean residence time between jumps, l the jump length and n the number of nearest neighboring sites. D_0 is often referred to as the intrinsic diffusion coefficient. The self diffusion determined in the present NMR results equals:

$$D_S = f_t \frac{l^2}{4\tau_0}. \tag{4.8}$$

In order to approximate the corresponding value for the chemical diffusion coefficient we need to make a few assumptions. First we use the thermodynamic factor for a non-interacting lattice gas, which equals $1/(1-c)$ where c is the average occupation of the available sites. It is always true that the mobility correlation factor, f_M, is closer to unity than f_t which itself is generally close to unity, (0.6-0.8 for $c \to 1$). Hence, if we assume f_M and f_t to be unity and $c_{max} = 0.6$, the latter only valid for the titanate phase, the approximate upper limit for the chemical diffusion coefficient based on our self diffusion coefficient can be estimated to be $D_C \approx 3.2 \times 10^{-12}$ cm^{2}s^{-1} for a single crystal at room temperature.

This value is a factor of 10 larger than the macroscopic single crystal results $2.0 - 6.0 \times 10^{-13}$) cm^{2}s^{-1} obtained by Kavan *et al.* [6]. Because the value found in the present results is an upper limit, we can at least conclude that it is not in contradiction with the electrochemically found diffusion coefficient. An interesting observation is that the self-diffusion between anatase and lithium titanate, $D_S = 1.3 \times 10^{-12}$ cm^{2}s^{-1}, is smaller than the self-diffusion within the two phases, $D_S = 4.7 \times 10^{-12}$ cm^{2}s^{-1} for Li-anatase and $D_S = 1.3 \times 10^{-11}$ cm^{2}s^{-1} for Li-titanate. This indicates that the rate limiting step for the overall macroscopic diffusion is the cross-phase boundary diffusion, as was already suggested in chapter 3. In particulary the activation energy, 0.43 eV, for inter-phase diffusion supports this suggestion, because it is large compared to the activation energy for diffusion within the phases, 0.2 eV in anatase and 0.09 eV in lithium titanate [23]. This is in rather good agreement with the activation energy found for the macroscopic diffusion coefficient for single crystal TiO$_2$ $0.5 - 0.6$ eV [6] and also for poly-crystalline TiO$_2$ 0.5-0.56 eV [8].

It has been mentioned that the Li diffusion in anatase might be one dimensional, with the crystallographic b-axis as preferential direction [9]. However, the theoretical study of Lunell *et al.* [8], and the experiments of Kavan *et al.* [6] do not indicate this. Data fitting resulted in values of the dimensionality larger than 2.8, which indicates that the diffusion is three dimensional. Further, both line-broadening in neutron and X-ray diffraction indicated isotropic line-broadening by the domains. Thus, also with regard to the domain shape there is no reason to assume anisotropy in the Li diffusion.

Until now we discussed the nano-morphology of lithiated anatase as a static system. However, Li transport from one phase to the other might also be interpreted as movement of the phase boundary without effective Li transport. As a result of the difference in Li fraction between the phases Li transport is needed to allow the boundary to move. One can propose that the boundaries of the two phases will make a diffusive motion due to local fluctuations in the Li equilibrium flux between the two phases. This would lead to

diffusive motion of crystalline domains in an otherwise rigid solid-state system. Based on the equilibrium Li flux through the phase boundaries, $\approx 0.5 \times 10^{20}$ s^{-1}m^{-2}, a simple calculation leads to a value of 2.6 nm/s shift of the phase boundary if the Li flux from one phase to the other would not be compensated by a counter flux. This can be interpreted as a theoretical maximum phase boundary mobility based on the equilibrium inter-phase flux not compensated by a counter flux. Clearly, the cross-boundary flux and the phase boundary mobility are directly coupled, and from these experiments it is impossible to judge which is the rate limiting step.

Van de Krol *et al.* [7] proposed intercalation schemes for the (de)intercalation of thin film TiO$_2$ electrodes. During the intercalation the Li-rich lithium titanate phase forms at the electrode/electrolyte surface and the phase boundary moves deeper into the electrode. Two de-intercalation mechanisms were proposed. The first possibility is that the phase boundary moves back, the exact reverse of the intercalation process. The second possibility is that a second phase boundary moves into the electrode. This can be explained by removal of Li at the electrode/electrolyte surface, subsequently the original anatase (Li-poor phase) is formed at the surface which grows at the cost of the lithium titanate phase. Van de Krol suggested the second model to be correct since it can explain that the diffusion coefficient during extraction is larger than during insertion [6, 5]. The reason for this is that in the first mechanism the lithium titanate phase can be expected to determine both rate of insertion and extraction, whereas in the second mechanism the Li poor anatase phase determines the extraction rate explaining the difference between insertion and extraction. Because the rate of extraction is larger the second model suggests that the Li diffusion in anatase is larger, for instance due to the higher number of unoccupied octahedral sites compared to lithium titanate. However, previous NMR results show that the Li self-diffusion in lithium titanate is larger than that in anatase. Although it is inappropriate to compare the chemical diffusion coefficient measured by van de Krol with the self diffusion resulting from NMR, the NMR results [23] make clear that the octahedral site occupation is not decisive for diffusion coefficient in lithiated TiO$_2$. The results here offer an alternative explanation in terms of phase boundary. If the phase boundary mobility or cross-boundary diffusion is rate limiting, both overall insertion and extraction rate in the second model will be the same because effectively Li needs to cross the phase boundary. Therefore, in contrast to the suggestion by van de Krol, the most plausible mechanism is described by model 1. Based on the results presented here, we suggest the following intercalation mechanism during insertion and extraction. During insertion the phase boundary moves progressively into in the electrode, and the rate will be determined by the phase boundary movement or the cross-boundary lithium diffusion. During extraction the Li can leave the electrode without crossing or having to push the phase boundary until it reaches the lithium concentration at which Li-titanate converts to Li-anatase, thereby explaining the higher rate of extraction compared to insertion. We will continue this discussion in chapter 7.

4.6 Conclusions

In summary, lithium diffusion over length scales of $\approx$ 160 nm and time scales of $\approx$ 50 ms between the two crystallographic phases in lithiated anatase TiO$_2$ was observed.

Such diffusion maintains the thermal equilibrium between the two intermixed phases so that a battery can have a constant potential during (dis)charge. The inter-phase Li diffusion at room temperature determined from the NMR diffusion experiments is $D_{RT} \approx 1.3 \pm 0.2 \times 10^{-12}$ cm^2 s^{-1} with activation energy 0.43 ± 0.06 eV. The diffusion between the two phases appears to be less easy compared to the diffusion within the two phases, therefore it is expected that the inter-phase diffusion is rate limiting in the overall (or macroscopic) Li-ion diffusion in anatase TiO$_2$.

Chapter 5

Li-ion dynamics on multiple discrete intra-octahedron positions in lithiated anatase TiO$_2$

Abstract

Intercalation of Li in anatase TiO$_2$ results in a phase separation in a Li-poor and a Li-rich phase. The local lithium configuration in the coexisting crystallographic phases is resolved by detailed analysis of neutron diffraction data. In each of the phases two distinct positions within the octahedral interstices are found, with a temperature dependent occupancy. A combination of quasi-elastic neutron scattering and force field molecular dynamics simulations shows that Li is hopping on a picosecond time scale between the two sites within the octahedral interstices. The results also suggest a specific Li arrangement along the crystallographic a-direction, albeit without long range order.

5.1 Introduction

The physical and chemical properties of titanium dioxide offer an exciting spectrum of applications having the additional advantage of being bio-compatible, environmentally friendly and readily available. It is used as a white pigment in many products from toothpaste to wall paint. The crystallographic anatase form is of special interest due to its ability to store significant amounts of Li, which finds application as an anode in Li ion (nano-)battery materials [2]. The optical properties change upon Li insertion [48, 14], this electrochromic effect being the starting-point of displays and smart windows. The semiconductor properties also make it a suitable electrode in the conversion of light energy into electrical energy [1, 47].

In this chapter we focus on the Li-ion positions and dynamics of inserted lithium. Schematically the (electro-)chemical Li insertion can be written as TiO$_2$ + x Li$^+$ + x e$^-$ $\rightarrow$ Li$_x$TiO$_2$, where x is the mole fraction Li in TiO$_2$. The maximum Li insertion in anatase TiO$_2$ varies through the literature from $x = 0.5$ up to 1 depending on the

temperature and experimental technique. For chemical intercalation with n-butyllithium [56], which has a potential of 1 V vs. Li, $x = 0.6$-0.7 seems to be the most reliable value, while for electrochemical experiments $x = 0.5$ is consistently reported as the maximum insertion ratio. The (elastic) interaction force between intercalated Li-ions is expected to be attractive [57] and weak Ti-Ti interactions are formed [21], which results in a structural phase transition and separation into a Li rich and Li poor phase [58].

Cava *et al.* [4] already reported the structure of the lithium rich phase, here referred to as Li-titanate, and the Li position therein by using neutron diffraction. The structure for composition Li$_{0.5}$TiO$_2$ was indexed with space group Imma, number 74, whereas the space group of the original anatase was already known to be I41/amd number 141 [22]. The overall orthorhombic distortion of the atomic positions in the change from anatase to Li-titanate is small and leads to more regularly shaped TiO$_6$ octahedra in Li-titanate than in anatase. The change in symmetry is accompanied by a decrease of the unit cell along the *c*-axis and an increase along the *b*-axis. According to Cava *et al.* [4] the Li ions in the Li-titanate phase are randomly located in about half of the available interstitial octahedral 4e sites, which was also found in theoretical calculations [18, 19].

^{7}Li Nuclear Magnetic Resonance (NMR) results [23] confirmed the two phase equilibrium between a Li-ion poor phase with the original anatase structure (here referred to as lithiated anatase) and the Li-ion rich Li-titanate structure for overall compositions $x = 0.07 - 0.6$. The Li position in the original anatase structure is unknown, and can most likely only be found by a careful neutron diffraction study because of the small Li fraction: Li/Ti≈ 0.01 as was determined by NMR [23]. Furthermore, recent ^{7}Li NMR experiments [23, 24] which probe the local environment suggested that Li in the Li-titanate structure might not simply occupy one well-defined position in the TiO$_2$ lattice. This notion was based on the unexpectedly large homogeneous NMR line width of the ^{7}Li in Li-titanate, which might be related to Li residing in one site for a finite time $\approx 1/$line-width and then moving to another site with another NMR spectrum. So far, neutron diffraction has not been applied to determine the Li-ion positions in compositions Li/Ti > 0.5. This is especially relevant because of a new Li NMR resonance that was observed for Li/Ti ≥ 0.5 with an even larger line width than in Li-titanate Li$_{0.5}$TiO$_2$ [55, 23]. Although Luca *et al.* [55] suggested this new Li environment to be weakly coupled with conduction electrons, a new structural environment for lithium in Li-titanate for Li/Ti ≥ 0.5 can be also considered.

In this chapter the detailed Li position(s) and dynamics within the oxygen octahedra are studied in both coexisting phases: lithiated anatase and Li-titanate as well as in Li$_{0.6}$TiO$_2$. The chapter has two parts. In the first part neutron diffraction is applied as a function of temperature and composition to determine the Li-ion positions and the overall structure. Neutrons are preferred over X-rays, because of the sensitivity of neutrons for Li and the large region in reciprocal space that can be probed with neutrons (as many possible diffraction peaks are required). In the second part the local Li-ion dynamics is probed by temperature dependent quasi-elastic neutron scattering (QENS) in comparison with molecular dynamics simulations based on the COMPASS force-field [68].

5.2 Experimental section

5.2.1 Sample preparation

Microcrystalline TiO_2(anatase) (99%,particle size $2-20$ μm) was obtained from Janssen Chemica. Li_xTiO_2 samples were prepared by chemical intercalation of the TiO_2 powder with n-butyllithium [56] (1.6 M Aldrich). Four Li_xTiO_2 samples were prepared with overall compositions $x = 0.12$, 0.35, 0.5, 0.6. All sample preparations were carried out in an argon atmosphere glove box to prevent reaction of Li with air and moisture. After preparation, the samples were subjected to wet-chemical Inductively Coupled Plasma Spectroscopy (ICP) analysis to check the overall composition (ratio Li/Ti). These results confirmed that during preparation all the lithium reacted with the TiO_2 (anatase) thus yielding the overall compositions described. The exception is $x = 0.6$ which showed to be the maximum insertion ratio irrespective of the surplus amount of n-butyllithium.

5.2.2 Neutron Diffraction

Because subtle changes in both structure and in Li position(s) and site occupation(s) are expected, both high intensity and resolution in d-spacing are necessary. Although neutrons are very sensitive to Li compared to X-rays, the coherent cross section of Li is smaller than that of oxygen and titanium. In order to meet these high demands the neutron diffraction experiments were performed at GEM, the high intensity general purpose time-off-flight diffractometer at the ISIS pulsed neutron source [69] (Rutherford Appleton Laboratory, U.K.). GEM is equipped with more than 6000 detectors in 7 banks covering angles between approximately 159 degrees (back-scattering) and 18 degrees (forward scattering). For the present samples, significant intensity was obtained in the d-spacing range [0.2Å, 8Å]. All sample compositions ($x = 0$, 0.12, 0.35, 0.5, 0.6) were measured at 10 and 298 K, in addition composition $x = 0.35$ was also measured at T = 20, 40, 70, 110 K. Cylindrical vanadium air-tight sample cans were used for all the measurements and stable temperatures between 10 and 298 K were provided by a closed cycle refrigerator (CCR). Data were corrected for the scattering of the vanadium and the CCR with the Ariel software [70] and Rietveld refinement was performed using GSAS [71].

Besides the atomic and lattice parameters, the absorption, a line broadening parameter, the crystal phase fractions and background were also fitted. All the refinements resulted in residuals R_p and wR_p between 3 and 4 %, which can be considered as very satisfactory. In order to determine the Li-ion positions the (differences between) observed and calculated structure factors were obtained with GSAS [71] (Pawley method). Fourier density (difference) maps were obtained from the structure factors using the Fourier formalism implemented in the GFour package [72]. The Li-ion positions found were used as input for the Rietveld refinement, resulting in the fits described above.

5.2.3 Quasi Elastic Neutron Scattering

A pure Li-titanate sample, $Li_{0.6}TiO_2$, was loaded in a flat plate aluminium sample chamber, 2 mm sample thickness, under argon atmosphere and sealed with indium. The quasi-elastic neutron experiments were performed on IN6 at the Institute Laue-Langevin

(Grenoble, France). IN6 is a time focussing time-of-flight spectrometer designed for quasi-elastic and inelastic scattering with incident wavelengths in the range of 4 to 6 Å allowing the study of energy transfers between -3 meV and +200 meV. For our experiments $\lambda = 5.12$ Å was chosen resulting in an energy resolution of 100 μeV. The neutrons are detected by 337 elliptical ^{3}He detectors covering an angular range of $10° < 2\theta < 114°$. This results in a momentum transfer range of about 0.3 to 2 Å^{-1}. The experiments were performed at 2, 100, 150 and 250 K. The data were corrected for time independent background and the sample container scattering. The relative detector efficiency was determined from the vanadium reference spectra. Data were corrected using standard algorithms.

5.2.4   Force Field Molecular Dynamics Simulations

Force field methods assume that the system of atoms can be described in terms of classical mechanics. In certain circumstances force field methods are a good alternative for the more realistic quantum mechanical methods, these being computationally more expensive. The force field employed is the COMPASS [68] module in the CERIUS suite [73]. This *ab-initio* force-field has been parameterized and validated using condensed-phase properties in addition to various *ab-initio* and empirical data for molecules in isolation and recently also for inorganic materials. It enables accurate and simultaneous prediction of structural, conformational, vibrational, and thermo-physical properties. The models were geometrically relaxed, using the same COMPASS force field (this included the cell parameters). For the interaction between atoms, a semi-ionic model was used, in which, for non-bonding atoms the interaction energy is represented by an electrostatic term and the Lannard-Jones function, and for bonding atoms a Morse dispersion function in addition to the electrostatic term. For the MD simulations a step size of $1.0 \cdot 10^{-15}$ s was chosen [74], longer step sizes normally lead to unreliable calculations. Our calculation extended to $1.0 \cdot 10^{-9}$ s for models up to $3 \times 3 \times 2$ ($a \times b \times c$) unit cells of lithiated anatase TiO$_2$. For the static potential calculation the Li-ion trajectory was divided in 20 positions. At each position the geometry was optimized, using the same force field.

5.3   The structure of lithiated anatase TiO$_2$

5.3.1   Diffraction

In figure 5.1 a typical neutron diffraction spectrum is displayed. The reflections observed, for all compositions and temperatures, are in agreement with the space groups with which the two phases were previously indexed, I41/amd (number 141) for lithiated anatase and Imma (number 74) for Li-titanate. Where appropriate, the diffraction patterns were refined with a combination of the two phases. In figure 5.1, the difference between fitted and observed intensity is shown, indicating the very good fit quality; similar fit quality was found for all refined patterns.
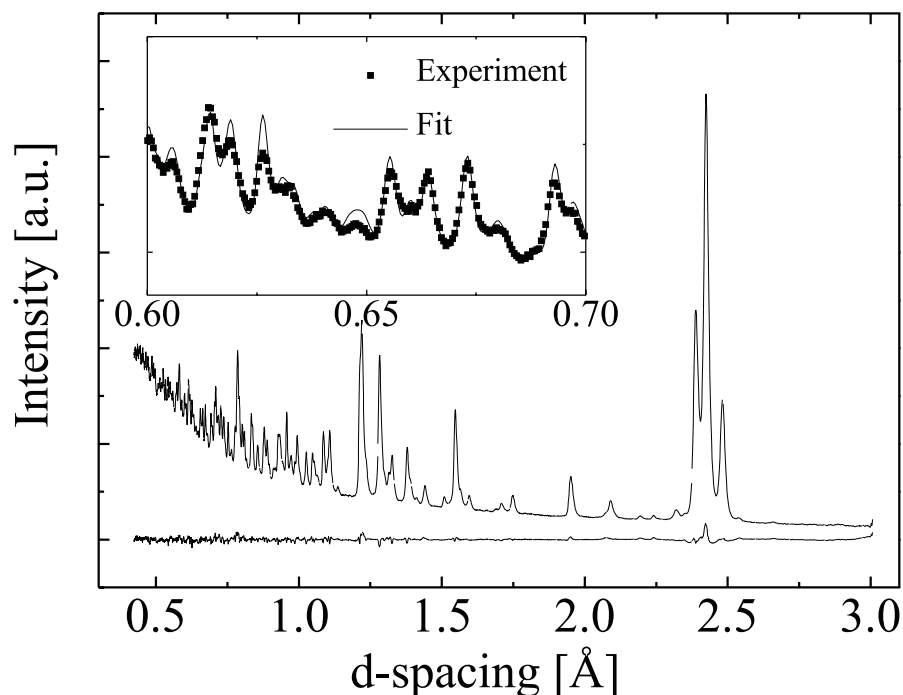
Figure 5.1: *Neutron diffraction TOF (2θ = 91.38 degree) pattern for Li$_{0.35}$TiO$_2$ including fit (line in the inset) and fit residual. In the inset a segment of the pattern at small d-spacing illustrates the large number of resolved diffraction peaks.*

5.3.2 Two-Phase Morphology

Progressive insertion of lithium in anatase TiO$_2$ leads to an increase of the Li-titanate phase and a decrease of the Li-anatase phase, see figure 5.2. In agreement with the XRD and NMR results presented in a previous publication [23] (chapter 3), only the ratio between the phases changes as more lithium is inserted. The linear behavior suggests that pure Li-titanate is formed at overall composition Li$_{x\approx0.55}$TiO$_2$.

As a function of temperature (T=10-298 K), the ratio between the two phases does not change significantly. The observed line broadening of the powder reflections is a clear indication of domain sizes of the two phases, these being significantly smaller than the initial TiO$_2$ powder particles, figure 5.2. The Li-rich Li-titanate and lithium poor Li-anatase phases coexist within one TiO$_2$ micron-sized particle [23, 24]. As the overall lithium content increases the Li-rich Li-titanate phase domains grow whereas the Li-poor phase domains become smaller.

5.3.3 Li-ion positions

In order to find the Li positions in both phases the structure factors from both the observed and calculated patterns were extracted. The model for the calculated structure factors contained the optimized Ti and O parameters, but did not include the unknown Li position(s). In this way the Fourier transform of the difference between the observed and
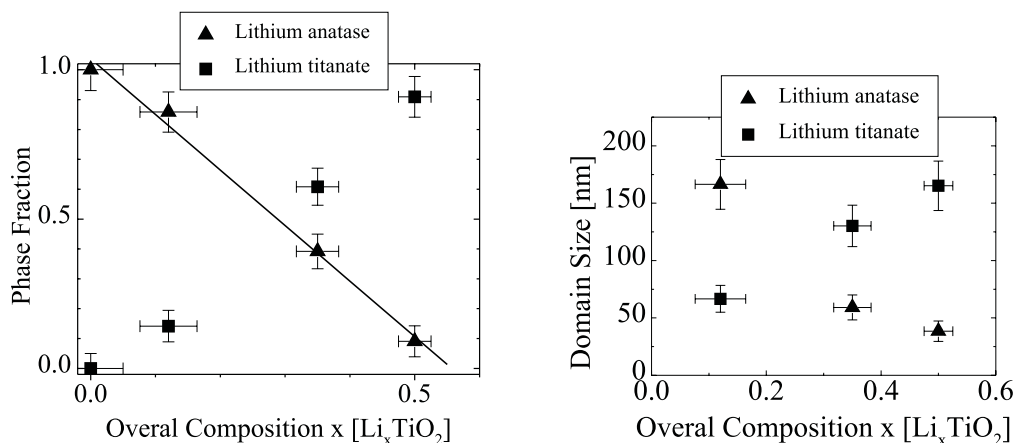
Figure 5.2: *Left: Phase fraction from Rietveld refinement versus composition x in Li$_x$TiO$_2$ at 10K. The line represents a linear fit to the Li-anatase phase fraction. Right: Estimates of the domain sizes versus composition x in Li$_x$TiO$_2$ at 10K based on line broadening.*

calculated structure factors indicates the Li position(s) within the lattice. Caution should be taken with the interpretation of density-difference plots because the one-dimensional (powder) data is, using the space group symmetry, transformed to three-dimensional data. The obvious way to confirm, and to further quantify, the Li position(s) found in the density-difference plot, is to use the resulting position(s) as start values in further refinement.

The density-difference plot for Li-anatase at 10 K in figure 5.3, is extracted from the diffraction pattern taken from the sample with the largest fraction Li-anatase; composition Li$_{0.12}$TiO$_2$. Because of the expected small Li fraction in anatase, approximately 0.01 [23], the measurement time for this composition was about 10 times longer than the other measurements. In figure 5.3 the oxygen and Ti positions are indicated and the two small spots between the oxygens is the intensity that is missing in the model because this does not contain the Li atoms. This indicates that the Li has two possible positions in the oxygen octahedra. Given the small distance between the two sites, 1.61 Å, it is unreasonable that the two positions are occupied simultaneously within one oxygen octahedron due to the repulsive Coulomb interactions between the Li-ions. The density-difference plot thus represents an average occupation over all the unit cells. To verify the Li density in figure 5.3, which can be represented by a single crystallographic position in the tetragonal I41/amd space group, they were included in the Rietveld refinement. Although the Li fraction is very small, the refinement was stable and the fit residue became significantly smaller upon adding the two Li positions. The fit results are included in table 5.1. For comparison, the fitted parameters of pure anatase are also listed. The Li/Ti ratio is about 0.026, which is larger, but of the same order as 0.01, found with quantitative NMR experiments [23]. Comparison of the unit cell dimensions of pure anatase and the Li$_{x\approx0.01}$TiO$_2$ (table 5.1) phase suggests that even the small Li-ion fraction causes a subtle distortion of the anatase lattice: a and b increase whereas c decreases. This is similar, though rather less than the distortion of the lithium rich
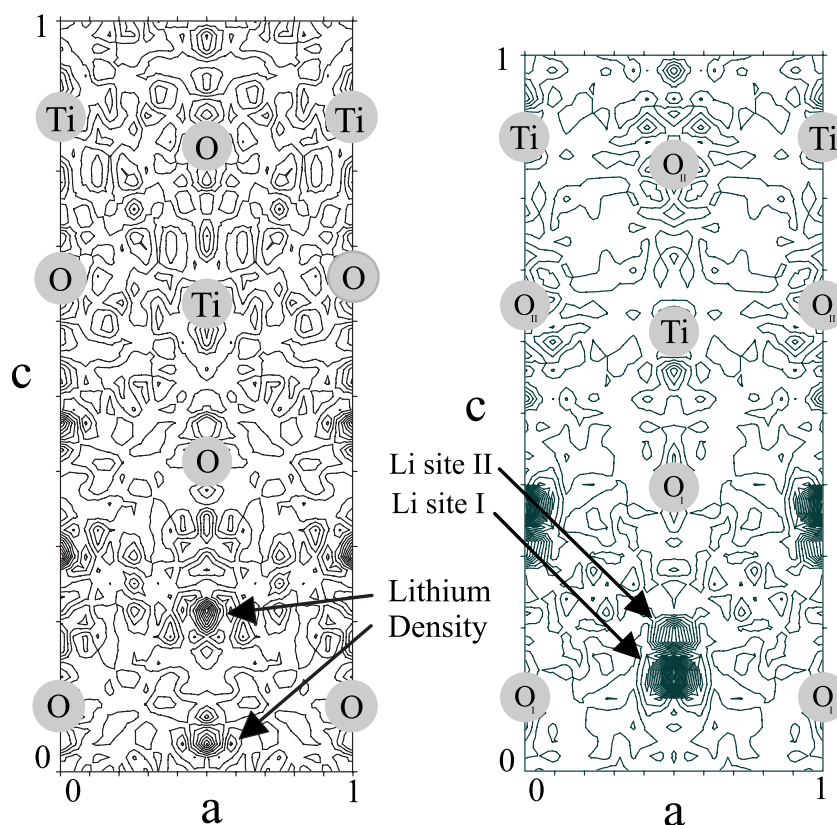
Figure 5.3: *Left: Fourier scattering length density-difference plot of the Li-anatase phase in the $Li_{0.12}TiO_2$ sample indicating possible Li positions at 10 K. Right: Fourier scattering length density-difference plot of the Li-titanate phase in the $Li_{0.5}TiO_2$ sample indicating possible Li positions at 10K. For both plots the density displayed is a section of the unit cell at y=0.25 b.*

Li-titanate phase (see below). Unfortunately, due to the small lithium fraction, it was not possible to derive composition and temperature dependent parameters.

The density-difference plot of the Li-titanate phase resulting from the Li$_{0.5}$TiO$_2$ sample at 10 K in figure 5.3 indicates two possible Li positions very close to each other compared to Li in Li-anatase in the same figure. Again, Rietveld refinements confirm the two positions found in the density-difference plots, the results of which are tabulated for T=10 K in table 5.1. Also in Li-titanate, Li does not occupy more than one position within one oxygen octahedron because of repulsive Coulomb interactions between the Li ions. The difference in density between the two Li sites in figure 5.3 illustrates that the two Li positions are not occupied evenly on average over the crystal. The positions are not symmetrically equivalent as in Li-anatase and were fitted separately. The fit results are presented in table 5.1.

The discrepancy between the present results and the neutron diffraction results of Cava *et al.* [4] is subtle and concerns the occurrence of the two lithium positions in Li-titanate. The Ti and O positions are identical, within the experimental accuracy. Cava *et al.* found one Li-ion site, z-coordinate 0.343 c, located between the two sites found in the present work. Assuming there is only one possible position, refinement of our data results

Table 5.1: *Unit-cell parameters (Å) and atom positions of anatase, Li-anatase, Li-titanate and Li$_{0.6}$TiO$_2$ at 10 K.*

|	Wyckoff symbol	x,y,z-coord. [0-1]a,b,c	frac. [0-1]
anatase TiO$_2$ (I 41/amd*)			
Ti	4a	0, 0.75, 0.1250	1
O	8e	0, 0.75, 0.3333	1
Lattice	a=3.7867		
parameters	b=3.7867		
	c=9.5149		
Li-anatase (I 41/amd*)			
Ti	4a	0, 0.75, 0.1250	1
O	8e	0, 0.75, 0.3334	1
Li	8e	0, 0.75, 0.5401	0.013
Lattice	a=3.7919		
parameters	b=3.7919		
	c=9.4973		
Li-titanate (Imma)			
Ti	4e	0, 0.25, 0.8871	1
O$_I$	4e	0, 0.25, 0.1037	1
O$_{II}$	4e	0, 0.25, 0.6518	1
Li$_I$	4e	0, 0.25, 0.3651	0.32
Li$_{II}$	4e	0, 0.25, 0.2881	0.19
Lattice	a=3.8186		
parameters	b=4.0842		
	c=9.0656		
Li$_{0.6}$TiO$_2$ T = 10K			
Ti	4e	0, 0.25, 0.8869	1
O$_I$	4e	0, 0.25, 0.1041	1
O$_{II}$	4e	0, 0.25, 0.6525	1
Li$_I$	4e	0, 0.25, 0.3569	0.38
Li$_{II}$	4e	0, 0.25, 0.2888	0.21
Lattice	a=3.8141		
parameters	b=4.0771		
	c=9.0427		

* Origin choice 2
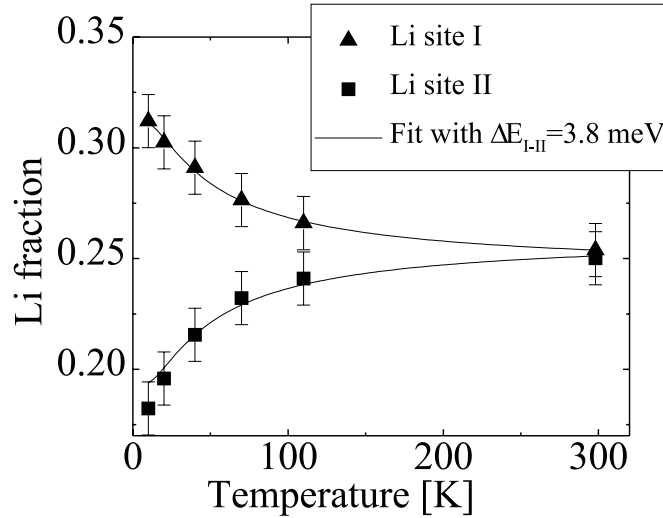
Figure 5.4: *Li fraction resulting from refinement from both Li sites in the Li-titanate phase (Li$_{0.52}$TiO$_2$) as a function of temperature (sample composition Li$_{0.35}$TiO$_2$). The line is a best fit with a Boltzmann distribution of Li between the sites.*

in the same Li position found by Cava *et al.* In particular at room temperature a good fit with one Li-ion position is obtained, but with a substantial anisotropic temperature factor in the c-direction. However, the two positions found with the density-difference analysis improved the fit quality significantly, even at room temperature, and thus gives a better description of the system. Further, this is in agreement with our dynamical measurements and MD simulations.

The composition of Li-titanate $x \approx 0.5$ might suggest a possible ordering of Li or/and Ti^{3+}-Ti^{4+} as already proposed by Murphy *et al* [22]. If such an ordering implies a multiple unit cell, one expects super structure reflections corresponding to the larger unit cell. Such an ordering can be rejected since no extra peaks were observed at high d-spacings in any of the spectra. Ordering within the Li-titanate Imma unit cell would lead to reduction in symmetry as the Li and/or Ti positions (all equivalent in Imma) will become non-equivalent (Imm2 space group). Our results corroborate those of Cava *et al.* in that the present results do not indicate such an ordering because the fit quality did not improve significantly within the Imm2 space group.

The considerable Li fraction in Li-titanate, enables the study of the Li fractional site occupation as a function of temperature and composition. The Li fraction versus temperature of both Li sites, *I* and *II*, is displayed in figure 5.4. The fact that the Li fractions become equal at high temperatures, whereas they were different at lower temperatures, can be interpreted as the result of a difference in energy between Li residing in site *I* and in site *II*, hence a preference for Li to reside at *I*. Fitting the site occupancy assuming a Boltzmann distribution, as shown in figure 5.4, indicates that the energy of a lithium ion in site *I* is 3.8 meV lower compared to site *II*. The total Li/Ti fraction is about 0.52 averaged over all temperatures and constant with temperature. This is somewhat smaller than, but not in contradiction with the value suggested by the quantitative NMR results ($x = 0.5-0.6$) [23]. The distance between site *I* and *II* in the c-direction becomes

marginally smaller with increasing temperature.

The Li concentration in the Li-titanate phase can be increased up to ≈ 0.6 Li/Ti in case of chemical lithiation with butyllithium. With ^{7}Li NMR a second Li environment in the Li-titanate structure was observed [55, 23]. Density-difference analysis and subsequent Rietveld refinement resulted in the same two Li positions and a slightly distorted structure compared to the original Li-titanate. The refined parameters are listed in table 5.1. Therefore the new ^{7}Li NMR resonance that appears for lithium insertion fraction Li/Ti ≥ 0.5 [55, 23] can not be explained by an additional Li-ion structural environment, which in addition to the arguments of Luca *et al.*[55], indicates an electronic origin of the additional Li-ion environment in compositions with Li/Ti ≥ 0.5. The refined Li fraction is increased from 0.52 in Li-titanate to 0.59 in $Li_{0.6}$-titanate. Also in $Li_{0.6}$-titanate there is no indication for non-equivalent Li_I, Li_{II} or Ti atoms within the Imma unit cell or ordering leading to a superstructure.

The changes of unit cell dimensions of the anatase structure upon lithiation towards Li-titanate are in agreement with those reported previously [4]. The unit cell volume increases about 3%. In Li-titanate the a and b-axis become different in length about 7%, mainly increasing in the b-direction, and the unit cell decreases about 5% in the c-direction, c.f. table 5.1. Upon intercalation the Li-electron density fills the states at the bottom of the conduction band that are Ti-O antibonding and Ti-Ti bonding [63]. As a consequence, the structure is deformed in such a way that Ti-O distances are elongated and Ti-Ti distances are shortened (see table 5.2). Occupation of these bonding bands with the charge causes two of the four smallest Ti-Ti distances to decrease upon lithiation and form zig-zag chains of Ti atoms in the b-direction. This causes the reduction in symmetry going from the anatase structure (I 41/amd) to the Li-titanate structure (Imma) and the change of the a and b unit cell lengths in Li-titanate. Increasing the lithium fraction from Li-titanate to $Li_{0.6}$-titanate, can be expected to lead to progressive filling of the Ti-Ti $3d_{yz}$ bonding bands resulting in a very small decrease, from 2.8914 Å to 2.8878 Å, of these Ti-Ti "chain" bond lengths.

Two equivalent Li-ion positions are found in Li-anatase, symmetrically located with respect to the middle of the oxygen octahedron. In Li-titanate, two possible lithium positions are also found within one oxygen octahedron. However, the positions are separated (in the z-direction) by 0.7 Å compared to 1.61 Å in Li-anatase. This is most likely the result of the deformation of the oxygen octahedron in Li-titanate which becomes smaller in c-direction with the four equatorial oxygens (in the ab-plane) more in plane (see table 5.2).

Inspection of figure 5.5 and of the Li-O distances in Li-anatase and in Li-titanate, table 5.2, indicates that lithium in anatase and lithium site II in Li-titanate are effectively five-fold coordinated rather than six-fold coordinated as suggested by the octahedral coordination. Lithium at site I in Li-titanate is located more towards the center of the oxygen octahedron, and its octahedral oxygen coordination is more regular compared to site II.

The relative preference for lithium to reside in site I rather than site II in Li-titanate results from the 3.8 meV energy difference between the sites. This may be due to the distance between two nearest neighboring Li_{II} sites (in the a-direction) being short compared to Li_I neighboring Li_{II} and to two neighboring Li_I sites. Hence, the latter will suffer less from Li-Li Coulomb repulsion. This qualitatively explains the difference

Table 5.2: *Interatomic distances (Å) and the coordination number number (in parentheses) in the structures anatase TiO_2 (I 41/amd, RT), Li-anatase (I 41/amd, 10 K), Li-titanate (Imma, 10 K) and $Li_{0.6}$-titanate (Imma, 10 K). The subscripts eq and ax refer to the oxygen coordination in the ab-plane and in c-direction, respectively. Li_{av} refers to the average position of Li in the oxygen octahedron, which is located approximately midway between site I and II*

Structure	Li-anatase	Li-titanate	$Li_{0.6}$-titanate
Ti-Ti	3.0384 (4)	3.1344 (2)	3.1252 (2)
Ti-Ti		2.8914 (2)	2.8878 (2)
Ti-O_{eq}	1.9367 (4)	1.9416 (2)	1.9400 (2)
Ti-O_{eq}		2.0438 (2)	2.0402 (2)
Ti-O_{ax}	1.9792 (2)	1.9636 (1)	1.9641 (2)
Ti-O_{ax}		2.1331 (1)	2.1196 (2)
Li_I-O_{eq}	1.9400 (2)	2.0487 (2)	2.0403 (2)
Li_I-O_{eq}	2.2445 (2)	1.9301 (2)	1.9394 (2)
Li_I-O_{ax}	1.9631 (1)	2.3697 (1)	2.2860 (1)
Li_I-O_{ax}	3.5757 (1)	2.5991 (1)	2.6730 (1)
Li_{II}-O_{eq}		2.1135 (2)	2.1389 (2)
Li_{II}-O_{eq}		2.1465 (2)	2.1065 (2)
Li_{II}-O_{ax}		1.6717 (1)	1.6702 (1)
Li_{II}-O_{ax}		3.2972 (1)	3.2888 (1)
Li_{av}-Li_{av}	3.0383 (4)	2.5473 (2)	2.5428 (2)
Li_{av}-Li_{av}		3.5033 (2)	3.4954 (2)

in occupancy.

Each octahedral interstice has four nearest neighboring interstices which are all at the same distance in the anatase structure but split in two pairs of distances in Li-titanate, the shorter being in the a-direction. As a result, the Li-Li distances between Li in one interstice and another (either Li_I-Li_I, Li_I-Li_{II} or Li_{II}-Li_{II}) are smaller in the a-direction. The average Li-Li inter-octahedral distance is ≈ 2.5 Å in the a-direction and ≈ 3.5 Å in the b-direction. As with the Ti-Ti distances, we can consider Li-Li zig-zag chains of sites in the a-direction (the Ti-Ti chains are in the b-direction). Based on the difference between the distance between Li-ion sites, we expect that the number of Li neighbors will be minimal on sites in the chain direction due to repulsive Coulomb interactions. This will be less important for the nearest Li neighbor located in sites in another chain. At Li occupation 0.5 one might expect that average each Li in the octahedral interstice is neighbored in the chain direction by two empty sites to
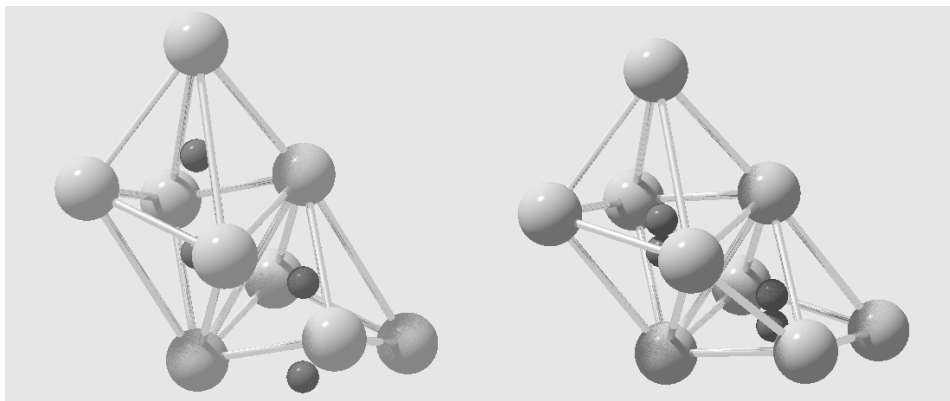
Figure 5.5: *Left: Two neighboring oxygen octahedra in Li-anatase (space group I/41amd) with the available Li ion sites. Right: in Li-titanate (space group Imma). In the left (right) octahedron the top (bottom) Li-ion site represents the position referred to as site I*

minimize the Coulomb interaction. This proposed site occupation model explains both the preference for the ≈ 0.5 lithium occupation in Li-titanate of the available positions and the difficulty to increase it, as this implies unfavorable in-chain nearest neighbors. The Li ordering in the chain direction will be obscured by the absence of ordering between the Li-ion positions in different chains and hence is unlikely to be observed in diffraction, as is the case in the present results. We anticipate that the dynamic behavior of the lithium ions, hopping between octahedra [23] (chapter 3), will result in increased disorder.

5.4   Intra-octahedron Li-ion mobility

In order to study the Li-ion dynamics within the oxygen octahedron in Li-titanate, in-coherent quasi-elastic neutron scattering experiments were performed (the Li fraction in Li-anatase is too small to conduct such a study). Quasi-elastic incoherent scattering measures the correlation function for a given particle, in this case Li, to be in a certain volume at a certain time, if it were in that volume at time zero. The energy transfer determines the time scale of the particle dynamics and the momentum transfer is inversely related to the dimension in which the motion takes place. The incoherent scattering length of Li is relatively small, compared to hydrogen for which many successful quasi-elastic studies have been reported [32], but TiO$_2$ as compound has almost negligible incoherent scattering. Consequently, the incoherent signal in Li$_x$TiO$_2$ mainly arises from Li. The experimental quasi-elastic neutron scattering results will be compared to molecular dynamic force field simulations of the Li-ion movement based on the structural parameters determined by neutron diffraction in the previous section.

5.4.1   Quasi-elastic neutron scattering results

The neutron scattering spectra were measured at different momentum transfers, Q. An example at one Q value is shown in figure 5.6. A fit was made over all Q-values using
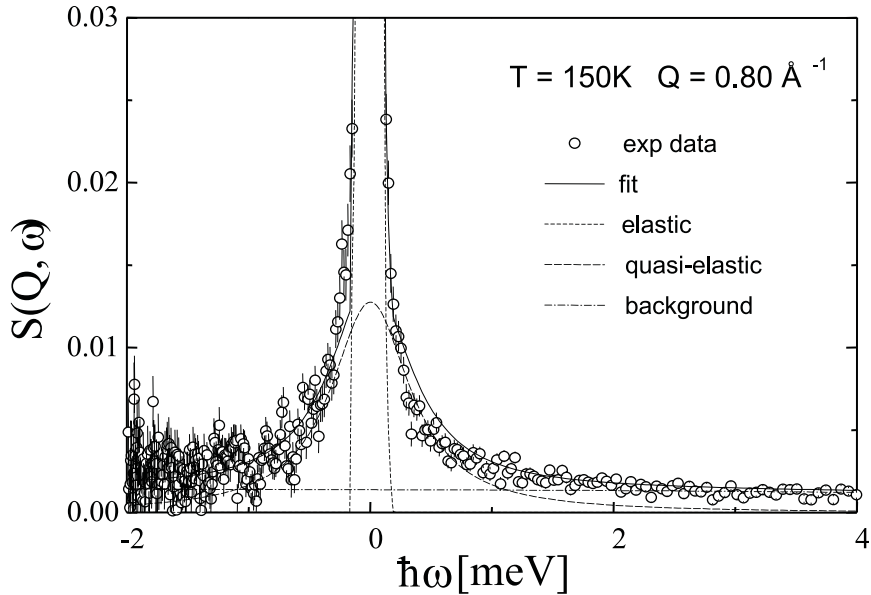
Figure 5.6: *Quasi-elastic neutron spectrum of $Li_{0.6}TiO_2$ at 150 K for momentum transfer Q=0.8 Å, one of the 8 Q values measured. The fitted elastic and quasi-elastic contribution are also shown.*

a single Lorentzian-function and a δ-function centered at zero energy transfer. The resulting functions were convoluted with the measured resolution functions. In figure 5.7 the full width half maximum $\Gamma(Q)$ (FWHM) of the quasi-elastic component is displayed as a function of Q, for different temperatures. For random diffusion of Li-ions the line width, $\Gamma(Q)$, would increase with Q^2 [75]. In contrast, $\Gamma(Q)$ in the present work is constant with Q and increases with temperature. The QENS experiments therefore indicate a single timescale of Li-ion motion that is thermally activated. The Lorentz shaped broadening indicates a relaxation of the self-correlation function of the form e^{-t/τ_c} where $\tau_c = 2/\Gamma$ is the correlation time, which for jump processes can be associated with the mean average time Li resides at a certain position. At $T = 2$ K the line width equals that of the resolution function (100 μeV) corresponding to 13.2 ps, this means $\tau_c > 13.2$ ps. If we assume the time scale of the Li mobility to be thermally activated, the correlation time will obey an Arrhenius law, $\tau_c = \tau_\infty \exp(E_A/k_B T)$, where E_A is the activation energy of the jump process and $1/\tau_\infty$ the attempt frequency. The result for the data in figure 5.7 is: $E_A = 5.7 \pm 0.3$ meV (66.7 K) and $\tau_\infty = 1.28 \pm 0.2$ ps.

The elastic incoherent structure factor (EISF) in figure 5.8, the normalized contribution of the elastic component, decreases with temperature and slightly decreases with increasing momentum transfer. Apparently Li-ions in Li-titanate effectively remain within the length scale, 3.5 Å, associated with the maximum impulse transfer Q.

5.4.2 Molecular dynamics simulations

Various models were subject of the MD simulations differing in Li-fraction and distribution, a few for which we explicitly report the results here. In figure 5.9 a schematic view
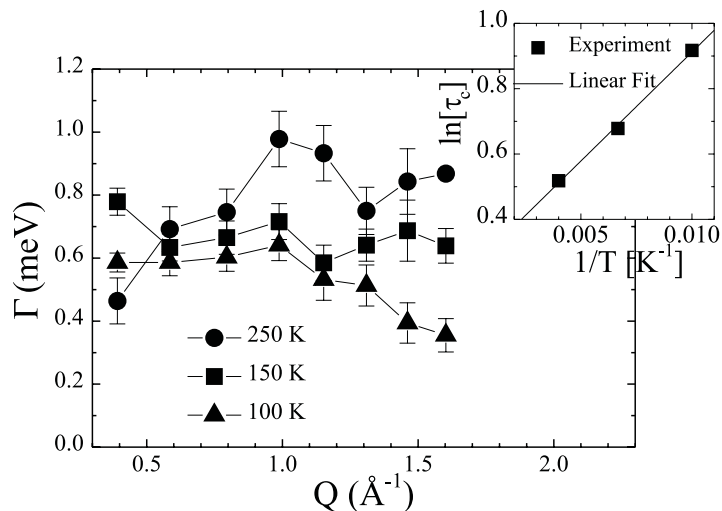
Figure 5.7: *Quasi-elastic line width as a function of momentum transfer for different temperatures. The inset represents an Arrhenius plot for the correlation time associated with the quasi-elastic line width, see text.*
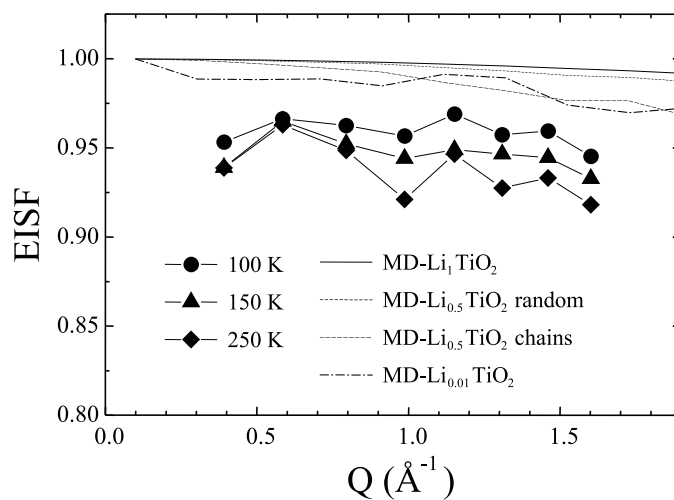

Figure 5.8: *The elastic incoherent structure factor (EISF) as a function of momentum transfer for different temperatures. Also included are calculated EISF curves based on the Molecular Dynamics calculations presented below.*

of models 1-3 is presented including the lattice energy for the models with composition $Li_{0.5}TiO_2$. In model 1 all the octahedral sites are occupied by lithium, either site I or II. In model 2 lithium is initially randomly distributed over half of the octahedral sites (site I or II within the oxygen octahedron). Model 3 represents again Li-titanate where in this case the octahedral interstices in the -a and +a direction (the chain direction representing the nearest neighboring Li-ion positions) are occupied every second position. Thus each Li-ion is neighbored by unoccupied Li sites in the -a and +a direction and as for model 2, half of the octahedral interstices is occupied by a lithium atom. Li randomly occupies site I or II within the octahedron. This model for the Li-positions ordered in the a-direction was proposed in section 5.3 based on minimizing the repulsive coulomb interactions between the Li-ions. Model 4 (not shown in figure 5.9) contains only one Li atom, which for this model size results in $Li_{0.01}TiO_2$. This resembles Li in anatase rather than Li in Li-titanate. It is interesting to note that although the single Li-ion was placed in the titanate lattice, relaxation of the structure including the cell parameters, resulted in the tetragonal anatase structure (the a and b lattice parameters become equal). Before the MD simulations were performed, all models were fully relaxed by minimizing the energy. Comparing the lattice energy between model 2 and 3, for Li-titanate, illustrates what was intuitively argued previously. The absence of nearest Li-ion neighbors in the a-direction (model 3, referred to as a Li-ion ordering in the a-direction) is energetically favorable compared to a random Li-ion occupation of the available sites (model 2) where a number of Li-ions have nearest Li-ion neighbors in the a-direction, see section 5.3.

In figure 5.10 the Li trajectory resulting from the dynamics calculation at 250 K is plotted for three different models in the ac-plane, the same plane as the density-difference plots presented in figure 5.3. For model 2 the expected two sites can hardly be recognized in the cigar shaped density, similar results were obtained for model 1. In contrast, in model 3 also representing Li-titanate the two sites I and II are recognized. Vibrations within the site and hopping between the sites can be distinguished. The distance between the sites is approximately 0.8 Å, in good agreement with the experimental value of 0.7 Å (see section 5.3).

Model 4 should be compared with the lithium poor Li-anatase phase. In agreement with the experimental result the two Li-ion positions within the oxygen octahedron are separated by a larger distance compared to lithium in Li-titanate; calculated is 1.5 Å, see figure 5.10, and experimentally found is 1.61 Å (see table 5.1).

We wish to compare the timescale of the intra-octahedron hops calculated for Li-titanate with the experimental QENS data. For that we use the results of model 3 which seems to represent the Li-titanate better than the other presented models. The timescales of the local Li vibrational motion and the intra-octahedron hops are well separated in the lithium mobility power-spectrum resulting from the MD calculations, figure 5.11. During the calculations, which covered 1.0 ns, the intra-octahedron hops occur at lower frequencies. As a result the characteristic frequency for this process has a relatively weak signal compared the local Li vibrations. From the power spectrum an average jump frequency of the Li-ions, equal to the inverse of the correlation or mean residence time for a Li-ion to reside at a given site, can be deduced. The correlation time at 250 K is approximately 3 ps (mean value of the envelope) for the intra-octahedron hops.

For lithium in the anatase structure, model 4, the power-spectrum (not shown) leads
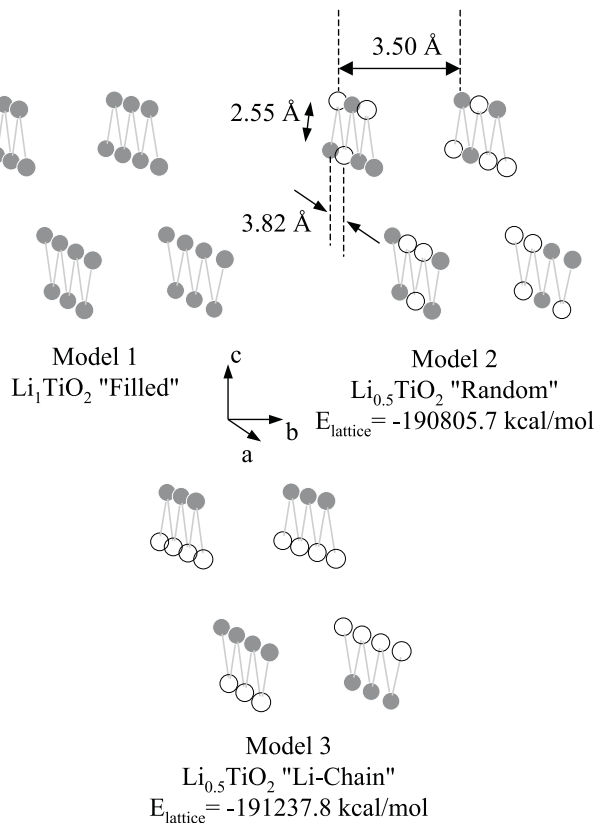
Figure 5.9: *Schematic view of the Li-ion octahedral occupations in model 1-3, a dark sphere represents an occupied lithium site. For simplicity the two Li-ion sites, Li_I and Li_{II}, are represented as one site.*

to smaller frequencies for the intra-octahedron hops and in a correlation time of approximately 20 ps. This is not surprising because the two sites in the oxygen octahedron are further apart, and probably separated by a higher potential barrier.

The elastic incoherent structure factor (EISF) can be calculated from MD trajectories, the results being illustrated in figure 5.8 for the four different models. The limited Q-range of the experiments and the small amplitude of the Li-ion dynamics does not allow any discrimination between the different models for the EISF.

Within the best proposed model for Li-titanate (model 3) it is interesting to calculate the Li-ion potential along the c-axis, because one would expect to find two minima in energy at the two Li-ion sites within the oxygen octahedron. During these calculations the unit cell dimensions and the position of the Li ion under investigation, were fixed, whereas the other atoms were allowed to relax. The results are plotted in figure 5.12 both for model 3, representing Li-titanate, and for model 4 representing Li-anatase. This calculation confirms the two Li positions within the oxygen octahedron found experimentally (figure 5.3). The corresponding energy barriers between the two sites are 0.26 eV for Li-anatase (model 4) and 0.026 eV for Li-titanate (model 3). In Li-anatase the statically calculated separation between the two lithium ions is 1.3 Å and for Li-titanate the distance between site I and II is 0.6 Å in reasonable agreement with the neutron

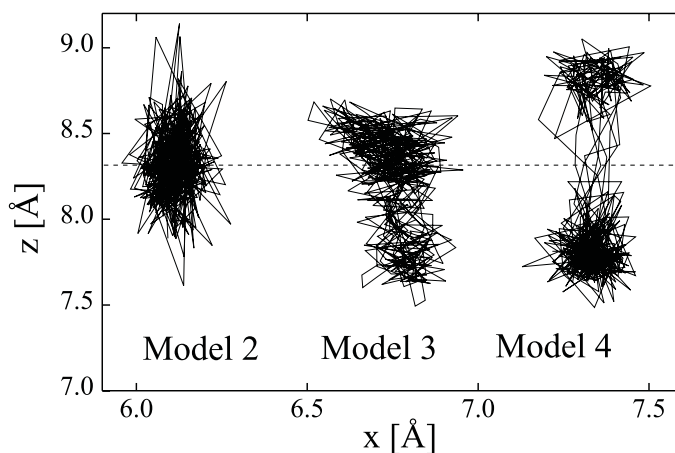Figure 5.10: *The lithium trajectory, projected on the ac-plane which intersects with the two lithium sites, calculated with the MD simulations for models 2, 3 and 4 (see text). The dashed line represents the mid-plane of the four oxygen atoms in the ab-plane.*
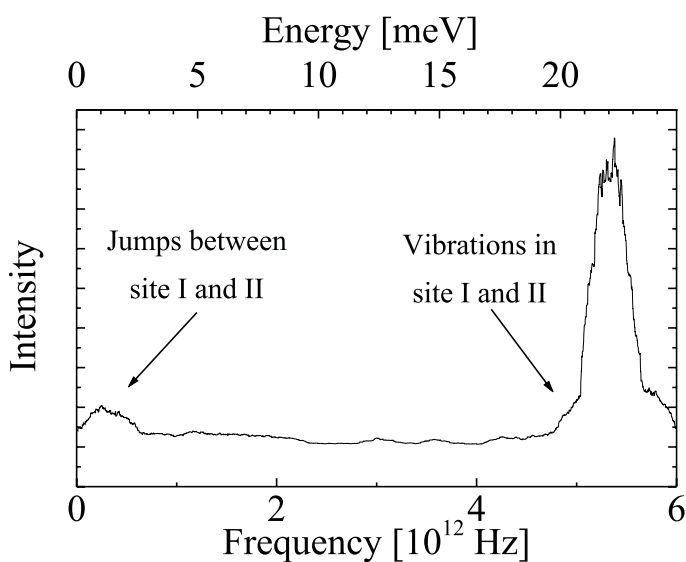

Figure 5.11: *Lithium mobility power-spectrum resulting from the MD simulations of model 3 representing lithium in Li-titanate (see text).*
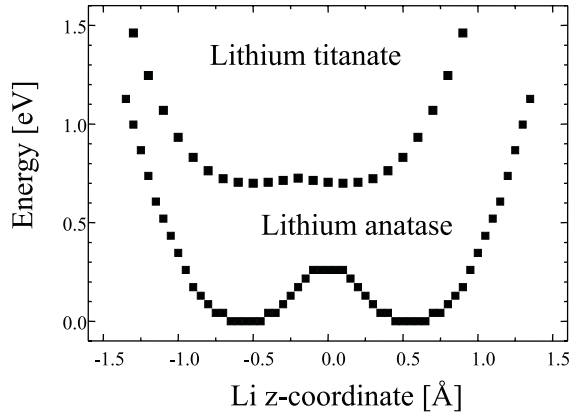
Figure 5.12: *Energy as a function of the Li-ion position along the c-direction in the center of the oxygen octahedron. Model 3 represents lithium in the Li-titanate phase and model 4 lithium in the Li-anatase phase. The energy is calculated statically by relaxing the lattice for each lithium position. For convenience the absolute energy position of both potential curves has been shifted to zero for the anatase minima.*

diffraction result (1.61 Å for Li-anatase and 0.7 Å for Li-titanate). The calculations correctly reproduces the symmetry of the Li positions in anatase with respect to the octahedron center, and the distortion of two Li-positions in Li-titanate with respect to the center of the oxygen octahedron.

5.4.3   Discussion quasi-elastic neutron scattering and molecular dynamics

The line broadening in quasi-elastic neutron scattering indicates thermally activated lithium dynamics in Li-titanate with a correlation time of 1.7 ps at 250 K. We distinguish three possible processes based on a difference in their typical time scales: (1) inter-octahedron jumps, (2) intra-octahedron jumps (between site *I* and *II*) and (3) local lithium vibrations. Random lithium hopping from one octahedral site to another, approximately separated by 2.5−3.5 Å (see section 5.3) on a timescale of picoseconds would lead to diffusion where the lithium is not confined within a specific volume. Hence, this would result in a strong decrease of the EISF with Q and also to a Q dependence of the line-width (Q^2 for random diffusion) for the Q-range probed, both of which are not observed (conform figure 5.7 and 5.8). This is consistent with our recent NMR experiments [23] where for Li in Li-titanate the mean residence time between these inter-octahedral hops was determined to be on a much longer time scale of around $\approx$ 40 μs at 250 K . Clearly, another, faster, dynamical process with limited spatial amplitude causes the quasi-elastic signal. In order to discriminate between the intra-octahedron lithium hopping and local vibrations the MD simulations were performed. For the ordered lithium "chain" model (model 3) the MD force field simulations reproduce the distinguishable lithium sites (*I* and *II*) in Li-titanate that were determined crystallographically. The MD simulations at 250 K result in a correlation time of femtoseconds up to 0.2 ps for the

the local vibrations and about 3 ps for the intra-octahedron hops. The latter is in rather good agreement with the experimental correlation time of 1.7 ps at 250 K. Clearly, the MD correctly predicts the existence of the two available Li-ion sites within the oxygen octahedron, and the correlation time for the hopping between them in Li-titanate. The local Li-ion vibrations with calculated frequencies higher than $5 \cdot 10^{12}$ Hz (> 0.02 eV) are outside the energy scale probed by the quasi-elastic neutron experiment.

Now that the time-scale of the intra-octahedron lithium jumps have been determined we can look back to one of the questions that initiated this study: the origin of the difference in the homogeneous ^{7}Li MAS NMR line width in Li-anatase and Li-titanate, the latter being roughly a factor 5 broader [23]. The inequivalent lithium sites in Li-titanate, Li_I and Li_{II}, might offer an explanation for the line width in terms of a distribution of chemical and/or quadrupolar shifts. However, the actual ^{7}Li MAS NMR line width (≈ 1 kHz at 9.4 Tesla) is not consistent with the time-scale of the intra-octahedron lithium mobility. Li-ion mobility on a 1.7 ps time scale will effectively result in a single well defined averaged ^{7}Li NMR environment (motional averaging). Hence, the two Li-ion positions in Li-titanate, site I and II, do not explain the large observed ^{7}Li NMR MAS line width in Li-titanate. We conclude that the line width of the ^{7}Li NMR MAS resonance in Li-titanate is prbably related to a weak coupling with the electrons [55].

The energy barrier calculated via molecular mechanics for intra-oxygen-octahedron hops, allowing the lattice to relax, resulted in 0.26 eV for Li-anatase and 0.026 eV in Li-titanate. The latter is significantly larger than the 5.7 meV experimentally found for lithium in Li-titanate. Although no experimental result is available for the barrier in Li-anatase it is also relatively large if we consider that the experimentally value found by NMR for inter-octahedron diffusion [23] (which may be expected to be much higher) equals 0.2 eV. Similarly, the inter-octahedron barrier itself, 0.2 eV in Li-anatase and 0.09 eV in Li-titanate, appears to be over-estimated by static calculations performed by other authors, ≥ 0.5 eV for Li-anatase [8] and 0.5 eV for Li-titanate [9]. Because the calculated "static" barrier is too high, this implies that the lithium mobility is stimulated by the dynamics of its environment, which is partly taken into account in the MD simulations, but totally absent in the molecular mechanics. In performing static energy calculations one assumes that the time scales of the diffusing particle and that of the environment, the lattice, are uncorrelated. The particle is assumed to move slowly compared to the rapid fluctuations of the lattice. As a result at each step of the diffusion process the lattice is assumed to be entirely relaxed. However, in reality the diffusive motion is usually stimulated and controlled by coupling with the fluctuations of the environment, leading to lower effective energy barriers [76]. Also coupling between the diffusing particles can lead to reduced barriers for diffusion [77]. In the Li-titanate phase the suggested Li-ion ordering in the a-direction might indicate such a coupling.

The time and length scales of the intra-oxygen octahedron dynamics are of the order of picoseconds and Ångstroms. It should be noted that this is on a much shorter time-scale than the inter-oxygen octahedron Li-ion diffusion [23], and the inter-phase domain Li-ion diffusion [24] which are in the order of microseconds and milliseconds respectively.

5.5   Concluding remarks

Inserting lithium in anatase results in phase separation in a lithium poor phase, composition Li $_{0.026}$TiO$_2$ with the original anatase structure, and a lithium rich phase, composition Li $_{0.52}$TiO$_2$ with a slightly different structure compared to anatase. In both phases two Li-ion positions appear to be available within the oxygen octahedron, see figure 5.5.

The finding of discrete Li sites inside distorted oxygen octahedra is rather remarkable. However, one would expect that Li intercalated TiO$_2$ is not the only oxide in which this occurs, but that this is much more general for transition metal oxides. The fact that such discrete sites have not been observed before is probably related to the difficulty of observing Li in diffraction experiments, or the difficulty in assigning resonances of a local probe like NMR for that matter. In neutron diffraction performed with inferior resolution, statistics and limited d-range, these sites will simply not be resolved, and in the best cases will just be identified as an anisotropic temperature factor. Clearly this is not the actual situation. An electron in the material will not interact with the Li at a position described by temperature factors, but with the instantaneous Li position that is on either of the multiple sites. The structure also appears less regular, because the Li can occupy multiple sites in an octahedron. One of the consequences is that theoretical work on this type of compounds will require modifications; special care should be taken with respect to the Li positions.

The Li positions in anatase are found symmetrically above and below the middle of the surrounding oxygen octahedron, see figure 5.5. These positions are reproduced by MD simulations (model 4, figure 5.10). The distinguishable Li sites in Li-titanate are also reproduced by the MD simulations, but only if a specific Li-ordering is assumed. This ordered structural model can be argued based on simple repulsive Coulomb interactions between the Li-ions. However, it does not lead to a superstructure in the observed neutron diffraction powder patterns due to the short range of the ordering in combination with the slow Li-ion hopping between the neighboring octahedra. The simulations thus show that Li-Li interactions are of considerable influence in this system. The temperature dependence of the lithium occupation in site I and II in Li-titanate reveals a 3.4 meV energy difference between the sites. The combination of molecular dynamics simulations and quasi-elastic neutron scattering provides insight into the intra-octahedron dynamics between the two sites. Quasi-elastic neutron scattering results in a correlation time of about 1.7 ps at 250 K for lithium hopping between the two sites located within the oxygen octahedron. This hopping appears to be thermally activated from which a 5.7 meV potential barrier between the sites can determined. The overestimation of potential barriers by static calculations for lithiated TiO$_2$ may illustrate the importance of lattice dynamics in the Li-ion mobility in this system.

Chapter 6

Ti K-edge EXAFS and XANES in lithiated anatase TiO$_2$

Abstract

Lithiation of anatase TiO$_2$ results in two coexisting phases. X-ray absorption at the Ti K-edge as a function of lithium content is interpreted as a sum of these two crystallographic phases. The changes in the near K-edge region of Ti (XANES region) indicate that the Li-ion charge compensating electron mainly occupies the crystal field split Ti $3d$ t_{2g} atomic orbitals positioned at the bottom of the conduction band. A qualitative model for the electronic structure of Li-titanate is formulated based on the XANES results, NMR results presented in chapter 3, and a number of theoretical and experimental studies found in literature.

6.1 Introduction

In the previous chapters the main subject has been the structure and the Li-ion dynamics of lithiated anatase. The electronic structure was only involved in chapter 3, where the chemical shift variation with temperature in the NMR spectra was interpreted as an increase of electron density in the conduction band consisting of mainly Ti-$3d$ and O-$2p$ atomic orbitals (AO). Upon Li-intercalation the original white anatase powder turns dark blue and a thin film changes from transparent to partial reflecting. This electrochromic effect is due to the charge compensating electron that enters the material with the Li ion. Generally the charge compensating electron entering transition metal oxides is assumed to enter the lowest unoccupied AOs mainly comprised of transition metal-$3d$ AOs with O-$2p$ admixture [20, 78, 63]. In principle the charge compensating electrons raise the Fermi level. However, the Li ion can be expected to lower the energy band structure, hence compensating for the rise in the Fermi level [78]. For anatase TiO$_2$ the coloration mechanism seems to remain unclear as different interpretations have been suggested. A number of authors attributed the electrochromic effect to absorption by nearly-free electrons, either compensating for intercalated Li-ions or for Li-ions accumulated at the solid/liquid interface [11, 12, 13]. This interpretation suggests a delocalized nature of the highest occupied electron states. In contrast, other authors suggested a semi-localized electron character based on conductivity and optical absorption [22, 14], and

polaron absorption by electrons localized at Ti [16, 15], giving rise to Ti^{3+} states or electrons trapped at surface states. Fully localized Ti^{3+}-*3d* states seem unlikely since they are known to be paramagnetic and hence would lead to large chemical shifts in NMR spectra and prominent intensities in ESR spectra, both of which are not observed [55, 23]. The calculations of Stashans *et al.* [19] predict a Li-ion induced local donor state with Ti-*4s* character positioned roughly midway in the band gap. The optical absorption resulting from their band structure model agrees well with absorption experiments [3, 14]. However, from the NMR [7]Li chemical shift variation with temperature presented in chapter 3 a donor level only about 40 meV below the conduction level was suggested, in contrast to the 1.2 eV calculated by Stashans *et al.*.

The localized character is also suggested by the formation of covalent Ti-Ti bonds in Li-titanate which are occupied by the charge compensating electron [22]. More specifically, Nuspl *et al.* [21] argued that the structural change of anatase TiO_2 upon lithiation to $Li_{0.5}TiO_2$ can be explained by filling of the Ti-$3d_{yz}$ levels at the bottom of the conduction band by the Li-ion charge compensating electrons. These Ti levels have a strong binding interaction with the other Ti atoms and form zig-zag Ti-Ti bondings (see chapter 5) in the *b*-direction that stabilize the structure of $Li_{0.5}TiO_2$. The formation of Ti-Ti zig-zag bonds suggests non-metallic resistivity as measured in Li-doped anatase, which would not be expected if the electrons are delocalized over the whole Ti-O framework [22]. Also the covalent character of these bonds might be consistent with the absence of appreciable amounts of paramagnetic Ti^{3+} states, [22, 55, 23].

Another aspect of the electronic structure is the influence on the Li-environment. For insertion ratios Li/Ti> 0.5 Luca *et al.* [55] detected an extra Li-ion environment with NMR that was attributed to a weak coupling with conduction electrons. An intriguing observation is the difference in ^{7}Li NMR line-width between lithium in Li-anatase and in Li-titanate [23] (see chapter 3) where the field dependence also indicated a coupling with the conduction electrons.

We realize that a wealth of information is available, but how can these be combined to yield a consistent picture? In this chapter we attempt to formulate such a consistent picture after adding extra experimental data in the form of Ti K-edge X-ray absorption spectroscopy (XAS) in TiO_2 and in Li-titanate ($Li_{0.5-0.6}TiO_2$).

Ti K-edge XAS offers the possibility to study both the atomic structure (EXAFS) and the electronic structure (XANES) as shown in section 2.3. In this chapter we study changes measured with Ti K-edge XAS in transmission for a range of Li intercalated Li_xTiO_2 ($0 < x < 0.7$) anatase powders. The aim is to study the changes in the electronic state upon lithium insertion. From the preceding chapters it is clear that for overall compositions Li_xTiO_2 ($0 < x < 0.6$) two phases coexist, lithium-poor anatase ($x \approx 0.01$) and lithium-rich lithium titanate ($x \approx 0.6$). The transmission XAS should also be consistent with this interpretation. Although the XAS signal contains both near edge region (XANES) and the extended region (EXAFS), the main subject of this study will be the XANES region which is related to the electronic structure. The EXAFS region is connected to the nearest neighbor structure which was already studied extensively in chapter 5.

6.2   Materials and methods

6.2.1   Sample preparation

Microcrystalline TiO_2(anatase) (99%) was obtained from Janssen Chemica. The Li_xTiO_2 samples were prepared by chemical intercalation of the pure powder with n-butyllithium (1.6 M Aldrich) [56]. The powders were mixed with hexane, and different amounts of n-butyllithium were added while stirring the mixture in order to obtain the following compositions: $x = 0.03, 0.07, 0.12, 0.19, 0.25, 0.32, 0.41, 0.5, 0.6, 0.7$ for Li_xTiO_2. All sample preparations were carried out in a glove box in an inert argon atmosphere to prevent reaction of Li with air or humidity. After preparation, the samples were subjected to wet-chemical Inductively Coupled Plasma spectroscopy (ICP) analysis to check the overall composition, especially the Li/Ti ratio. These results confirmed that during preparation all the lithium reacts with the TiO_2 (anatase), yielding the overall compositions $\pm3\%$ as calculated from the amount of n-butyllithium in the solution. The samples were thoroughly mixed with boron nitride to increase the powder volume ($\sim$ 90 weight % boron nitride, $\sim$10 weight % Li_xTiO_2) so that mechanically stable samples could be pressed. Before the measurements, transmission scans with a small pinhole over the sample were performed in order to check the homogeneity. The sample holders were sealed under argon atmosphere with Kapton windows to prevent sample degradation during the experiments.

6.2.2   X-ray absorption experiments

The experiments were performed at the X-ray undulator beamline BW1 at the DORIS III storage ring at Hasylab, (Hamburg, Germany) operating at a positron energy of 4.45 GeV with $\approx$100 - 150 mA of stored current. A double-crystal monochromator with two flat Si(111) crystals was used. Transmission XANES and EXAFS data were collected at the Ti K-Edge ($\sim$4966 eV) at room temperature. In the vicinity of the absorption edge it is assumed that the full width at half maximum of all peaks in the derivative spectrum closely resembles the energy resolution of the instrument. We estimated a value of about 0.89 ± 0.05 eV (FWHM) from the 1st derivatives of measured XANES spectra of a Ti-metal reference foil. Incident and transmitted intensities were measured with nitrogen filled ionization chambers. A Ti metal foil was measured in transmission between the second and a third ionization chamber in order to calibrate the energy scale of the monochromator simultaneously with each of the samples. Suppression of higher harmonics in the Bragg-reflected beam was achieved by de-tuning of the monochromator crystals to about 40-50% of the maximum intensity. Careful de-tuning is of extremely high importance at low energies , because the absorption of higher harmonic photons is significantly lower compared to the first harmonic.

6.2.3   Data correction and analysis

The XAS data analysis was performed using the WinXas package [46]. The data fitting in terms of the two crystallographic phases, present in the lithiated anatase system, was checked with principal component analysis (PCA) [79], which is also included in the WinXas package. With PCA one can determine the minimal number and the type of

the model compounds which are necessary to reproduce the measured spectra by means of a linear combination. PCA is equivalent to the methods in linear algebra which are performed to determine the dimensionality of the vector space for the spectra. It is a commonly used tool, e.g. for spectroscopic techniques, and has recently been applied also for the detailed analysis of X-ray absorption spectroscopy data [79].

6.3   Results and discussion EXAFS region

Upon lithiation distinct changes are observed in the Fourier-Transforms of the extended X-ray absorption fine structure data as illustrated in figure 6.1. All visible coordination shells decrease significantly in amplitude with increasing Li amount. Even for Li$_{x=0.12}$TiO$_2$, a clear decrease of all peaks is present. This is the result of the phase transition that takes place during the lithium insertion [4, 58, 23] extensively discussed and characterized in chapters 5 and 3. The first strong peak represents the first coordination shell of oxygens surrounding the Ti atom. Although the EXAFS can be related to structural changes we do not put effort to do so here. Luca *et al.*[55] studied the structural changes and concluded that the lithium titanate structure probed with EXAFS was in accordance with the known changes upon lithiation [4, 22]. However, Luca *et al.* did not interpreted the EXAFS data of intermediate compositions in terms of two coexisting phases. The present EXAFS data are analyzed by means of PCA in order to investigate the validity of the two-phase interpretation found in previous studies [23][25]. Indeed, PCA indicates the presence of only two components, in this case the experimental spectra for Li$_x$TiO$_2$ $x = 0$ and $x = 0.6$. The EXAFS data can be fitted with the combination of the two coexisting phases, anatase TiO$_2$ and Li$_{0.6}$TiO$_2$ as shown in figure 6.2 for the composition Li$_{0.19}$TiO$_2$. The effect of the small fraction of Li in the anatase phase ($x \approx 0.01$) in equilibrium with the Li rich phase Li$_{0.6}$TiO$_2$ is assumed to be negligible. The PCA analysis and the least squares fits were always performed on the absorption spectra $\mu(k)$, the fit quality is good (see 6.2) with an residue of less than about 2-3%. It has to be mentioned, that neither TiO or Ti$_2$O$_3$ spectra can fit the data.

The observed changes in the fine structure of the EXAFS spectrum upon lithiation for all the compositions can be modelled using only different fractions of the anatase TiO$_2$ and Li$_{0.6}$TiO$_2$ spectra, the results of which are included in figure 6.5. We assume these fractions to be the crystalline phase volume fractions and compare these with X-ray diffraction results, obtained in a previous study [23]. This shows in addition, that no significant amounts (< 2-3%) of amorphous phases contribute to the EXAFS signals.

6.4   Results and discussion XANES region

The XANES spectra of the Li$_x$TiO$_2$ samples and pure anatase TiO$_2$ as well as their derivatives are shown in figure 6.3. With increasing Li insertion ratio, x, the pre-edge features decrease in intensity and their positions remain nearly unchanged up to about x=0.3. The edge positions, which are marked in the derivative spectra, are shown in figure 6.4 as a function of the insertion ratio. Before proceeding with a detailed description of the XANES features, it is essential to realize that two distinct crystallographic phases coexist in the Li$_x$TiO$_2$ system for compositions Li$_{0.01<x<0.6}$TiO$_2$ (chapters 3 [23] and 4
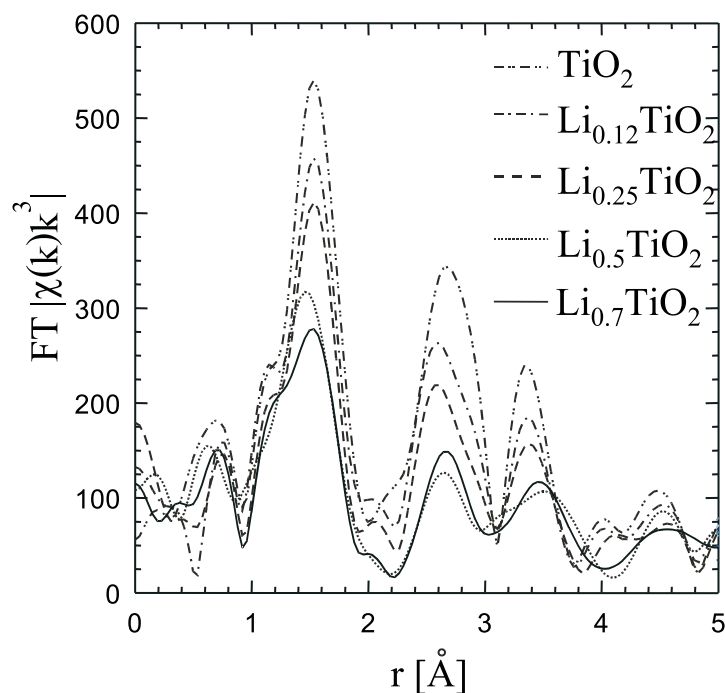
Figure 6.1: *Magnitude of the Fourier-Transform of the k^3-weighted absorption fine structures extracted above the Ti K edge for a number of overall compositions.*

[24]). The compositions coexisting in these micro-powders are a lithium-poor phase with $x \approx 0.01$ and a lithium-rich phase with $x = 0.5 - 0.6$. The changes observed in the XANES spectra might therefore be explained by the shift in the ratio of the two phases. In agreement with the EXAFS region, PCA gives strong evidence for the presence of only two principal components and suggests that anatase TiO_2 and $Li_{0.6}TiO_2$ are well-suited reference compounds, again assuming $Li_{0.01}TiO_2$ resembles pure TiO_2. The fit residuals are 1-1.5%, therefore the observed edge shift with increasing x in Li_xTiO_2, figure 6.4, should not be interpreted as a homogeneous change of the Ti environment, as suggested by Luca *et al.* [55], but rather as result of the change in the relative weight of both edges originating from the two different crystallographic phases.

The relative contributions of Li-anatase and Li-titanate as determined from the PCA analysis of the XANES and EXAFS data are plotted in figure 6.5 together with the results of the XRD experiments [23] as a function of the Li content. XRD and XANES give quantitatively the same results implying that all the structures that are formed are crystalline. As a result only differences between anatase and Li-titanate need be considered.

The anatase near edge structure has been the subject of several theoretical and experimental studies [80, 81, 82, 83, 55]. Throughout these studies the various features have been subject of debate. However, the following assignment seems the most accepted. The four pre-peaks (see figure 6.6), assigned *A1-3* and *B*, correspond to transitions of the core electron to Ti *3d-4p-4s* hybridized states. The *A1* pre-peak is due to a t_{2g}
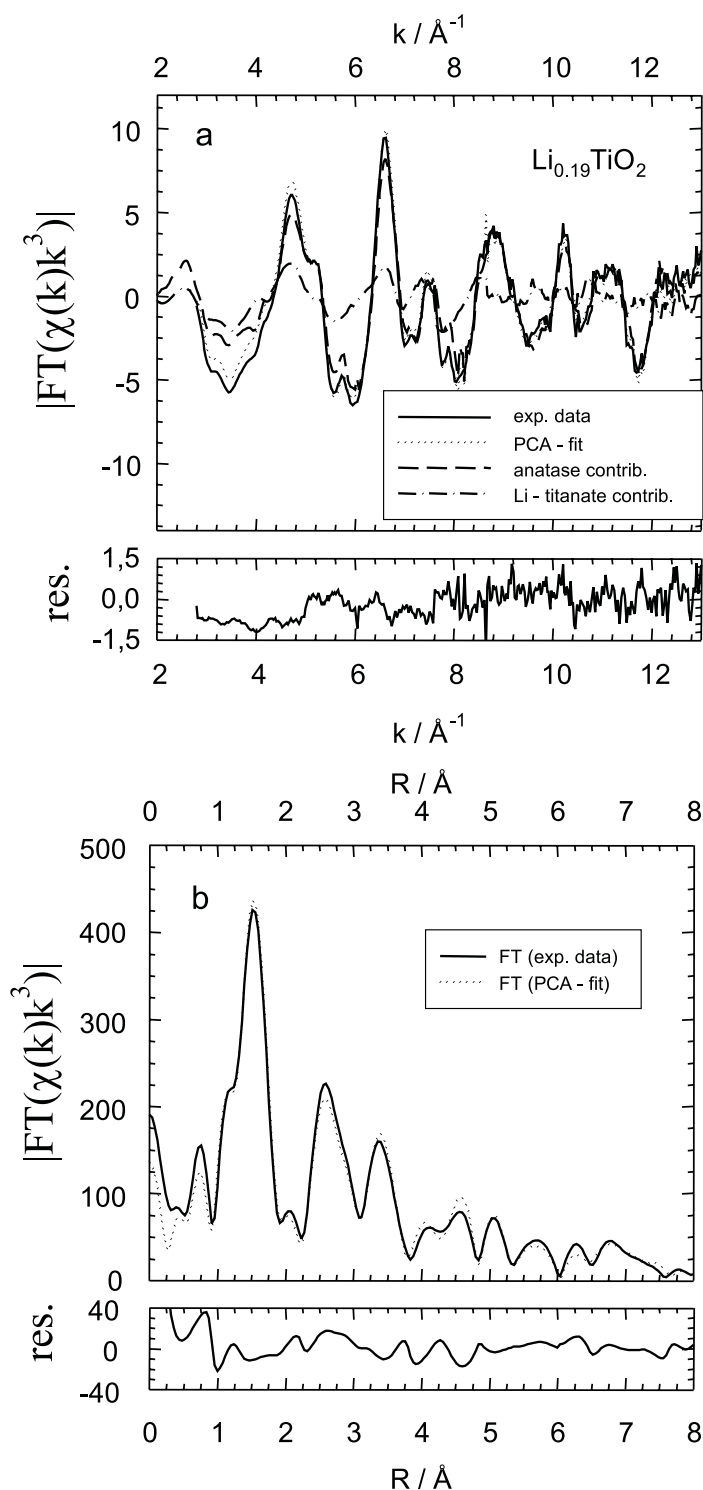
Figure 6.2: *(a) Least squares fit of the extended X-ray absorption fine structure (EXAFS) for the $Li_{0.19}TiO_2$ composition with contributions of anatase and Li-titanate as shown. (b) R-space representation of the experimental data and the fit from (a). The fit residual is shown in the bottom of each graph.*
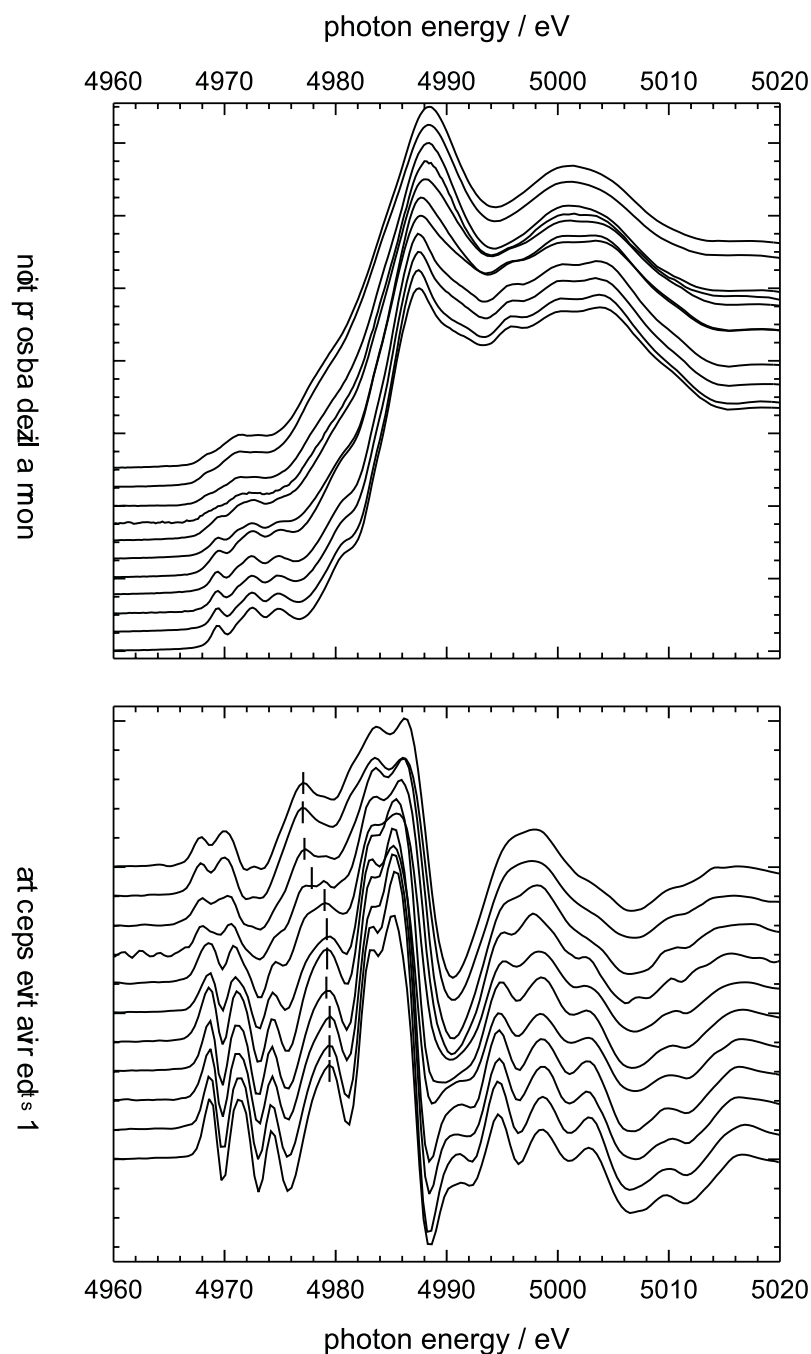
Figure 6.3: *Top: Near edge X-ray absorption spectra of several Li-intercalated anatase TiO₂ powders in the vicinity of the Ti K-edge (4979 eV) measured at room temperature. Bottom: Derivative spectra with the edge position indicated by the vertical lines (see text). From bottom to top Li$_x$TiO₂ with x=0.00, 0.03, 0.07, 0.12, 0.19, 0.25, 0.32, 0.41, 0.5, 0.6, 0.7.*
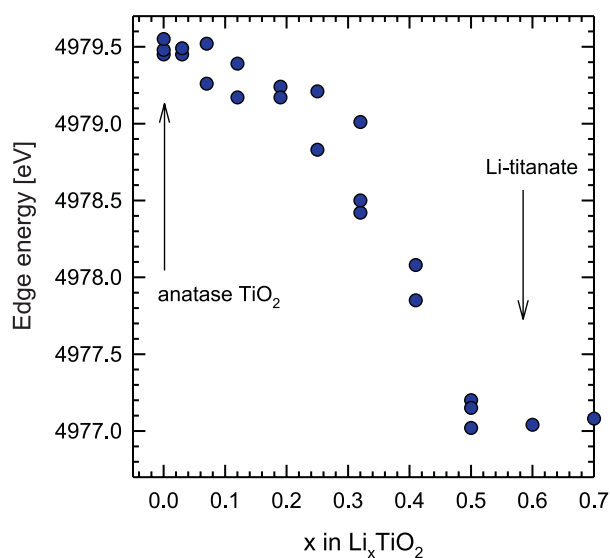
Figure 6.4: *Edge positions determined as the first inflexion point of the X-ray absorption fine structure spectra of the powder samples with overall composition $Li_x TiO_2$ where x varies from 0 (pure anatase) to 0.7. For most of the samples several measurements were performed.*
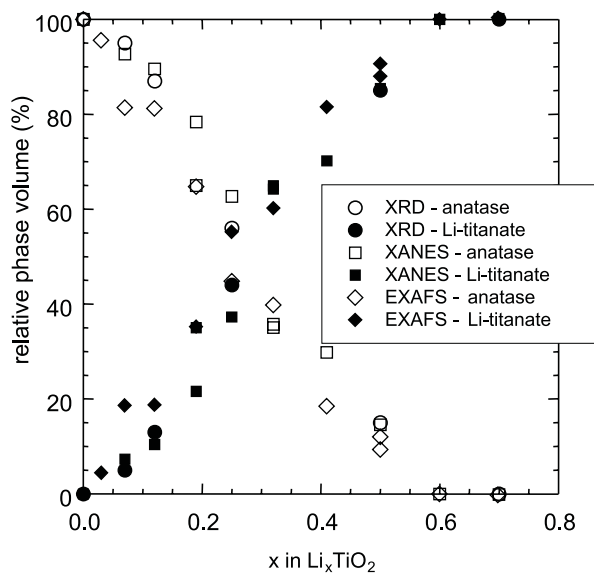
Figure 6.5: *Relative phase volume of Li-anatase $(Li_{x\approx0.01} TiO_2)$ and Li-titanate $(Li_{x\approx0.55} TiO_2)$ resulting from the XANES and EXAFS least squares fits of samples with intermediate compositions. For comparison XRD results presented in chapter 3 [23] have been included.*
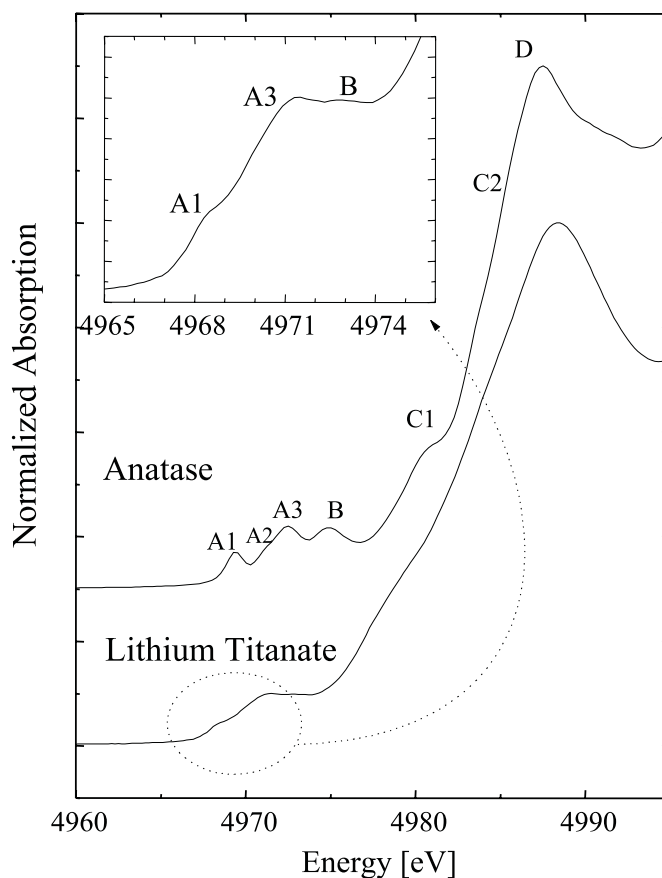
Figure 6.6: *Experimental near edge X-ray absorption spectra of anatase* TiO_2 *and* $Li_{0.6}TiO_2$ *lithium titanate. For the assignment of the different peaks, see text.*

band-like state whereas *A2* and *A3* are the results of e_g band-like states. The t_{2g} and e_g states represent the components of the crystal-field split Ti-*3d* AOs which are shifted relatively to each other in energy as a result of the octahedral oxygen surrounding of titanium (t_{2g}: d_{xy}, d_{yz}, d_{zx} and e_g: $d_{x^2-y^2}$, d_{z^2}). Interestingly, Wu *et al.* [83] argued that the *A1* feature mainly originates from the first shell of four Ti neighbors at ≈ 3.04 Å and the *A2* and *A3* feature get a substantial amount of their intensity from the second set of Ti neighbors at ≈ 3.78 Å. Apparently, the Ti-*3d* AOs influence each other via hybridization with oxygen orbitals located in between. Transition *B* has a predominantly Ti-*4p* character hybridized with the Ti-*4s* and/or O-*2p* orbitals [80]. Pre-peaks *C1* and *C2* represent transitions of the core electron towards O-*2p* states that are hybridized with Ti-*4p* states and *D* can be attributed to higher lying *p* AOs.

Figure 6.6 reveals a number of distinct changes between the spectra of anatase and lithium titanate. In Li-titanate the *A1-A3,B* features can barely be distinguished from each other and seem to be much less intense. In the inset, part of the pre-edge range of Li-titanate is expanded where the *A1* and *A3* can be recognized and with some effort even the *B* transition. The pre-edge transitions in anatase and in Li-titanate are fitted

Table 6.1: *Fit results A1,A3 and B transitions in the XANES region for anatase and Li-titanate. The FWHM was fitted for anatase and kept fixed in the Li-titanate fit.*

		E [eV]	FWHM [eV]	Area
Anatase	A1	4969.37	1.96	5.0
	A3	4972.46	2.25	2.03
	B	4974.88	3.87	8.5
Li-Titanate	A1	4968.59	1.96	1.2
	A3	4969.60	2.25	1.11
	B	4972.74	3.87	1.7

with a Lorentzian line shape to emphasize the changes, in which it was assumed that the width does not change. The results are listed in table 6.1. It should be noted that the amount of lines complicates such a fit, but nevertheless a qualitative behavior can be extracted. The interpretation of the changes in the XANES spectra is rather tedious since not only electron density is added due to the Li-ion intercalation, but the original anatase structure changes to the Li-titanate structure. However, the structural changes are small and it is generally assumed that the resulting changes in the electronic structure are small. This can be recognized in the XANES, because the transitions in anatase can, although clearly modified, still be distinguished in the lithium titanate XANES spectrum. In the following, the most prominent changes are discussed.

All transitions shift to lower energies indicating a change of the oxidation state. The edge position (the first inflection point of the absorption) shifts from the value of Ti^{4+} anatase (4979.5 eV) towards 4977 eV for L$_{0.6}$TiO$_2$. For comparison, Ti K-edge energies of some selected Ti-reference compounds are given together with the formal Ti valency in figure 6.7.

Assuming a linear relation between the oxidation state and edge position of these Ti compounds, the lithium reduces the Ti valency state in lithium titanate to about Ti$^{3.5+}$. Close inspection of the Li$_{0.6}$TiO$_2$ edge in figure 6.6 shows that the edge extends over a range larger than the TiO$_2$ edge. Therefore it seems likely that the oxidation state of Li$_{0.6}$TiO$_2$ is not a homogeneous oxidation state of Ti$^{3.5+}$ but rather a distribution between Ti oxidation states roughly between 4+ and 3.0+ given the first inflection point and comparison with the anatase spectrum. The most prominent change in the XANES transitions is the decrease of the *A1* transition, which was associated with the t_{2g} Ti-*3d* AOs, and the virtual disappearance of the *B* transition associated with the Ti-*4p* AOs hybridized with the Ti-*4s* and/or O-*2p*. Also the low energy tail of the edge has shifted to the left and pushes the XANES transitions up. The distinct decrease of the *A1* transition indicates that Li-ion intercalation reduces the transition probability towards the t_{2g} band. This can be explained by filling of these AOs by the charge compensating
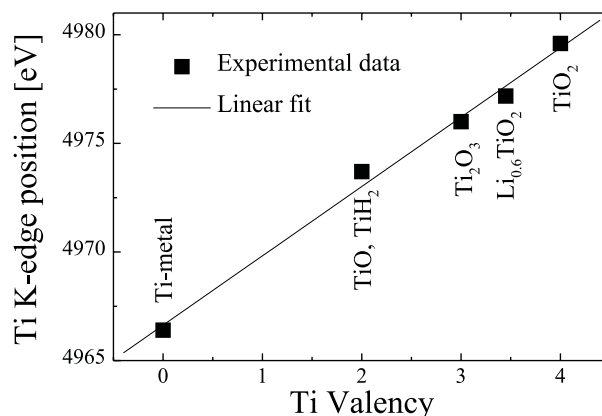
Figure 6.7: *Edge position of various Ti compounds with different oxidation states. The straight line illustrates the linear relation between the oxidation state and the edge position. The edge position of the $Li_{0.6}TiO_2$ composition suggests an average Ti oxidation state of about 3.5+.*

electrons. This is in agreement with calculations that explain the structural changes in terms of electron occupation of t_{2g} bonding bands [21]. The transition probability, i.e. the intensity of the pre-peaks, is also directly related to the structure, because the p-character of the unoccupied states is modified. In a perfect octahedral environment, the transition probability is small, while in a distorted octahedron it is higher, thus the intensity is higher. Apparently, this increase is not sufficient to cover the decrease due to the filling of these AOs. Surprisingly, the higher energy levels associated with the B transition appear to be occupied as well according to the decrease in intensity of this transition. However, the change in this absorption might also be related to the presence of the Li-ion in the donor model suggested by Stashans *et al.* [19] which was predicted to consist of Ti-*4s* orbitals whereas the B transition is expected to have admixture with these orbitals. Therefore, a drastic change in the *4s* orbitals due to the presence of Li-ions might effect the B transition.

The notion that the edge distribution is most likely the result of a distribution of oxidation states does not agree with a nearly free electron picture [11, 12, 13] where the delocalized band character can be expected to lead to a more homogeneously distributed Ti valency resulting in a well defined edge position. In a more localized electron picture, the distribution of possible valences is easily explained by the local random Li occupation of sites. Note that only 0.6 of the oxygen octahedra has a Li inside and this Li may be on two different positions, see chapter 5. In a more delocalized picture, one would expect that it is only the average Li site occupation that matters. A more localized electron state character is also suggested by broad optical absorption bands [14] and the non-metallic conductivity [22, 14]. The statement of Wu *et al.* [83] that the *A1* feature mainly originates from the first shell of four Ti neighbors at ≈ 3.4 Å also supports a more localized picture although not localized on a single Ti atom, as suggested by XPS [16]. Finally, the localized character is also suggested by the formation of Ti-Ti zig-zag bonds in the *yz*-direction as can be explained by filling of the bottom of the conduction
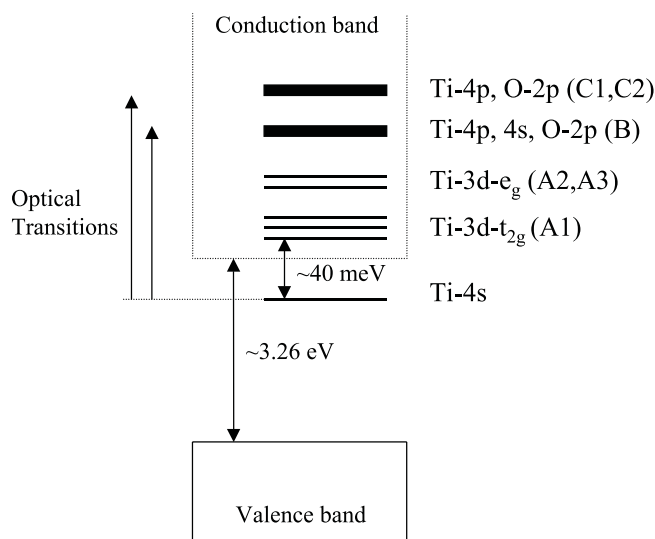
Figure 6.8: *Proposed electronic structure of Li-titanate. The corresponding XANES peaks are given in parentheses.*

band consisting of Ti-*3d*$_{yz}$ AOs (part of the t_{2g} crystal field split AOs) [21].

The XANES results presented here can be interpreted as a filling of these t_{2g} orbitals by the charge compensating electrons. These localized bonding AOs imply a covalent character [22] that is often observed in combination with the disappearance of magnetic moments [84]. This suggestion might explain the absence of a significant amount of paramagnetic Ti^{3+} as concluded from NMR [55, 23] and ESR [85] experiments. The variation of the ^7Li NMR chemical shift with temperature in both Li-anatase and Li-titanate reported in chapter 3 was interpreted as an increase of electron density in the conduction band with increasing temperature. The origin of this increase may be a donor level below the bottom of the conduction band induced by the interstitial Li-ion. Generally, donor states in semi-conductors are localized states below the bottom of the conduction band. The temperature dependence of the ^7Li NMR chemical shift suggests that the donor level is located roughly 100 meV and 40 meV below the conduction band for Li-anatase and Li-titanate, respectively. The local donor state induced by the Li-ion was also calculated in a theoretical study of Stashans *et al.* [19]. However, the position of the donor state, consisting of Ti-*4s* AOs, was determined to be ≈ 1.2 eV below the bottom of the conduction band, compared to 40 meV determined from the temperature behavior of the ^7Li NMR chemical shift. The donor state model of Stashans *et al.* [19] predicts the experimentally measured broad optical absorption bands. Although the absolute position of the calculated donor level is quite different from that suggested by NMR, the relative positions of the AOs involved in the optical transitions may still be correctly predicted by the calculations of Stashans *et al.* [19].

The discussion of the present results, the NMR result in chapter 3, results of Nuspl *et al.* [21] and Stashans *et al.* [19] can be summarized by a model of the electronic structure in Li-titanate as illustrated in figure 6.8. Upon lithiation a donor state is created about 40 meV (chapter 3) below the conduction band. The Li-*2s* electron will occupy this lowest free orbital. According to the Boltzmann distribution at RT about 46% of the

electron density will be thermally activated to the conduction band, the bottom of which mainly exists of the lower lying Ti-$3d$ t_{2g} and e_g levels. Donor states that mainly consist of Ti-$4s$ AOs, will have a localized nature. Additionally, covalent Ti-$3d_{yz}$ bonds may also have a localized character. This might explain the low electric conductivity [22, 14]. The changes of the number of conduction electrons with temperature will contribute to the non-metallic behavior.

The question is if this model might explain the difference in the homogeneous [7]NMR line width between lithium in Li-anatase and Li-titanate [23] (chapter 3) and the suggested weak coupling of lithium with the conduction electrons for insertion ratios Li/Ti> 0.5 [55] where a second Li-environment appears in Li-titanate with a larger line-width [55]. The decrease of the ^{7}Li NMR chemical shift with increasing temperature, interpreted as increasing Ti-$3d$ electron density, already implies a coupling. The only qualitative observation we can make is that an increase of the Ti-$3d$ electron density can be expected to result in a stronger coupling. This is consistent with the observed behavior, increasing the insertion ratio Li/Ti, thereby increasing the Ti-$3d$ electron density, resulting in larger NMR line-widths and larger chemical shifts.

6.5 Conclusions

The interpretation of the of the changes in the EXAFS and XANES region of the X-ray absorption spectra is that of a two-phase system in accordance to other structural studies. The changes in the near K-edge region of Ti indicate that electron density, donated by the inserted Li, occupies the crystal field split Ti-$3d$ t_{2g} Ti-Ti bonding atomic orbitals positioned at the bottom of the conduction band as predicted by Lunell *et al.* [18]. The lithium donated Ti-$3d$ electron density is in agreement with recent temperature dependent NMR results which may be interpreted as a Li-induced donor state approximately 40 meV below the conduction band, as proposed by Stashans et al. [19]. This causes the Ti-$3d$ electron density to be temperature dependent. The distribution in the Ti edge position observed in lithium titanate indicates a distribution of Ti valences around $Ti^{3.5+}$. The presence of such a distribution is consistent with a more localized electron density induced by the local Li site occupancies. The small difference between the highest donor level and the conduction band and the relatively localized nature of donor states and of the bonding Ti-$3d$ atomic orbitals might explain the non-metallic resistivity in Li-titanate.

Chapter 7

In-situ neutron reflectometry on Li intercalation in thin film anatase TiO$_2$

Abstract

In-situ neutron reflecometry reveals the intercalation scheme of lithiated thin film anatase TiO$_2$ in terms of phase boundary movement. The Li-rich lithium titanate phase progressively moves from the electrolyte interface into the anatase TiO$_2$ electrode as a front parallel to this interface. In contrast to previous suggestions for this system, the phase front moves back during lithium extraction in exactly the same way it came in. The electrochemistry side reactions result in a ≈ 5.5 nm-thick film on top of the TiO$_2$ electrode extending into the organic electrolyte which is believed to passivate the Li-intercalation.

7.1   Introduction

Anatase TiO$_2$ is an interesting model system for Li-ion batteries in which a two phase equilibrium in one of the electrodes maintains the constant potential. Recent investigations suggest that the lithium intercalation in thin film anatase TiO$_2$ is mainly determined by the establishment and movement of a diffusion-controlled phase boundary, parallel to the electrode surface, between the Li-rich (Li$_{\approx 0.5}$TiO$_2$, referred to as Li-titanate) and the lithium poor phase (Li$_{\approx 0.026}$TiO$_2$, referred to as Li-anatase) [7, 23, 24]. During the Li-ion insertion the original tetragonal anatase TiO$_2$ phase undergoes an orthorhombic distortion, which results in the Li-titanate phase [4, 25]. For thin dense films, Van de Krol *et al.* [7] suggested that the Li-titanate phase penetrates the TiO$_2$ layer with the phase boundary parallel to the surface of the film. This in contrast to for instance a percolation scheme where the Li-titanate phase would penetrate the original anatase layer only at certain regions of the thin film, for instance at the grain boundaries. Further intercalation would increase both the perpendicular and the lateral dimension of these percolation paths eventually leading to a homogeneously intercalated film. Van de Krol *et al.* [7] proposed a specific scheme for the de-intercalation in order to explain the difference between the rate of insertion, 2.0×10^{-15} cm^{2}s^{-1}, and the rate for lithium extraction, 6.0×10^{-15}cm^{2}s^{-1} in CVD films [5]. Based on the assumed faster lithium

diffusion in the Li-anatase they expected fast depletion of lithium in the near-surface region of the Li-titanate phase (which is in contact with the electrolyte). As a result, during lithium extraction, the Li-anatase phase starts to grow at the electrolyte into the layer at the expense of the lithium titanate phase.

In order to study these intercalation schemes, *in-situ* neutron reflectometry (NR) is performed on lithium intercalated anatase TiO$_2$. For the thickness of these layers, $\simeq 25$ nm, the relatively high sensitivity for lithium (compared to X-rays), and the ability of neutrons to pass through a solid substrate, NR is a unique probe in determining the lithium density profile perpendicular to the surface of reflection. In the case of lithiated anatase the lithium rich Li-titanate phase contrasts with the lithium poor Li-anatase phase. Because the translation of the reflection data into a density profile is not unique, as the neutron phase information is lost during detection, the data are fitted with models representing a specific density distribution. A common method to decrease the number of possible models is to vary the contrast for neutrons of one or more components. For instance, the electrolyte density as "seen" by neutrons can be matched with anatase TiO$_2$ by deuterating a specific fraction of the electrolyte. However, due to the extreme costs of deuteration and the limited degrees of freedom of the system which facilitates the interpretation here, the contrast is not varied for these experiments.

7.2 Materials and methods

7.2.1 Thin film anatase TiO$_2$

A thin (≈ 25 nm thickness) 100×50 mm^2 anatase TiO$_2$ layer was prepared by r.f. sputtering deposition (Perkin-Elmer 2400). The following deposition procedure was used. First the optically polished single crystal quartz substrate ($100 \times 50 \times 10$ mm^3)was cleaned by standard cleaning procedures. After pre-sputtering of the targets, ≈ 20 nm Au was sputtered during 1.2 min using an r.f. power of 200 Watt and a bias voltage of -900 V. The argon flow was 15 ml/min resulting in a background pressure of $2 \cdot 10^{-2}$ mbar. The gold serves as a back contact for the TiO$_2$. The TiO$_x$ deposition took place in an argon/oxygen mixture of 3.2 ml/min argon and 5.2 ml/min O$_2$, respectively. The total background pressure was $4 \cdot 10^{-3}$ mbar. An r.f. power of 250 Watt (bias voltage of -980 V) resulted in a deposition rate of about 1 nm/min. After deposition the films were annealed in an oxygen flow at 280 C$^\circ$ for 5 hours. A ramping of 20 C$^\circ$/min was used during heating as well as cooling of the sample. Grazing incidence X-ray diffraction showed the characteristic anatase TiO$_2$ reflections and also indicated a preferred orientation of the crystallites along the c-axis perpendicular to the surface.

7.2.2 *In-situ* electrochemistry

In figure 7.1 the neutron-electrochemical cell is shown, which was designed similar to a previous cell [86]. The working electrode, anatase TiO$_2$, on top of the single crystal quartz block was separated by an air-tight teflon spacer from a glass block, together forming a box completely filled with the electrolyte. This arrangement was clamped between stainless steel plates which were accurately mounted on the neutron reflectometer. Ports were introduced in the teflon for the electrolyte inlet/outlet and for the counter
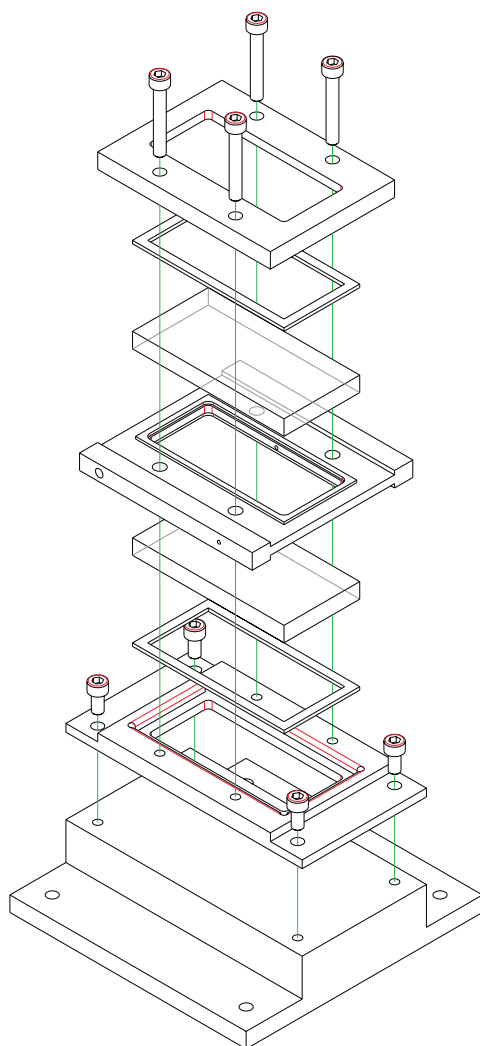
Figure 7.1: *Expanded view of the in-situ electrochemical cell designed for neutron relfec-tometry*

and reference electrode. Single crystal quartz was chosen as substrate because of its high transmission of neutrons ($\sim 70\%$) preventing high losses in the incoming and reflected neutrons. The TiO_2 electrode surface area exposed to the electrolyte was 36 cm^2. Lithium foil, size 2×8 cm^2, was used as counter electrode. Contact with the working electrode was made through the gold layer at the edge of the quartz block, which was located outside the teflon spacer. The resistance of the thin gold layer over ≈ 10 cm was less than 30 Ω.

All electrochemical experiments were performed using the above three-electrode electrochemical cell designed for NR with lithium as both counter and reference electrode and an electrolyte solution consisting of 1 M $LiClO_4$ in propylene-carbonate (PC). The electrolyte volume enclosed by the electrochemical cell was about 25 cm^3. Potential control was provided by an Eco Chemie Autolab PGSTAT30 potentiostat. Lithium was galvanostatically inserted and extracted (intercalation potentials between 1.5 V and 3.0 V vs. Li) in two steps with 10 μA. The composition of Li-titanate, $Li_{0.52}TiO_2$ [25], leads

Figure 7.2: *Cyclic voltammogram of the Li intercalation of anatase TiO$_2$ at 0.2 mV/s. For both reference and counter electrode lithium is used. The electro-active TiO$_2$ surface area is 36 cm^2.*

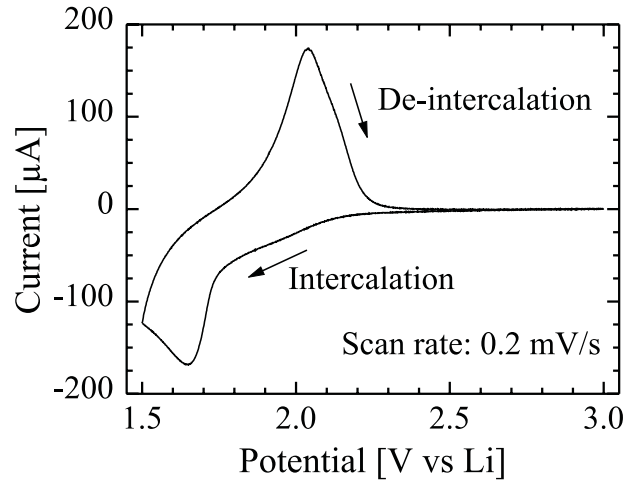for a 25 nm intercalated layer to a theoretical charge of $\approx$0.19 C, which takes approximately 5.3 hours at 10 μA for full intercalation of the film. The system was pre-cycled (cyclic voltammogram) three times with 5 mV/s between 3.0-1.5 V vs. Li. In addition one slow cyclic voltammogram was taken at 0.2 mV/s in order to estimate the amount of charge that could be inserted. Five NR experiments were performed. The first one (referred to as virgin state) after filling the cell, before the pre-cycling. The second after 2.5 hours of intercalation, then after complete intercalation, half de-intercalation, and completely de-intercalation, respectively. After each step the system was allowed to reach equilibrium before the experiment.

7.2.3 Neutron reflectometry

The NR experiments were performed on the time-of-flight neutron reflectometer SURF at the ISIS spallation source, Rutherford Appleton Laboratory, U.K. Two reflection angles were used, 0.25° and 0.60° measured for 30 and 120 minutes, respectively. The information obtained with NR is the spatial distribution of components perpendicular to the reflecting interface. The reflectivity is measured as a function of the wave vector component perpendicular to the interface $q = (2\pi/\lambda)\sin\theta$, where λ is the neutron wavelength and θ the angle of reflection. Here we use the following definition for the scattering length density (SLD): $\Gamma(z) = 4\pi \sum_i N_i(z)b_i(z)$, were the sum runs over the the different types of atoms present, $N_i(z)$ is the particle number density and b_i the coherent scattering length of the specific nuclei i.

The NR data were corrected for detector efficiencies and the wavelength dependent quartz transmission. The data analysis of the NR data was done using the STAR package [87]. The SLD profile is represented by a layered system from which the reflectivity is calculated using the matrix formalism [34].

Table 7.1: *Scattering length density (SLD) for the relevant materials*

Material	Density [g cm^{-3}]	SLD [10^{-3} nm^{-2}]
Quartz	2.65	5.26
Au	19.3	5.65
TiO$_2$	3.89	3.01
Li$_{0.52}$TiO$_2$	3.91	2.48
Electrolyte (PC) + 1 M LiClO$_4$	1.295	2.15

7.3 Results and discussion

The cyclic voltammogram, shown in figure 7.2, was performed to test the Li-intercalation in the anatase TiO$_2$ film. The cathodic (I < 0) and anodic (I > 0) peaks indicate insertion and extraction of lithium, respectively. The cyclic voltammogram is typical for lithium intercalation in anatase TiO$_2$ [7]. At potentials below the cathodic peak, additional current is lost to side reactions such as reduction of traces of water and electrolyte decomposition. As a result the charge inserted, 0.299 C, is larger than the extracted charge, 0.204 C. Assuming that the extracted charge is free of parasitic losses the layer is almost completely charged during the cycle shown in figure 7.2 since the theoretical load of the 24.4 nm TiO$_2$ (see table 7.2) layer is 0.189 C, assuming composition Li$_{0.52}$TiO$_2$ [25].

Before the sample was mounted in the electrochemical cell, a NR experiment was performed, (not shown) in order to measure the bare sample, TiO$_2$ layer and gold layer on top of the single crystal quartz substrate. The SLD of all the components, anatase TiO$_2$, Au and quartz, determined from fitting the bare sample result agreed with the values calculated from the densities and were used as input for fitting of the *in-situ* models. The calculated values for all the relevant materials are listed in table 7.1. A neutron reflection scan was then made with the sample mounted in the electrochemical cell. In this case the quartz is the incoming medium and the neutrons reflect subsequently on the gold, TiO$_2$ and the electrolyte. This measurement was done before any electrochemistry was performed and hence is referred to as the virgin state. The experiment and best fit are shown as curve (a) in figure 7.3 and the fit results are included in table 7.2. The only parameter fitted for the virgin state (related to the composition of the sample) was the SLD of the electrolyte which lead to value 13 % smaller than the calculated value (compare tables 7.2 and 7.1). This can be understood because in the calculation of the electrolyte SLD it was assumed that no volume change of the propylene carbonate (PC) occurred upon adding the LiClO$_4$ salt. Apparently, addition of the salt causes volume

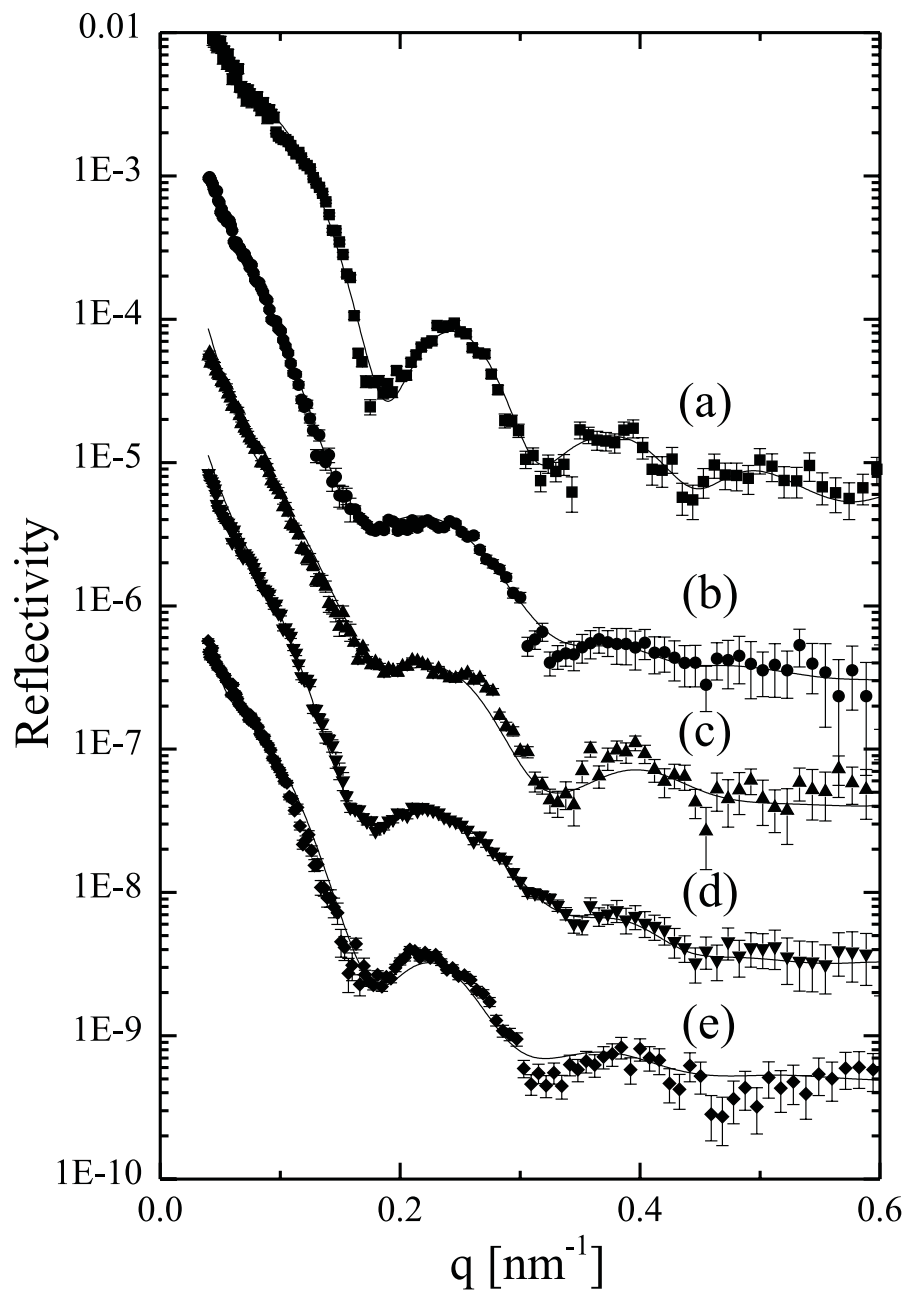Figure 7.3: *Neutron reflectometry results measured at different stages in the intercalation cycle, including the fit results corresponding to the models in figure 7.4. (a) Virgin state, before any electrochemistry is performed. (b) Approximately half way the intercalation. (c) Fully intercalated state. (d) Approximately half way the de-intercalation. (e) Empty state after the de-intercalation.*
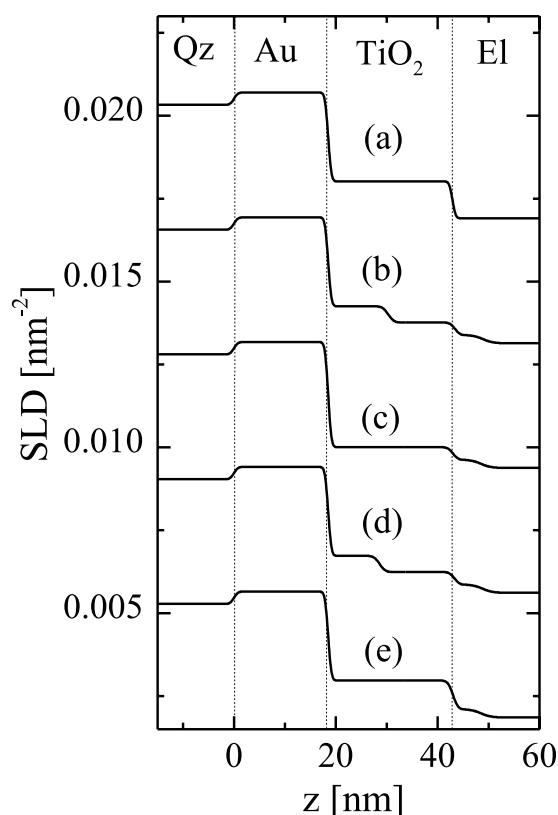
Figure 7.4: *Scattering length density profiles corresponding to the fits of the NR data in figure 7.3. "Qz" refers to the quartz which is the incoming and outgoing medium for the reflected neutrons, "El" refers to the electrolyte, 1 M LiClO4 in propylene-carbonate (PC). (a) Virgin state, before any electrochemistry is performed. (b) Approximately half way the intercalation, inserted Li decreases the SLD of the TiO_2 and thin layer develops at the TiO_2 interface with the electrolyte. (c) Fully intercalated state. (d) Approximately half way the de-intercalation. (e) Empty state after the intercalation.*

increase of the PC. Indeed, if we assume ideal mixing of 1 $LiClO_4$ molecule per 11.8 $C_4H_6O_3$ molecules (1 M $LiClO_4$ PC), the volume will increase with 4% leading to a SLD of $1.85 \cdot 10^{-3}$ nm^{-2} in good agreement with the experimental result.

In agreement with what is expected, the reflection curve for the fully intercalated state can be fitted by a single layer with the SLD corresponding to composition $Li_{0.52}TiO_2$. More interesting is the lithium distribution in case a part of the lithium is extracted. The main question is whether the NR supports the model proposed by Van de Krol *et al.* to explain the faster lithium extraction compared to insertion [7]. In the suggested model the extraction of lithium causes depletion of the lithium in the TiO_2 in the region in contact with the electrolyte (Model 2). An alternative model would be that the phase front of the Li-rich lithium titanate phase moves back to the electrolyte, exactly in the way the front moved in (Model 1). A third possibility is the homogeneously depletion of the fully intercalated layer or via percolation paths (Model 3) both of which will look

the same for specular NR.

After the initial three cyclic voltammograms, the TiO$_2$ was galvano-statically (I =-10 μA) intercalated in two steps and subsequently galvano-statically (I =10 μA) de-intercalated in two steps. After each step the system was allowed to reach equilibrium, until a constant potential was reached, before the NR experiment was performed. The NR results, including best fits, for each stage in this intercalation cycle are shown in figure 7.3. The results of the fitted parameters are listed in table 7.2 and also shown as a SLD profile in figure 7.4.

A profound change is observed comparing the NR from the virgin state and the empty state after the electrochemistry. The difference can be explained in terms of a thin layer in the electrolyte. It is generally known that in this type of organic electrolytes a layer develops when lithium is inserted and extracted. This layer is generally referred to as the solid electrolyte interphase (SEI). Specifically for lithium intercalation of anatase TiO$_2$ in contact with 1 M LiClO$_4$ in PC, the growth of this layer was studied by electrochemical quartz crystal microbalance (EQCM) measurements [88]. From such a layer it is known that it can passivate the Li transport from the electrolyte to the TiO$_2$ electrode. Although specific compounds have been suggested to build up such a layer [88], it is difficult to determine the mass from the SLD density deduced by the NR results because the highly porous SEI layer will be filled by an unknown amount of electrolyte.

The thin layer in the electrolyte on top of the TiO$_2$ is assumed not to change after the initial cyclic voltammograms, as is suggested by the EQCM results [88].

The main subject of the NR study presented here is to determine the spatial distribution of lithium in the anatase TiO$_2$ layer during insertion and extraction. Two basic models for the insertion can be formulated in an attempt to explain the changes in the observed reflection curves in figure 7.3. The intercalation is known to cause a phase transition from anatase to lithium titanate with composition Li$_{\approx 0.5}$TiO$_2$. For this type of dense film it is expected that a phase front parallel to the surface progressively moves into the TiO$_2$ during intercalation [7]. An alternative is that the lithium titanate percolates through the thin layer, for instance along grain boundaries between the crystallites. Such an inhomogeneous lithium distribution in the plane of reflection will be averaged as the reflecting neutrons have a long (μm) coherence length in the lateral direction, i.e. sample the lateral inhomogeneities on larger scales. In the case of Li diffusing via percolation paths, the experimental reflectivity can be expected to be reproduced by a single layer which SLD changes homogeneous during Li insertion. However, the half-intercalated state could not be interpreted as such. The best fit result was achieved by assuming the Li-rich lithium titanate phase (Li$_{0.52}$TiO$_2$) in contact with the electrolyte as was predicted by Van de Krol [7], see figure 7.4 (b). As a result of the negative coherent scattering length of lithium, the SLD of lithium intercalated TiO$_2$ is smaller than that of pure TiO$_2$.

The SLD density profiles in figure 7.5 present the different models. The preference for model 1, which represents the best fit (displayed in figure 7.3), is illustrated by comparing the calculated reflectivity corresponding to the different models and the experimental reflection half way the lithium extraction in figure 7.5. This indicates that the phase front moves back towards the interface between electrode and electrolyte. This is in contrast to model 2, proposed by Van de Krol *et al.* [7], which was based on the assumption that the lithium conductivity in the anatase structure is faster than in the Li-titanate

Table 7.2: *Fit results of the neutron reflection data measured at different stages in the intercalation cycle. Q represents the intercalated charge, d the layer thickness, SLD the scattering length density and σ the roughness between two media. The electrolyte SLD is determined from the virgin state and is held constant in the other fits. The layer in the electrolyte, referred to as El. Layer, which develops due to the electrochemistry is determined from the empty state and is held constant in the other fits (except in the virgin state).*

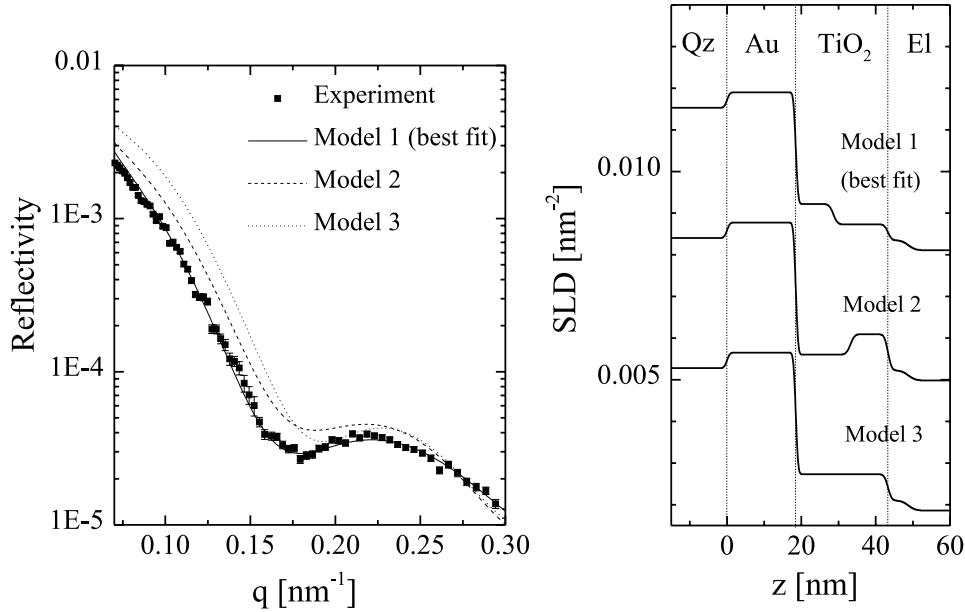| State	Q [C]	Layer	d [nm]	SLD [10^{-3} nm^{-2}]	σ [nm]
Virgin	0				
		Quartz		5.28	0.5
		Au	18.4	5.65	0.5
		TiO$_2$	24.4	2.97	0.5
		Electrolyte		1.86	
Insertion	0.15				
		TiO$_2$	11.8	2.97	0.5
		Li$_{0.52}$TiO$_2$	13.1	2.48	0.8
Fully Loaded	0.32				
		Li$_{0.52}$TiO$_2$	24.9	2.48	
Extraction	0.10				
		TiO$_2$	10.1	2.97	0.5
		Li$_{0.52}$TiO$_2$	14.7	2.48	0.8
Empty	0				
		TiO$_2$	24.5	2.97	0.8
		El. Layer	5.4	2.11	1.5

Figure 7.5: *Left: Experimental neutron reflection result at approximately half way through the de-intercalation, (d) in figure 7.3. The lines represent calculated reflectivities representing three models, see figure at the right, for the distribution of Li in the TiO$_2$ during extraction. Model 1 is the best fit result where the Li in the TiO$_2$ is distributed as a layer in contact with the electrolyte. Model 2 is the calculated reflectivity in case the same amount of Li was distributed in a layer next to the gold. Model 3 is the calculated reflectivity in case the same amount of Li was distributed homogeneously in the whole TiO$_2$ layer. Right: The SLD of the three different models for the distribution of the same amount of Li in TiO$_2$, the corresponding reflectivities are compared to the experimental result in the left figure.*

structure. This assumption has recently been shown [23] to be erroneous as the diffusion in lithium titanate is faster compared to that in anatase (see chapter 3).

In order to understand the difference in intercalation and extraction rates, another factor may play a role: the phase boundary. In our recent publication [24] (chapter 4) it was shown that the cross-diffusion between the two coexisting phases (Li-rich lithium titanate and Li-poor anatase) is rate limiting. But the question is, does the phase boundary movement implicates Li diffusion through the phase boundary? Does lithium cross the phase boundary until the concentration is reached that enforces the Li-titanate phase, or alternatively, does the strain field of the newly formed Li-titanate phase causes the progression of the phase front. In the first case the cross diffusion of Li between the two phases will determine the phase boundary movement and the overall diffusion. In the second case it is unclear how the phase boundary movement is related to the Li-ion diffusion.

From the results presented here it is clear that the difference in insertion and extraction rate can not be explained if only the anatase and the Li-titanate phases are considered, the phase front needs to be included in a complete description. One might

suggest that the higher rate of extraction compared to insertion may be explained if one assumes that the progression of the phase front costs energy whereas this energy is not needed if the front moves back during extraction. But it is unclear if this can be directly related to the cross boundary diffusion of Li which was determined in chapter 4.

7.4   Conclusions

In-situ NR has been performed in order to study the insertion and extraction mechanism in terms of the lithium distribution in anatase TiO_2. The NR supports a model in which the Li-rich lithium titanate penetrates progressively into the anatase TiO_2 electrode material as a flat phase front parallel to the surface. During the extraction the results indicate that the Li-rich lithium titanate phase withdraws in the same way it came in during insertion, rather than that the lithium near the electrolyte being depleted. This scheme may explain the observed difference between Li extraction and insertion only if the phase boundary dynamics is included in the description. In addition the neutron reflection indicates the growth of a thin layer, ≈ 5.5 nm-thick, during the electrochemical cycling, as a result of electrolyte decomposition side reactions.

Bibliography

[1] O'Regan, B.; Grätzel, M. *Nature* **1991,** *353*, 737-740.

[2] Huang, S. Y.; Kavan, L.; Exnar, I.; Grätzel, M. *J.Electrochem.Soc.* **1995,** *142,* L142.

[3] Hagfeldt, A.; Vlachopoulos, N.; Grätzel, M. *J. Electrochem. Soc.* **1994,** *141,* L82.

[4] Cava, R. J.; Murphy, D. W.; Zahurak, S.; Santoro, A.; Roth, R. S. *J.Solid State Chem.* **1984,** *53,* 64-75.

[5] Lindström, H.; Södergren, S.; Solbrand, A.; Rensmo, H.; Hjelm, J.; Hagfeldt, A.; Lindquist, S. E. *J.Phys.Chem.B* **1997,** *101,* 7710-7716.

[6] Kavan, L.; Grätzel, M.; Gilbert, S. E.; Klemenz, C.; Scheel, H. J. *J.Am.Chem.Soc.* **1996,** *118,* 6716-6723.

[7] van de Krol, R.; Goossens, A.; Schoonman, J. *J.Phys.Chem.B* **1999,** *103,* 7151-7159.

[8] Lunell, S.; Stashans, A.; Ojamae, L.; Lindström, H.; Hagfeldt, A. *J. Am. Chem. Soc.* **1997,** *119,* 7374-7380.

[9] Koudriachova, M. V.; Harrison, N. M.; Leeuw, S. W. *Phys.Rev.Lett.* **2001,** *86,* 1275-1278.

[10] Fahmi, A.; Minot, C.; Silvi, B.; Causa, M. *Physical Review B* **1993,** *47,* 11717.

[11] Enright, B.; Fitzmaurice, D. *J. Phys. Chem.* **1996,** *100,* 1027.

[12] Boschloo, G.; Fitzmaurice, D. *Proc. Electrochem. Soc.* **1997,** *97-20,* 84.

[13] Kavan, L.; Grätzel, M.; Rathousky, J.; Zukal, A. *J. Electrochem. Soc.* **1996,** *143,* 394.

[14] van de Krol, R.; Goossens, A.; Meulenkamp, E. A. *J. App. Phys.* **2001,** *90,* 2235.

[15] Cao, F.; Oskam, G.; Searson, P. C.; Stipkala, J. M.; Heimer, T. A.; Farzad, F.; Meyer, G. J. *J.Phys.Chem.* **1995,** *99,* 11974-11980.

[16] Södergren, S.; Siegbahn, H.; Rensmo, H.; J., H. L.; Hagfeldt, A.; Lindquist, S. E. *J. Phys. Chem. B* **1997,** *101,* 3087.

[17] Kang, T. S.; Kim, D.; Kim, K. J. *J. Electrochem. Soc* **1998,** *145,* 1982.

[18] Lunell, S.; Stashans, A.; Ojamae, L.; Lindström, H.; Hagfeldt, A. *J.Am.Chem.Soc.* **1997,** *119,* 7374-7380.

[19] Stashans, A.; Lunell, S.; Bergström, R.; Hagfeldt, A.; Lindquist, S. E. *Physical Review B* **1996,** *53,* 159-170.

[20] Bruce, P. G. *Solid State Electrochemistry;* Cambridge University Press: Cambridge, 1995.

[21] Nuspl, G.; Yoshizawa, K.; Yamabe, T. *J.Mater.Chem.* **1997,** *7,* 2529-2536.

[22] Murphy, D. W.; Greenblatt, M.; Zahurak, S. M.; Cava, R. J.; Waszczak, J. V.; Hull, G. W.; Hutton, R. S. *Rev.Chim.Miner.* **1982,** *19,* 441-449.

[23] Wagemaker, M.; van de Krol, R.; Kentgens, A. P. M.; van Well, A. A.; Mulder, F. M. *J. Am. Chem. Soc.* **2001,** *123,* 11454-11461.

[24] Wagemaker, M.; Kentgens, A. P. M.; Mulder, F. M. *Nature* **2002,** *418,* 397-399.

[25] Wagemaker, M.; Mulder, F. M.; van Well, A. A.; Kearley, G. J. *J. Am. Chem. Soc. Accepted for publication* **2002,** .

[26] Lützenkirchen-Hecht, D.; Wagemaker, M.; Keil, P.; van Well, A. A. *Hasylab Annual Report 2000* .

[27] Lützenkirchen-Hecht, D.; Wagemaker, M.; Keil, P.; van Well, A. A.; Frahm, R. *Hasylab Annual Report 2001* .

[28] Wagemaker, M.; van de Krol, R.; van Well, A. A. *submitted for publication* .

[29] Lützenkirchen-Hecht, D.; Wagemaker, M.; Keil, P.; van Well, A. A.; Frahm, R. *Submitted to Fuel Cells* .

[30] Wagemaker, M.; Lützenkirchen-Hecht, D.; Keil, P.; Frahm, R.; van Well, A. A. *manuscript in preparation* .

[31] Squires, G. L. *Introduction to the theory of thermal neutron scattering;* Cambridge University Press: Cambridge/London/New York/Melbourne, 1978.

[32] Price, D. L.; Sköld, K. *Methods Of Experimental Physics 23B;* Academic Press Inc.: London, 1987.

[33] Bee, M. *Quasielastic neutron scattering;* Adam Hilger: Bristol, 1988.

[34] Lekner, J. *Theory of Reflection of Electromagnetic and Particle Waves;* Martinus Nijhof Publishers: Dordrecht, 1987.

[35] Carrington, A.; McLachlan, A. D. *Introduction to magnetic resonance;* Harper and Row: New York, 1967.

[36] Slichter, C. P. *Principles of Magnetic Resonance;* Springer-Verlag: New York, 1992.

[37] Abragam, A. *Principles of Nuclear Magnetism;* Oxford Science Publications: Oxford, 1961.

[38] Kentgens, A. P. M. *Geoderma* **1991,** *80,* 271-306.

[39] Kubo, R.; Tomita, K. *J. Phys. Soc. Japan* **1954,** *9,* 888.

[40] Ernst, R. R.; Anderson, W. A. *Rev. Sci. Instr.* **1966,** *37,* 93.

[41] Bloembergen, N.; Purcell, E. M.; Pound, R. V. *Phys.Rev.* **1948,** *73,* 679.

[42] Holcomb, D. F.; Norberg, R. E. *Phys.Rev.* **1955,** *98,* 1074.

[43] Torrey, H. C. *Phys. Rev.* **1953,** *92,* 962.

[44] Koningsberger, D.; Prins, R. *X-ray Absorption. Principles, Techniques and Applications of EXAFS, XANES, SEXAFS;* John Wiley: New York, 1988.

[45] Ankudinov, A. L.; Ravel, B.; Rehr, J. J.; Conradson, S. D. *Phys. Rev. B* **1998,** *58,* 7565.

[46] Ressler, T. *www.winxas.de* .

[47] Hagfeldt, A.; Grätzel, M. *Chem.Rev.* **1995,** *95,* 49-68.

[48] Bechinger, C.; Ferrere, S.; Zaban, A.; Sprague, J.; Gregg, B. A. *Nature* **1996,** *383,* 608-610.

[49] Canto, M. P.; Cisneros, J. I.; Torresi, R. M. *Thin Solid Films* **1995,** *259,* 70-74.

[50] Ohzuku, T.; Hirai, T. *Electrochim.Acta* **1982,** *27,* 1263-1266.

[51] Ottaviani, M.; Panero, S.; Morzilli, S.; Scrosati, B. *Solid State Ionics* **1986,** *20,* 197-202.

[52] Bonino, F.; Busani, L.; Manstretta, M.; Rivolta, B.; Scrosati, B. *J.Power Sources* **1981,** *6,* 261-270.

[53] Ohzuku, T.; Takehara, Z.; Yoshizawa, S. *Electrochim.Acta* **1979,** *24,* 219-222.

[54] Ohzuku, T.; Kodama, T.; Hirai, T. *J.Power Sources* **1985,** *14,* 153-166.

[55] Luca, V.; Hanley, T. L.; Roberts, N. K.; Howe, R. F. *Chem. Mater.* **1999,** *11,* 2089-2102.

[56] Wittingham, M. S.; Dines, M. B. *J.Electrochem.Soc.* **1977,** *124,* 1387-1388.

[57] Zachau-Christiansen, B.; West, K.; Jacobsen, T.; Atlung, S. *Solid State Ionics* **1988,** *28-30,* 1176-1182.

[58] van de Krol, R.; Goossens, A.; Meulenkamp, E. A. *J.Electrochem.Soc.* **1999,** *146,* 3150-3154.

[59] Murphy, D. W.; Cava, R. J.; Zahurak, S. M.; Santoro, A. *Solid State Ionics* **1983,** *9-10,* 413-417.

[60] Xu, Z.; Stebbins, J. F. *Science* **1995,** *270,* 1332-1334.

[61] Koller, H.; Engelhardt, G.; Kentgens, A. P. M.; Sauer, J. *J.Phys.Chem.* **1994,** *98,* 1544-1551.

[62] Chauvet, O.; Forro, L.; Kos, I.; Miljak, M. *Solid State Communications* **1995,** *93,* 667-669.

[63] Benco, L.; Barras, J. L.; Daul, C. A. *Inorg. Chem.* **1999,** *38,* 20-28.

[64] Benco, L.; Barras, J. L.; Atanasov, M.; Daul, C. A.; Deiss, E. *Solid State Ionics* **1998,** *112,* 255-259.

[65] Ernst, R. R.; Bodenhausen, G.; Wokaun, A. *Principles of nuclear magnetic resonance in one and two dimensions;* Clarendon Press, Oxford, 1994: Oxford, 1994.

[66] Schmidt-Rohr, K.; Spiess, H. W. *Multidimensional Solid-State NMR and Polymers;* Academic Press: London, 1994.

[67] Faux, D. A.; Ross, D. K. *J. Phys. C: Solid State Phys.* **1987,** *20,* 1441-1457.

[68] Sun, H. *J. Phys. Chem.* **1998,** *102,* 7338.

[69] W. G. Williams, R. M. Ibberson, P. D.; Enderby, J. E. *Physica B* **1998,** *241-243,* 234-236.

[70] Radaelli, P. G. *http://www.isis.rl.ac.uk/disordered/GEM/Software/Ariel3.1release.htm* .

[71] Larson, A. C.; Dreele, R. B. V. "GSAS", Technical Report NM 87545, Los Alamos National Laboratory, 1994.

[72] Gonzalez-Platas, J.; Rodriguez-Carvajal, J. *ftp://charybde.saclay.cea.fr/pub/divers/ fullprof.2k/Windows/* .

[73] Delley, B. *J. Chem. Phys.* **1990,** *92,* 508.

[74] Leach, R. L. *Molecular Modelling;* Pearson Education Limited: Harlow, 2001.

[75] Bee, M. *Quasielastic Neutron Scattering;* Adam Hilger: Bristol and Philadelphia, 1988.

[76] Rezayi, E. H.; Suhl, H. *Phys. Rev. B* **1982,** *25,* 2324.

[77] Beyeler, H. U.; Pietronero, L.; Strassler, S. *Phys. Rev. B* **1980,** *22,* 2988.

[78] Aydinol, M. K.; Kohan, A. F.; Ceder, G.; Cho, K.; Joannopoulos, J. *Phys. Rev. B* **1997,** *56,* 1354.

[79] Wasserman, S. R. *J. Phys. IV France* **1997,** *7,* C2-203.

[80] Grunes, L. A. *Phys. Rev. B* **1983,** *27,* 2111.

[81] Brydson, R.; Sauer, H.; Engel, W.; Thomas, J. M.; Zeitler, E.; Kosugi, N.; Kuroda, H. *J. Phys.: Condens. Matter* **1989,** *1,* 797.

[82] Ruiz-Lopez, M. F.; Munoz-Paez, *J. Phys.: Condens. Matter* **1991,** *3,* 8981.

[83] Wu, Z. Y.; Ouvrard, G.; Gressier, P.; Natoli, C. R. *Phys. Rev. B* **1997,** *55,* 10382.

[84] Cotton, F. A.; Wilkinson, G. *Advanced Inorganic Chemistry;* John Wiley and Sons Inc.: New York, 1972.

[85] Wagemaker, M.; Klaassen, A. *Unpublished results* .

[86] Saville, P. M.; Gonsalves, M.; Hillman, A. R.; Cubitt, R. *J. Phys. Chem. B* **1997,** *101,* 1.

[87] van de Kruijs, R. W. E. *Specular and off-specular reflection of polarized neutrons from magnetic thin films and multilayers,* Thesis, Delft University of Technology, 2002.

[88] van de Krol, R. *Lithium Intercalation in Anatase TiO$_2$,* Thesis, Delft University of Technology, 2000.

Structure and Dynamics of Lithium in Anatase TiO$_2$

by Marnix Wagemaker

Summary

Introduction

anatase TiO$_2$ is capable of hosting a high amount of Li-ions that can be inserted chemically or electrochemically. The lithium insertion involves a number of changes. In the first place the crystallographic structure of anatase TiO$_2$ host progressively changes to a structure that we refer to as Li-titanate. Until the original anatase grain is completely converted into Li-titanate, the two phases coexist. In order to maintain charge neutrality, the inserted Li ions are accompanied by electrons which result in a change in the electric and optical properties. This is directly observed as the original white powder turns dark blue, whilst in thin-film form the initial transparent film becomes partially reflecting. The optical changes are applicable in electrochromic devices, whereas the storage of lithium ions in the anatase TiO$_2$ lattice makes it a candidate for electrode material in Li-ion batteries. TiO$_2$ as electrode material has the advantage of being light weight, environmentally friendly and readily available.

Why is it interesting, and what do we want to know?

The insertion of lithium in anatase TiO$_2$ causes a number of processes at the atomic level that determine the macroscopic properties of the lithiated material. Understanding these processes, is the basis from which optimal devices can be designed. Lithiated TiO$_2$ is in many respects comparable to other lithiated transition metal oxides. Therefore, studying lithiated anatase is not only interesting with regard to the material itself, in addition it may be considered as a model material for other transition metal oxides. The questions that we address in this thesis can be divided into three classes, which refer to microscopic processes that take place upon Li-insertion. (1) *Changes in the atomic structure:* More specifically, where do the Li ions reside, what is its influence

on the host structure, and what is the morphology of the two coexisting phases (2) *Li-ion dynamics:* The dynamic performance of a battery is directly related to the Li-ion dynamics. Therefore, we wish to know on what timescale the Li-ion moves through the lattice and if there is a specific mobility limiting factor in the two phase morphology of lithiated anatase? Li-ion dynamics can also be expected to maintain the two phase equilibrium between the original and the Li-titanate phase, which is responsible for the maintenance of a constant potential during battery operation, but on what timescale does this take place? (3) *Changes in the electronic structure:* The Li-ion insertion does not only involve the ion itself, it is accompanied with a charge compensating electron. We wish to know the type of orbital that this electron occupies, is it a conducting state or a localized state, and what does this mean for the optical properties?

Some of these processes can be expected to be correlated, for instance in many cases structural changes can be related to changes in the electronic configuration. A challenging question with regard to Li-ion battery materials is: if and how the electronic structure influences the Li-ion dynamics.

In this thesis these fundamental aspects and questions are subject to investigation, using complementary techniques, such as neutron scattering, nuclear magnetic resonance and X-ray absorption spectroscopy, that probe the Li and its environment. The advantage of combining these techniques is that the results cover length scales from 0.1 to ≈100 nm and time scales from picoseconds up to seconds. This facilitates the interpretation of macroscopic properties in terms of processes at the atomic scale. In the following, the findings of this study are summarized starting at the macroscopic level, progressively scaling down to the atomic level.

Seconds down to milliseconds

Inserting lithium in anatase results in phase separation in a lithium poor phase, composition $Li_{\approx 0.026}TiO_2$ with the original anatase structure, and a lithium rich phase, composition $Li_{\approx 0.52}TiO_2$ with a slightly different structure compared to anatase.

Line intensities and broadening of X-ray and neutron diffraction peaks as a function of the Li fraction indicates that one phase (the Li-rich Li-titanate phase) grows with increasing Li contents at the expense of the other phase (the Li-poor anatase phase). Within one μm-sized powder particle the phases coexist with typical domain sizes in the order of 100 nm. Neutron reflectometry probes the growth and shrinking of the phases directly in a battery configuration. The lithium distribution, and hence the phase distribution changes during the intercalation yielding a flat Li-titanate front, parallel to the electrode surface, penetrating the thin smooth anatase TiO_2 layer. During extraction the phase front reversibly moves back to the electrode/electrolyte interface. These experiments clearly reject other, more complicated, intercalation schemes as well as percolation of Li along grain boundaries of the polycrystalline film.

The equilibrium between the coexisting two phases can only be maintained if there is Li exchange between the two phases. The Li-exchange between Li-anatase and Li-titanate is probed by two-dimensional ^7Li nuclear magnetic resonance. With this technique the change in chemical environment after allowing the lithium to diffuse for a certain "mixing" time is measured. For this particular system, the difference in chemical environment of the Li is provided by the two coexisting phases. The results show

that lithium is continuously diffusing from one phase to another in an equilibrium situation, analogous to molecules exchanging between a coexisting liquid and its vapor. The timescale of the Li-ion diffusion between the two phases, over distances in the order of the domain sizes ($\approx$100 nm), is around 50 ms. This equilibrium exchange limits the overall diffusion in anatase TiO_2 as it appears to be harder (activation energy $\approx$ 0.43 eV) compared to the diffusion within each of the separate phases (see below). Thereby, it is suggested that the Li diffusion in a TiO_2 electrode is limited by the equilibrium flux between the two phases as this can be expected to determine the growth and and shrinking of the two phases during battery operation.

The microsecond range

One-dimensional ^{7}Li nuclear magnetic resonance can probe the lithium ion dynamics on the μs timescale (roughly 50 μs in Li-titanate en 20 μs in Li-anatase between two hops at 300 K). Hopping from one Li site to another (Li is located in the oxygen octahedra, see below) over a distance of roughly 3 Å on this timescale causes lithium to experience more averaged dipolar interactions resulting in less efficient transversal relaxation, an effect generally referred to as motional-narrowing. Although there are more unoccupied available sites in Li-anatase, lithium diffuses more easily through the Li-titanate phase (activation energy $\approx$ 0.09 eV in Li-titanate compared to $\approx$ 0.2 eV in Li-anatase). This may be related to the higher concentration of charge compensating electrons in Li-titanate. These electrons are expected to screen the potential landscape experienced by the Li-ions (see below). The coupling between the charge compensating electrons and the diffusion of the Li-ions is also suggested by the onset of the lithium mobility at about 200 K, the same temperature where the Ti-*3d* conduction bands are being filled appreciably.

Down to picoseconds

Detailed analysis of high-quality neutron diffraction data reveals, in both phases, two available Li-ion positions within the oxygen octahedron. These sites are only 0.7 Å separated in Li-titanate and 1.8 Å in anatase and never occupied at the same time. The finding of multiple discrete Li sites inside distorted oxygen octahedra is rather remarkable and one might expect that Li intercalated TiO_2 is not the only oxide in which this occurs. The fact that such multiple discrete sites have not been observed before is probably related to the difficulty of observing Li in diffraction experiments, or the difficulty in assigning resonances of a local probe like NMR for that matter. In neutron diffraction performed with inferior resolution, statistics and limited d-range, these sites will simply not be resolved, and in the best cases will just be identified as an anisotropic temperature factor. One of the consequences is that theoretical work on this type of compounds will require modifications; special care should be taken with respect to the Li positions.

The distinguishable Li sites in Li-titanate are also reproduced by molecular dynamics simulations (see below), but only if a specific Li-ordering is assumed. This ordered structural model can be argued based on simple repulsive Coulomb interactions between the Li-ions. However, it does not lead to a superstructure in the observed neutron diffraction powder patterns due to the short range of the ordering in combination with the slow Li-ion hopping between the neighboring octahedra. The simulations thus indicate

the importance of Li-Li interactions in this system. The model also explains the apparent preference for the value of the Li fraction, Li/Ti≈ 0.5, in Li-titanate. If more than half of the available Li-ion sites is occupied (the two positions within an oxygen octahedron count as one), Li/Ti> 0.5, short Li-Li distances will occur, which is energetically unfavorable due to the repulsive Coulomb interaction between the Li-ions. During electrochemical Li-insertion an over-potential will be needed to raise the Li fraction above 0.5, in general this is not practical because the over-potential will cause side-reactions at the electrode/electrolyte interface rather than increasing the Li content of the electrode.

The temperature dependence of the lithium occupation as probed with neutron diffraction in the two newly found sites within one octahedron in Li-titanate reveals a 3.4 meV energy difference between these sites. The combination of molecular dynamics simulations and quasi-elastic neutron scattering provides insight into the intra-octahedron dynamics between the two sites. Quasi-elastic neutron scattering experiments reveal that the time between hopping from one site to the other is about 1.7 ps at 250 K. This hopping appears to be thermally activated with a 5.7 meV potential barrier between the sites. The calculated potential barrier for Li moving from one site to the other, overestimates the experimentally found value. This illustrates the importance of lattice dynamics for the Li-ion mobility in lithiated TiO_2.

The width of the ^{7}Li NMR resonance for Li in anatase (Li/Ti≈ 0.026), Li in Li-titanate (Li/Ti≈ 0.52) and Li in $Li_{0.7}TiO_2$ is electronic in nature and increases with the Li fraction. This may suggest that the coupling between the charge compensating electrons and the Li-ions is stronger in Li-titanate compared to the coupling in the Li-poor anatase. This offers an explanation for the higher Li-ion mobility in Li-titanate compared to that in anatase, if the stronger coupling is interpreted as being proportional to the effective screening of the Li-ion charge.

The subtle change in chemical environment of lithium in both Li-anatase and Li-titanate phases as a function of temperature detected with ^{7}Li NMR can be explained as a change in the Ti-*3d* electron density. This implies the existence of a Li-induced donor level just below the conduction band ($\approx$ 100 meV in Li-anatase and $\approx$ 40 in Li-titanate). X-ray absorption spectroscopy at energies just below the ionization energy of the Ti core electron, excite these electrons to unoccupied orbitals in the Ti conduction band (Ti K-edge XANES). Upon intercalation, the Li-electron density fills the states at the bottom of the conduction band that are Ti-Ti (Ti-3d) bonding and Ti-O (Ti-3d and O-2p) anti bonding. This causes deformation of the original anatase structure in such a way that the Ti-Ti distances are shortened and the Ti-O distances are elongated. This explains the phase transition from anatase to Li-titanate. The majority of the charge compensating electron density is suggested to reside in the Ti-Ti bonding bands which are covalent (semi-localized) in nature. This might explain the low electron conductivity of lithiated anatase despite of the high concentration of charge compensating electrons. The electronic structure suggested by Ti K-edge XANES, in combination with the semi-localized electron character, give a consistent picture, also explaining the experimentally found broad absorption bands representing the electrochromic effect.

Concluding remarks

In conclusion, the multi-technique approach presented in this thesis has lead to a consistent and coherent description of lithiated anatase TiO_2. The Li dynamics from picoseconds up to seconds has been revealed, describing the local motions within its oxygen cage up to the Li exchange between the two coexisting phases which is responsible for the constant potential during battery operation. The complete description of this lithiated transition metal involves all three aspects, the atomic structure, Li-ion mobility and the electronic structure and, in addition, the correlation between these aspects. This study has resulted in a number of new or, apparently, underrated aspects in the field of Li-ion battery materials, such as, the importance of Li-Li interactions, multiple discrete intra-octahedral Li-ion sites, the coupling of the electronic configuration with the Li-ion mobility and the equilibrium Li-exchange between the two coexisting phases.

Structuur en Dynamica van Lithium in Anatase TiO$_2$

door Marnix Wagemaker

Samenvatting

Inleiding

Titaandioxide (TiO$_2$) met de 'anatase' kristalstructuur kan een grote hoeveelheid Li-ionen herbergen. Deze kunnen zowel chemisch als elektrochemisch geïntercaleerd worden. Het laden met lithium heeft een aantal veranderingen tot gevolg. In de eerste plaats verandert de kristalstructuur van anatase TiO$_2$ in een structuur die we Li-titanaat noemen. Totdat het anatase compleet is omgezet in Li-titanaat, komen de twee fasen naast elkaar voor. Ter wille van ladingsneutraliteit worden de opgenomen Li-ionen vergezeld van elektronen die een verandering teweeg brengen in de elektrische en optische eigenschappen. In de twee geometrische vormen van anatase die we bekijken, poeder en dunne, gesputterde, film, is dit is direct zichtbaar: het witte anatase poeder wordt blauw, en de transparante dunne film wordt gedeeltelijk reflecterend. Deze optische (elektrochrome) veranderingen worden onder andere toegepast in smart windows. De opslag van Li-ionen in het anataserooster vindt zijn toepassing als deze gebruikt wordt als elektrode in een Li-ion batterij. TiO$_2$ als elektrode materiaal heeft de voordelen dat het licht is, milieu vriendelijk en rijkelijk voorhanden.

Waarom is het interessant, en wat willen we weten?

De lithium intercalatie in anatase TiO$_2$ gaat gepaard met een aantal processen op atomaire schaal, die uiteindelijk de macroscopische materiaaleigenschappen bepalen. Begrip van deze processen is de basis waarop betere toepassingen kunnen worden ontworpen. Gelithieerd TiO$_2$ is in veel aspecten te vergelijken met andere overgangsmetaal-oxides. Daarom is onderzoek naar gelithieerd anatase TiO$_2$ niet alleen interessant op zichzelf, maar het kan ook gezien worden als modelmateriaal voor andere overgangsmetaal-oxides. De vragen die we in dit proefschrift hopen te beantwoorden kunnen in drie groepen worden onderverdeeld, elke groep refereert naar microscopische processen die plaats vinden

als gevolg van de lithiumintercalatie. (1) *Veranderingen in de atomaire structuur:* Specifieker, waar bevinden de Li-ionen zich, wat is de invloed van de Li-ionen op de structuur van het anatase TiO_2, en wat is de morfologie van de twee naast elkaar bestaande fasen? (2) *Li-ion dynamica:* De maximale stroom die een batterij kan leveren is direct gerelateerd aan de Li-ion dynamica. Daarom willen we weten op welke tijdschaal de Li-ionen door het rooster bewegen, en wat de beperkende factor is voor de Li-ion mobiliteit in de twee-fasen morfologie. Het is te verwachten dat de Li-ion dynamica ook het twee-fasen evenwicht tussen de originele anatase fase en de Li-titanate in stand houdt. Dit evenwicht zorgt voor een constante potentiaal gedurende het laden en ontladen van de batterij. De vraag is echter, op welke tijdschaal vindt dit Li-ion transport tussen de twee fasen plaats? (3) *Veranderingen in de elektronische structuur:* De Li-ion intercalatie gaat gepaard met de opname van een elektron om de ladingsneutraliteit te behouden. We willen weten welke orbitaal dit elektron bezet, en wat het karakter ervan is: is het een geleidings- of een gelokaliseerd orbitaal, en wat betekent dat voor de optische eigenschappen?

Van een aantal van deze processen kan worden verwacht dat ze gecorreleerd zijn. Zo kunnen bijvoorbeeld structurele veranderingen vaak gepaard gaan met elektronische veranderingen en *vice versa*. Een uitdagende vraag in verband met Li-ion batterij materialen is: of en hoe de elektronische structuur de dynamica van het Li-ion beïnvloedt.

In dit proefschrift zijn deze fundamentele aspecten en vragen het onderwerp van onderzoek. Hierbij wordt gebruik gemaakt van complementaire technieken, zoals neutronenverstrooiing, kern spin resonantie (NMR) en Röntgen absorptie spectroscopie, die alle gevoelig zijn voor het Li-ion en zijn omgeving. Het voordeel van de combinatie van deze technieken is dat de resultaten verschillende lengte- en tijdschalen bestrijken, van 0,1 tot 100 nm, en van picoseconden tot seconden. Dit maakt het mogelijk de macroscopische eigenschappen te interpreteren op basis van processen die plaatsvinden op atomaire schaal. Hieronder worden de resultaten van deze studie samengevat, beginnend op het macroscopische niveau, en vervolgens afdalend tot het atomaire niveau.

Seconden tot milliseconden

Lithium insertie in anatase TiO_2 resulteert in fasescheiding in een lithium arme fase, met samenstelling $Li_{\approx0,026}TiO_2$ met de originele anatasestructuur, en een lithium rijke fase, $Li_{\approx0,52}TiO_2$ met een iets andere structuur.

De poederpreparaten zijn onderzocht met behulp van de Röntgen en neutronendiffractie. De intensiteit en verbreding van de pieken als functie van de Li fractie duidt erop dat een van de fasen groeit met toenemende Li fractie (de Li-rijke Li-titanaat fase) ten koste van de andere fase (de Li-arme anatase fase). Binnen één deeltje, met afmetingen van enkele μm, hebben de twee coëxisteren fasen typische domeingroottes in de orde van 100 nm. Met neutronenreflectometrie is de groei en het krimpen van de fasen direct waargenomen in de batterijconfiguratie (filmgeometrie). De lithiumverdeling, dus de faseverdeling, verandert gedurende de intercalatie. Gedurende het laden met lithium, penetreert een vlak Li-titanaat front, parallel aan het elektrode oppervlak, de dunne anatase TiO_2 laag. Tijdens de Li extractie beweegt het fasefront omkeerbaar terug naar het elektrode/elektrolyt grensvlak. Deze experimenten sluiten andere, meer gecompliceerde, intercalatieschema's, en percolatie van Li langs korrelgrenzen in de poly-kristallijne dunne laag uit.

Het evenwicht tussen de twee coëxisterende fasen kan alleen in stand worden gehouden door Li transport tussen de fasen. De uitwisseling van Li tussen Li-anatase en Li-titanate is onderzocht met twee-dimensionale ^{7}Li NMR. Met deze techniek is het mogelijk de verandering te meten van de chemische omgeving die het Li ondervindt gedurende een "mixing" tijd. Voor gelithieerd anatase kan deze techniek gebruikt worden omdat de chemische omgeving van het Li verschillend is voor de twee fasen. De metingen laten zien dat, in evenwicht, het Li onafgebroken tussen de twee fasen diffundeert, vergelijkbaar met de evenwichtsuitwisseling van moleculen tussen een vloeistof en zijn damp. De tijdschaal van deze Li uitwisseling tussen de twee fasen, over afstanden in de orde van de domeingrootte (≈ 100 nm), is ongeveer 50 ms. De hoge activeringsenergie voor Li-diffusie tussen de twee fasen ($\approx 0{,}43$ eV), in vergelijking met de diffusie binnen elk van de fasen (zie beneden), duidt erop dat de samengestelde diffusie in anatase TiO_2 is gelimiteerd door de evenwichtsuitwisseling. Dit suggereert dat de Li-ion diffusie, in een anatase TiO_2 elektrode wordt bepaald door de uitwisseling van Li tussen de fasen, omdat dit de groei en het krimpen van de twee fasen zal bepalen tijdens de werking van de batterij.

Rond de microseconden

Met een-dimensionale ^{7}Li-NMRwordt de Li-ion dynamica (sprongdiffusie) onderzocht op een tijdschaal van μs (ongeveer 50 μs in Li-titanaat en 20 μs in Li-anatase tussen twee sprongen bij 300 K). Het springen van Li van één positie naar een andere (De Li-ion posities bevinden zich binnen de zuurstof octaëders) over een afstand van ongeveer 3 Å op de μs tijdschaal heeft tot gevolg dat Li een scherper gedefinieerde dipool interactie ervaart. De consequentie is dat de transversale relaxatie minder efficiënt is, een effect dat "motional narrowing" wordt genoemd. Ondanks het grotere aantal onbezette posities in Li-anatase diffundeert Li makkelijker in Li-titanaat (activeringsenergie $\approx 0{,}09$ eV in Li-titanaat vergeleken met $\approx 0{,}2$ eV in Li-anatase). Dit heeft mogelijkerwijs te maken met de hogere concentratie van ladingscompenserende elektronen in Li-titanaat. Naar verwachting schermen deze elektronen het door de Li-ionen ervaren potentiaallandschap af (zie beneden). De koppeling tussen de ladingscompenserende elektronen en de diffusie van het Li wordt ook gesuggereerd doordat de Li-ionen mobiel worden vanaf ongeveer 200 K, dezelfde temperatuur waarbij de elektronendichtheid in de Ti-*3d* orbitaal aanzienlijk toeneemt.

Naar de picoseconden

Uit gedetailleerde analyse van neutronendiffractie data blijkt dat in allebei de fasen twee posities binnen één zuurstof octaëder beschikbaar zijn. Deze posities zijn slechts 0,7 Å van elkaar verwijderd in Li-titanate en 1,6 Å in Li-anatase, en zijn dus niet tegelijkertijd bezet. Deze waarneming van meerdere discrete Li-ion posities binnen één verstoorde zuurstof octaëder is uitzonderlijk, en het is te verwachten dat gelithieerd anatase TiO_2 niet het enige oxide is waarin dit het geval is. Dat zulke meervoudige posities niet eerder zijn waargenomen heeft waarschijnlijk te maken met het feit dat Li moeilijk te zien is doormiddel van diffractie experimenten en dat het moeilijk is onderscheid te maken tussen de kernspin resonanties van zulke posities. In een neutronendiffractie-experiment, uitgevoerd met lagere resolutie, beperkte statistiek en een kleiner d-interval, worden zulke meervoudige posities niet onderscheiden. In het gunstigste geval wordt een

anisotrope temperatuurfactor gevonden. Een van de gevolgen van de huidige bevindingen is dat theoretisch werk aan deze materialen moet worden aangepast in verband met de aanwezigheid van meervoudige Li-ion posities in de zuurstof octaëders.

De twee mogelijke Li-ion posities in de zuurstof octaëders in Li-titanaat worden gereproduceerd met moleculaire dynamica simulaties (zie beneden), maar alleen als een specifieke Li ordening wordt aangenomen. Deze structurele ordening van het Li volgt direct uit simpele argumenten betreffende de afstotende Coulomb interactie tussen de Li-ionen. Niettemin leidt de ordening niet tot superstructuur pieken in de waargenomen neutronendiffractiepatronen vanwege de beperkte dracht van de ordening in combinatie met het springen van Li-ionen tussen naburige octaëders. De simulaties geven aan dat in dit systeem de Li-Li interacties van belang zijn. Het geordende model verklaart ook de voorkeur voor de Li fractie $Li/Ti \approx 0,5$ in Li-titanaat. Indien meer dan de helft van de aanwezige Li-ion posities bezet is (de twee posities binnen een octaëder tellen als een), zullen er korte Li-Li afstanden voorkomen, hetgeen energetisch ongunstig is als gevolg van de afstotende Coulomb interactie. In het geval van elektrochemische intercalatie zal een over-potentiaal nodig zijn om de Li-ion fractie boven de 0,5 te doen stijgen. Over het algemeen zal zo'n over-potentiaal zij-reacties aan het elektrode/elektrolyt grensvlak tot gevolg hebben, in plaats van de gewenste toename van de Li-ion fractie in de elektrode.

De met neutronendiffractie gemeten temperatuur-afhankelijke bezetting van de twee nieuw gevonden Li-ion posities binnen een zuurstof octaëder in Li-titanaat, leidt tot een 3,4 meV energieverschil tussen deze posities. De combinatie van moleculaire dynamica simulaties en quasi-elastische neutronenverstrooiing geeft inzicht in de intra-octaëder Li-ion dynamica tussen de twee posities. Quasi-elastische neutronenverstrooiing leert dat de tijd tussen het springen van de ene naar de andere positie ongeveer 1,7 ps is bij 250 K. Dit springen blijkt thermisch geactiveerd met een potentiaalbarrière van 5,7 meV tussen de posities. De met de simulaties berekende potentiaal is groter dan de experimentele waarde. Dit illustreert dat roosterdynamica een belangrijke invloed heeft op de Li-ion mobiliteit in gelithieerd TiO_2.

De breedte van de NMR–resonantielijnen van Li in anatase ($Li/Ti \approx 0,026$), Li in Li-titanaat ($Li/Ti \approx 0,52$) en Li in $Li_{0,7}TiO_2$ is van elektronische origine, en neemt toe met de Li fractie. Dit suggereert dat de koppeling tussen de Li-ion ladingscompenserende elektronen en de Li-ionen in Li-titanaat sterker is dan in de Li-arme Li-anatase fase. Indien die koppeling geïnterpreteerd wordt als effectieve afscherming van de Li-ion lading, zou dit een mogelijke verklaring zijn voor de hogere Li-ion mobiliteit in Li-titanaat vergeleken met die in Li-anatase.

De subtiele verandering in de chemische omgeving van lithium in zowel de Li-anatase als de Li-titanaat fase als functie van temperatuur, gemeten met ^{7}Li-NMR, kan worden verklaard door een verandering in de Ti-$3d$ elektronendichtheid. Dit impliceert het bestaan van een Li geïnduceerd donorniveau vlak onder de geleidingsband (≈ 100 meV in Li-anatase en ≈ 40 meV in Li-titanaat). Röntgen absorptie spectroscopie bij energieën vlak onder de ionisatie-energie van het Ti core-elektron, exciteren deze elektronen naar onbezette orbitalen in de Ti geleidingsband (Ti K-edge XANES). De Li-intercalatie heeft tot gevolg dat de Li-elektrondichtheid de toestanden onder in de geleidingsband vullen, die een Ti-Ti (Ti-$3d$) bindend en Ti-O (Ti-$3d$ and O-$2p$) niet bindend karakter hebben. Omdat hierdoor de Ti-Ti afstanden kleiner en de Ti-O afstanden groter worden, wordt de originele anatasestructuur gedeformeerd. Dit verklaart de structuurovergang van de

anatase- naar de Li-titanaatfase. Het grootste gedeelte van de ladingscompenserende elektronen lijkt in de covalente (semi-gelokaliseerde), Ti-Ti bindende, orbitalen te verblijven. Dit kan de elektronengeleiding van gelithieerd anatase TiO_2 verklaren, die laag is ondanks de hoge concentratie ladingscompenserende elektronen. De elektronische structuur, zoals gesuggereerd door Ti-K edge XANES, in combinatie met het semi-gelokaliseerde elektronenkarakter, leidt tot een consistente beschrijving van de elektronische structuur, die ook de experimenteel gevonden brede optische absorptiebanden kan verklaren (het elektrochrome effect).

Ter conclusie

De combinatie van technieken gepresenteerd in dit proefschrift heeft geleid tot een consistente en coherente beschrijving van gelithieerd anatase TiO_2. De Li dynamica van picoseconden tot seconden is blootgelegd; van de lokale beweging binnen de zuurstofkooi tot de Li uitwisseling tussen de twee coëxisterende fasen. Deze laatse is verantwoordelijk voor een constante potentiaal van een batterij. De complete beschrijving van dit gelithieerde overgangsmetaal oxide behelst alle drie de aspecten, atomaire structuur, Li-ion mobiliteit en elektronische structuur, inclusief de correlatie tussen deze aspecten. Deze studie heeft geresulteerd in een aantal nieuwe en/of tot nu toe ondergewaardeerde aspecten op het vakgebied van Li-ion batterijmaterialen, zoals het belang van Li-Li interacties, meervoudige intra-octaëder Li-ionposities, de koppeling van de elektronische structuur met de Li-ion mobiliteit en de Li-uitwisseling tussen de twee coëxisterende fasen.

Acknowledgements

There are many people who contributed to this thesis in one way or another. In fact I could not have done it without all these persons. It is not just the support in the scientific context, but also in the positive atmosphere that was created during the time of this thesis study.

First to mention are my daily supervisors Ad van Well and Fokko Mulder. Ad was my official supervisor, and in addition Fokko became intensively involved due to the direction that the research took me. The inexhaustible enthusiasm and "will to understand" of both of them was an inspiration and a great pleasure to work with. Ad gave me the freedom and confidence in finding my way during the four years, which started with a rather loosely defined subject. He teached me to be more consistent in my research and in particular in formulating it in the form of papers. Fokko confronted me with a way of looking at physics above the details and the techniques in terms of length and time scales. He came up with ideas and suggestions, like "lets try NMR", that have considerably attributed to this thesis and to my understanding in various subjects.

In the first year, when my subject was finding its way and I was looking for it, I met Roel van de Krol from the inorganic chemistry group in Delft of Prof. J. Schoonman. At that time Roel was in the middle of his thesis study and had a number of unanswered questions that were suited for the more microscopic neutron techniques. This actually initiated all the research that has lead to this thesis. He introduced me into electrochemistry, and our discussions were always both fruitful and enjoyable.

My professor Don Kearley enriched our group in the beginning of my thesis study. In particular at the end I had the chance to work with him as he introduced my in the molecular dynamics calculations which have made me very enthusiastic.

Professor Arno Kentgens has given us the opportunity to do NMR experiments, in which a lot of time has been invested. More than that, he has been a critical referee of my NMR thoughts and interpretations increasing the quality and my understanding. Besides that I was lucky to have the technical support of Gerda Nachtegaal en later Adri Klaassen in performing the NMR experiments.

I met Dirk Lützenkirchen-Hecht from the university Wuppertal at a conference after a talk that I considered very relevant for my subject. Ever since, it has been a great pleasure to cooperate with him, designing cells, discussing and doing the EXAFS experiments. He has been tested thoroughly every time that I came with samples which hardly brought what we hoped, he never lost hope and we were always able to turn it to the positive side, brilliant. His entire group lead by professor Ronald Frahm has been very nice to work with and to visit. At the beam line at Hasylab my hero is Patrick, who more than once broke the record of working continuously together with Ulrich, thereby optimally using the beam-time.

When Roel left I lost my "contact" at the chemistry laboratory where I spend a lot of time sweating with my arms in the glove box. Not being my home lab, I always had to bother the people there with my often silly questions concerning chemistry. Frans Ooms was always prepared to help, and easy to find as he was always whistling a tune walking through the building. It didn't take much time before we were cooperating in a number of publications, where we performed neutron diffraction on his electrode materials in order to determine the structure.

Other people in the Inorganic Chemistry group with who I had valuable contact were Albert Goossens, Adam Best and Dan Simon. I thank the whole group, because I was always welcome to use their facilities and resources.

The thin film TiO2 anatase samples were prepared by D. Blank and F. Roesthuis of the Material Science group, Department of Applied Physics, University of Twente. I gratefully acknowledge them for all the time that they invested in preparing samples for me.

Peter Bouwman from the University Twente came in touch with us as he was interested in doing the same neutron reflection experiments we were planning for his materials. Although we were not able to perform the experiments as we wished, I experienced the cooperation as very pleasant and useful.

Although the thesis subject of Edwin Currie has by no means a relation with my subject, I want to thank him for our good cooperation. I was very happy to help with the data fitting of the neutron reflection measurements he performed on his polymers which worked out very nice.

The neutron scattering and Mössbauer group at IRI has been a wonderful group to work. Everyone is always there to help, the atmosphere is professional, relaxed and personal. I cannot imagine there are more pleasant places to work thanks to the whole group. In particular I thank the technical support of Piet, Hans en Henk in the design, drawing and making of cells for experiments, not to forget the nice expanded view of the neutron reflectometry cell for in my thesis by Piet.

During the experiments at ISIS I was always supported by the local instrument scientists, Stephen Holt and John Webster at SURF and Michael Hofmann at GEM, and also by the NWO representative at ISIS Dick Visser.

I gratefully acknowledge the Netherlands Organization for Scientific Research (NWO), because part of the research performed has been financially supported by NWO.

Most of the daily contact was with my room mates. My first roommate was Octay with whom I visited the HERCULES course in Grenoble. I had the pleasure to accompany him on his first day skiing. I think by now we should know who won our little contest, I'm afraid he won. In my new room I met Xhou Rong, whose company I enjoyed not very long as he became terribly sick and died in 2002 from cancer. After a period of isolation, Kuni Myasaki joined me, and a wonderful period of hard work, laughter and friendship followed. Unfortunately Kuni left to the States after almost two years, and I ended up in the "PhD-student room (sorry Jeroen)" of our group, a bit afraid for this crowded house, existing of Gijs, Lambert, Jeroen and Alexander, I very soon enjoyed the company intensively. There was always fun and interesting discussions and always people that think with you, and make strong coffee. I am not looking forward to leave this, thanks guys.

There was no week without climbing, but what is climbing without friends. I thank

them all for the wonderful, enthusiastic and fanatic atmosphere which I hope to enjoy for infinite time. Special thanks goes to Frido, together we created the cover which shows Mount Kenia, located near the equator.

My mother, Ada and my sister were always there, caring and enthusiastic in whatever I do. My dad and An, were always proudly supporting and interested in what I was doing in Delft. I praise myself lucky with my home fronts.

Last but not least, Ditte and Cheyenne, who suffered from my workaholic attitude during the last months, but never stopped encouraging me. They were always enthusiastic when I told about what I was doing and when I proudly showed a paper or a chapter. I acknowledge Cheyenne who assisted me enthusiastically in calculations, in particular in adding integer numbers.

Curriculum vitae

Marnix Wagemaker was born on the 26th May 1971 in Leiden, The Netherlands. There he attended the "Vrije School" and received his MAVO diploma in May 1990. One year later he obtained his VWO diploma. He subsequently started to study Aeronautics at the Delft University of Technology where he obtained his Propadeuse one year later. In January 1992 he changed his studies to Technical Physics at the same university. In August 1996 he graduated on adsorption of proteins at the air-water interface studied with neutron reflectometry in the Radiation Physics department of the Interfacultair Reactor Institute (IRI) in Delft. From August to December he travelled through India and Nepal. Subsequently he started working at the Macneil-Schwendler Cooperation as a programming development engineer. One and a half year later, in September 1998, he returned to the IRI to start his PhD promotion study from which this thesis resulted.

List of publications

- *Structure of Monodisperse and Bimodal Brushes*
  E.P.K. Currie, M. Wagemaker, M.A. Cohen Stuart and A.A. van Well, Macromolecules 32 (1999) 9041-9050

- *Overflowing cylinder for neutron reflection research at expanding surfaces*
  M. Wagemaker, F.J.G. Boerboom, H.J. Bos and A.A. van Well, Physica B 283 (2000) 278-281

- *Structure of grafted polymers, investigated with neutron reflectometry*
  E.P.K. Currie, M. Wagemaker, M.A. Cohen Stuart and A.A. van Well, Physica B 283 (2000) 17-21

- *Lithium intercalation in anatase TiO_2; An EXAFS study*
  D. Lützenkirchen-Hecht, M. Wagemaker, P. Keil and A.A. van Well, Hasylab Annual Report 2000

- *Two Phase Morphology Limits Lithium Diffusion in TiO_2 (Anatase); a ^7Li MAS NMR Study*
  M. Wagemaker, R. van de Krol, A.P.M. Kentgens, A.A. van Well and F.M. Mulder, J. Am. Chem. Soc. 46 (2001) 11454-11461

- *An EXAFS study of Li^+-intercalated anatase TiO_2*
  D. Lützenkirchen-Hecht, M. Wagemaker, P. Keil, A.A. van Well and R. Frahm, Hasylab Annual Report 2001

- *A cell for quasi in-situ studies of electrode surfaces*
  D. Lützenkirchen-Hecht, M. Wagemaker, P. Keil and A.A. van Well, Hasylab Annual Report 2001

- *Structure determination of high-voltage $LiMg_\delta Ni_{0.5-\delta}O_4$ spinels for Li-ion batteries*
  F.G.B. Ooms, M. Wagemaker, A.A. van Well, F.M. Mulder, E.M. Kelder and J. Schoonman Applied Physics A, in press

- *High-Voltage $LiMg_\delta Ni_{0.5-\delta}O_4$ spinels for Li-ion batteries*
  F.G.B. Ooms, M. Wagemaker, F.M. Mulder, E.M. Kelder and J. Schoonman Solid State Ionics, 152-153 (2002) 143-153

- *Lithium transport for equilibrium between nano-crystalline phases in intercalated TiO_2 anatase*
  M. Wagemaker, A.P.M. Kentgens and F.M. Mulder, Nature 418 (2002) 397-399

- *Quasi-in-situ reflection mode EXAFS at the Ti K-edge of lithium intercalated TiO_2 rutile*
  D. Lützenkirchen-Hecht, M. Wagemaker, P. Keil, A.A. van Well and R. Frahm, to be published (submitted to Surface Science)

- *Multiple Li positions inside oxygen octahedra in lithiated TiO_2 anatase*
  M. Wagemaker, G.J. Kearley, A.A. van Well, H. Mutka, and F.M. Mulder, J. Am. Chem. Soc. Accepted for publication

- *Quasi-in-situ reflection mode EXAFS at the Ti K-edge of lithium intercalated TiO_2 rutile and anatase*
  M. Wagemaker, D. Lützenkirchen-Hecht, P. Keil, A.A. van Well and R. Frahm, to be published (submitted to Physica B)

- *Nano-morphology of lithiated thin film TiO_2 anatase probed with in-situ neutron reflectometry*
  M. Wagemaker, R. van de Krol and A.A. van Well, to be published (submitted to Physica B)

- *Lithium intercalation in anatase TiO_2, A transmission EXAFS and Quasi-in-situ reflection mode EXAFS study at the Ti K-edge*
  M. Wagemaker, D. Lützenkirchen-Hecht, P. Keil, A.A. van Well and R. Frahm, manuscript in preparation

- *$Li[CrTi]O_4$: a stable 1.505 V spinel for rechargeable Li-ion batteries*
  F.G.B. Ooms, M. Wagemaker, F.M. Mulder, E.M. Kelder and J. Schoonman, manuscript in preparation

- *Changes in the electronic structure of $Li_{1+x}[Li_{1/3}Ti_{5/3}O_4]_3$ spinel*
  M. Wagemaker, D. Lützenkirchen-Hecht, P. Keil, A.A. van Well and R. Frahm, manuscript in preparation

- *Lithium Positions in Single Phase Spinel $Li_{4+x}Ti_5O_{12}$ Anode upon Lithium Charging*
  F.M. Mulder, M. Wagemaker, D. Simon, M. Hofmann, E.M. Kelder, J. Schoonman , manuscript in preparation